Optical Information Processing using Photorefractive BSO

Colin Soutar

A thesis submitted in partial fulfilment of the
requirements for the degree of Doctor of Philosophy

Sponsoring Establishment : Dundee Institute of Technology
Submitted : December 1991

Acknowledgements

Thanks to Dr.'s Allan Gillespie and Colin Cartwright for their encouragement, assistance and patience throughout the time of this work. Also the support of Wang Zhaoqi and Charlie Main is greatly appreciated.

Thanks to Dr. B. Jefferies who, as Head of Department, lent his support at the times when it was necessary.

The advice and assistance of the technical staff of the Department of Electronic and Electrical Engineering is gratefully acknowledged.

Thanks are due to the departmental secretarial staff (especially Linda) for their assistance and co-operation.

Special thanks are due to Wendy for enduring all of the unsociable aspects of conducting a PhD. Also, thanks to Steve for helping to maintain a healthy perspective of the proceedings.

Optical Information Processing using Photorefractive BSO

Colin Soutar

Abstract

Several optical information processing tasks are implemented using photorefractive BSO as a dynamic holographic medium. The physical basis for the mechanism which allows the implementation of these devices is studied.

The properties of BSO which make it particularly attractive as a processing medium are highlighted, and experimental results are presented to demonstrate its practical limitations.

An extensive study is presented of the influence of optical bias on the grating formation characteristics. This leads to a documentation of the optimum conditions for transient enhancement of a beam diffracted from such a grating. This transient enhancement can be controlled to provide ideal characteristics for the implementation of transient devices such as a novelty filter.

A novelty filter utilising this transient enhancement is subsequently demonstrated. It exhibits good temporal discrimination through the choice of suitable external optical conditions, and the use of digital thresholding. The overall device operates at T.V. frame rates.

Results are also presented of various optical correlators using BSO. These include the optical intensity correlator. The unique properties of the intensity correlator are stressed by practical demonstration. Specifically, the relative intolerance of the intensity correlator (compared with coherent correlators) to the position of the various components is demonstrated. Also, the spatially incoherent readout light allows the use of a low-optical quality liquid crystal television (LCTV) as a low-cost spatial light modulator. Output results are then presented from the correlator using the LCTV as a dynamic readout device. This provides an updateable hologram as the reference of the correlator which is interrogated at frame rates by the LCTV.

Finally, the temporal discrimination of the novelty filter is combined with the character recognition ability of the intensity correlator. This produces an optical processor which will recognise a particular object but will only register it at the output stage when it is moving.

SYMBOLS

a	Depth of modulation of the photocarrier distribution.
A	Depth of modulation of the ionised-donor distribution.
d	Inter-electrode distance.
D	Diffusion constant, $\left(\mu(kT/q)\right)$
E	Electric field within the sample.
E_D	Diffusion field, $\left(K(kT/q)\right)$.
E_o	Applied electric field, (V_a/d).
E_{sc}	Amplitude of the first Fourier component of the space-charge field
E_Q	Trap-limited electric field, $\left(\frac{qN_A}{K\varepsilon\varepsilon_o}\right)$.
g_o	Generation rate of photocarriers on uniform illumination of intensity I_o, $\alpha\phi\frac{I_o}{\hbar\omega}$.
G	Photocarrier generation distribution, $\alpha\phi\frac{I(z)}{\hbar\omega}$.
$\hbar\omega$	Photon energy.
I_1, I_2	Intensity of the write-beams.
I_3	Intensity of the additional optical bias.
J	Electron current density, $\mathbf{J} = q\mu\mathbf{nE} + qD\nabla.\mathbf{n}$
ℓ	Thickness of the holographic medium in the beam propagation direction.
l_s	Debye screening length, $\left(\sqrt{\frac{\varepsilon\varepsilon_o k_B T}{q^2 N_A}}\right)$.
l_E	Length of electron tightening, $\left(\frac{\varepsilon\varepsilon_o E_o}{qN_A}\right)$.
m	Modulation index, $\frac{2(I_1 I_2)^{1/2}}{I_1 + I_2}$.
m′	Modified modulation index, $\frac{2(I_1 I_2)^{1/2}}{I_1 + I_2 + I_3}$.

n	Number density of electrons in the conduction band.
n_o	Number of electrons generated by the intensity I_o.
n_{ob}	Number of electrons generated by the intensity I_{ob}.
n	Ordinary refractive index.
Δn	Magnitude of photo-induced refractive index change.
N_A	Limiting trap density.
N_D	Number density of donor states.
N_D^+	Number density of ionised donors.
q	Electronic charge.
r_D	Photoelectron diffusion length, $(D\tau)$.
r_E	Electron drift length, $(\mu\tau E_o)$.
r_{ij}	Electro-optic coefficient.
R	Recombination rate of photocarriers, $\gamma_R N_D^+(z)n(z)$.
T_d	Characteristic decay time of the space-charge field.
V_a	Applied voltage.
v_o	Characteristic velocity of the space-charge field.
α	Optical absorption coefficient.
β	Bragg-angle.
δ	Angular deviation from the Bragg-angle.
ε	Relative permitivitty.
ε_o	Dielectric permitivitty.
η	Diffraction efficiency.
Λ	Fringe spacing, $\left(\frac{\lambda_w}{2\sin\theta}\right)$.
λ_r	Wavelength of beam used to 'read' holographic grating.
λ_w	Wavelength of beam used to 'write' holographic grating.
ϕ	Quantum efficiency.
μ	Drift mobility.
θ	Half-angle between the write-beams.
τ	Free-electron lifetime, $\gamma_R N_A$.
τ_M	Maxwell dielectric relaxation time, $\left(\frac{\varepsilon\varepsilon_o}{q\mu n_o}\right)$.
τ_M'	Modified Maxwell dielectric relaxation time, $\left(\frac{\varepsilon\varepsilon_o}{q\mu(n_o + n_{ob})}\right)$

Contents

Chapter One
Introduction

Photorefractive (PR) materials have, for many years, provoked much interest as suitable media for the implementation of optical processing tasks.

In this thesis, details are given of several optical information processors which use photorefractive Bismuth Silicon Oxide (BSO) as a dynamic holographic medium.

As the work presented in this thesis was carried out during the formative years of a new research group in PR materials, the early chapters are dedicated to the characterisation of BSO as to its suitability as a processing material.

The photorefractive effect is introduced in chapter 2 and standard analysis is presented, based on the Kuhktarev band transport equations.

The influence of various extrinsic parameters on the diffraction efficiency such as beam intensities, beam ratios, grating spacings, and applied electric field is examined in chapter 3. It is demonstrated that the experimental results obtained generally conform to the mathematical framework of the Kuhktarev band transport model.

In chapter 4 the properties of BSO which make it particularly attractive for optical processing tasks are assessed. Its natural optical activity and spectral response offer ample opportunity for achieving a good signal-to-noise ratio in optical systems. Geometric factors such as the limitations imposed by the Bragg criterion of the volume hologram are assessed.

During the measurements on the transient behaviour of gratings in BSO it was noted that the influence of optical bias was not as expected from the band transport model. This phenomenon is studied in detail in chapter 5. Transient enhancement is achieved in the diffracted beam, and the ideal conditions for implementing transient devices using this

phenomenon are documented.

In chapter 6 the transient enhancement discussed above is used to implement a novelty filter using BSO, in conjunction with a PC fitted with a Frame-grabber. This produces an overall device which operates at T.V. frame rates and offers good temporal discrimination.

The remainder of the applications presented in chapter 6 is centred on the operation of optical correlation. A coherent joint-transform correlator is initially demonstrated, and results are presented for the case of simple binary amplitude input objects. In section 6.2 an optical intensity correlator is introduced and compared to the coherent correlators which have previously been demonstrated using BSO. This is the first reported demonstration of such a correlator using a real-time holographic medium. The main advantages of the intensity correlator stem from the fact that spatially incoherent light is used to read out the Fresnel holographic filters. This means that the intensity correlator possesses far greater tolerance in the positioning of the various components than its coherent counterparts. Further, due to the spatially incoherent nature of the readout, any phase variations in the readout components will not be relayed to the output plane. This allows a low-optical quality liquid crystal television to be used as a low-cost spatial light modulator, despite its inherent phase inhomogeneities (due to the inhomogeneity of the transparent electrodes and the liquid crystal molecular distribution).

The final section of chapter 6 presents work that was carried out on an optical processor to implement the joint operations of transient enhancement and character recognition. This produces an optical device which not only recognises a specific object, but will only register this 'match' when the object is in motion.

Most of the experiments carried out in this thesis were conducted using a sample of BSO (nominally undoped) of dimensions 10 x 8 x 2 mm^3, which was obtained from Sumitomo Industries. Therefore, unless otherwise stated, all the experiments reported in this thesis refer to this sample.

Chapter Two
The Photorefractive Effect

The photorefractive (PR) effect has been observed in many electro-optic crystals. It is classified as a non-linear optical effect as it permits the interaction of complex wavefronts within the photorefractive medium. It does not suffer from any threshold problems, and can persist at very low (μWcm^{-2}) intensity levels. The attraction of PR crystals is the ability to set up within them holographic gratings which may be indefinitely re-cycled at speeds which are dependent on the material and various extrinsic parameters. This allows the use of these materials to perform optical information processing tasks such as those which have been previously carried out using conventional holographic film with its remote processing requirements and subsequent delays.

The volume refractive index gratings are set up in PR crystals by the following mechanism (see Fig. 2.1). The crystal is illuminated by a spatially varying optical intensity pattern, typically from the interference of two or more coherent beams. The light pattern produces a corresponding inhomogeneous photo-excited charge-carrier distribution. These charge-carriers migrate via drift or diffusion into dark regions of the crystal where they are subsequently re-trapped in localised trapping centres. The resultant charge re-distribution produces a space-charge field which follows the original intensity distribution. This field modulates the refractive index of the crystal, via the linear electro-optic effect, thus producing a refractive index grating within the volume of the crystal which is of the same form as the intensity pattern. This grating can be read out, using another beam, to reproduce the optical information contained in the original writing beams. Thus, the photorefractive effect can be described as a form of 'real-time holography' [2.1].

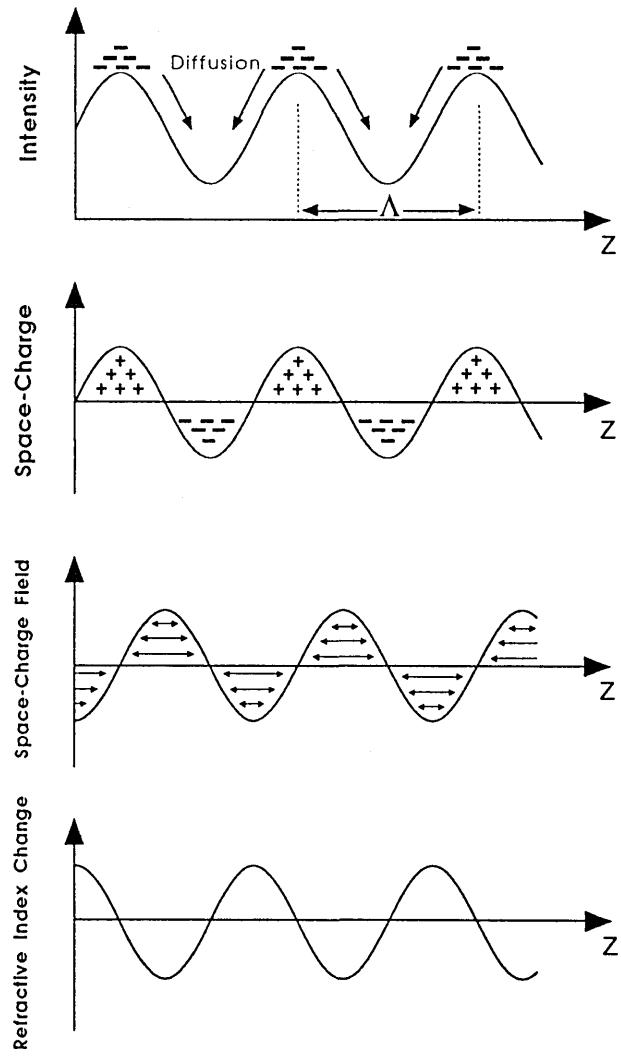

Figure 2.1 Establishment of the space-charge field and resultant refractive index modulation in a photorefractive medium, in the absence of an external applied field and the photovoltaic effect (i.e. the movement of the charge-carriers is by diffusion only).

It is evident from the above discussion that the main requirements for a material to be photorefractive are;

1) It must be a photoconductor able to produce photo-excited charge-carriers at a convenient light wavelength,

2) It must be electro-optic, i.e. be of a non-centrosymmetric crystallographic class,

3) There must be a sufficient number of defects or recombination

centres within the crystalline structure, to serve as localised trapping sites,

4) It must be a poor conductor in the dark to avoid charge leakage which would 'wash-out' the holographic grating.

Although the above criteria may seem rather rigid there are a surprising number of crystals and semiconductors which are classified as being photorefractive. Also, these materials possess a wide range of the material parameters which determine the PR performance. This usually enables a choice to be made of a suitable material for any particular application. The principal photorefractive crystals are the paraelectric $Bi_{12}SiO_{20}$ (BSO) and its isomorphs $Bi_{12}GeO_{20}$ (BGO) and $Bi_{12}TiO_{20}$ (BTO) and the ferroelectric $LiTaO_3$, $Sr_xBa_{1-x}Nb_2O_6$ (SBN), $KNbO_3$ and $BaTiO_3$. The main difference between materials is the magnitude of the relevant electro-optic coefficient, which depends on the crystal orientation. For example, in the most commonly available PR crystals, the electro-optic coefficient can be as high as 1600 pm/V for $BaTiO_3$ and as low as 5 pm/V for BSO. However as the electro-optic coefficient is related to the dielectric constant of the material and the time response of the material is characterised by the dielectric relaxation time there is a distinct trade-off between amplitude and speed of photorefractive response. In this thesis the work concentrates on the use of BSO in optical processing systems. Although BSO exhibits a small PR effect, the sensitivity of modern cameras and detectors means that the output of a system can still be detected providing there is a reasonable signal-to-noise ratio. Optimum conditions for good signal-to-noise are provided by BSO due to its natural optical activity and spectral sensitivity, as will be discussed in chapter 3. Holographic gratings can be updated in BSO at speeds comparable to television frame-rates at reasonable write-beam intensity levels ($mWcm^{-2}$). BSO is also available with good optical quality over a large surface area.

2.1 The Band Transport Model

There have been two prominent models used to describe the photorefractive effect, the band transport model developed by Kukhtarev and co-workers in 1979 [2.2] and the charge 'hopping' model proposed by Feinberg et al in 1980 [2.3]. These models start from different viewpoints; the Kukhtarev model relies on promotion of charge carriers into the conduction band where they migrate to vacant trapping sites, whereas the Feinberg model postulates light-induced hopping of charges from one location to another at a rate which is dependent on the local intensity and electric field. However, for materials such as BSO where the measured lifetime of a charge-carrier in the conduction band is very short compared with the time for build-up of the holographic grating the two models converge in most instances [2.4]. That is to say, although the band transport model requires the mediation of the conduction band for migration, the actual time spent in the conduction band is negligibly small and so it is as if the charges were instantaneously 'moved' from one trapping site to another, as in the hopping model. The Kukhtarev band transport model follows the notation of the partially-compensated semiconductor model [2.5], and has been shown to predict the vast majority of the observed effects of BSO. Therefore, the derivation of the PR transport equations in this thesis will follow the analysis of Kukhtarev et al.

2.1.1 Physical Model

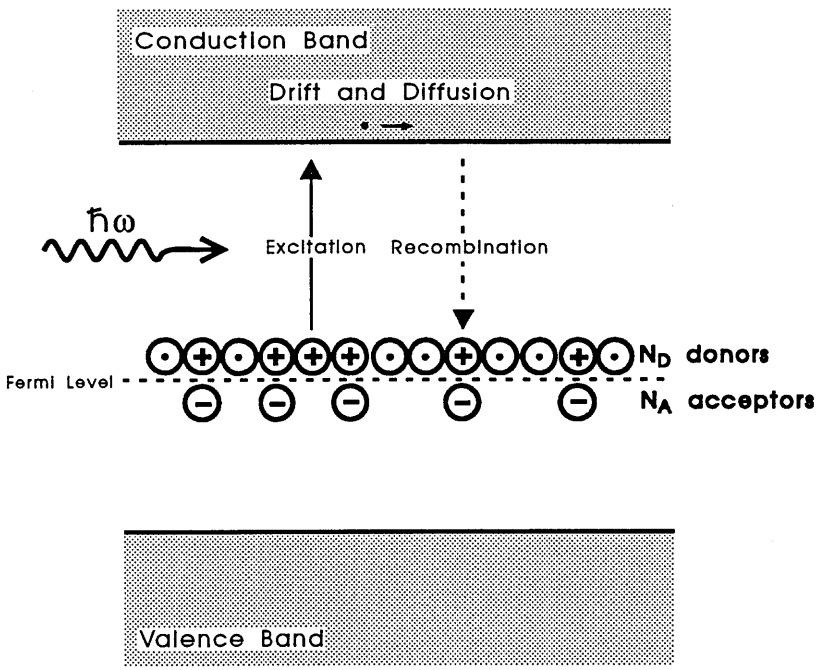

Figure 2.2 A schematic of the physical model used to derive the band transport equations of a partially compensated semiconductor.

The physical model used for the band transport equations is shown in figure 2.2. It is assumed here that electrons are the dominant photo-carrier but, in certain circumstances, holes may also contribute to the effect [2.6]. Photo-excited electrons are ejected from filled donor sites to the conduction band. Here they migrate to dark regions in the crystal before recombining into empty donor sites. The number of filled (neutral) donor states is denoted by N_D ($N_D \sim 10^{19}$ cm^{-3}). The number of empty (ionised) states will then be given by N_D^+ Note that the acceptor sites, of number density N_A, do not play any active role in the photorefractive process but are present merely to ensure that a large number ($\sim 10^{16}$ cm^{-3}) of donors are ionised even in the dark. It is clear then that $N_{D_{dark}}^+ \equiv N_A$. Ultimately it is the number density N_A of vacant donors in the dark which is the limiting factor of the space charge field as only N_A photoelectrons can be accommodated in these donor sites.

2.1.2 Band Transport Equations

The four equations which set up the band transport model are;

i) A continuity equation for the mobile electrons in the conduction band

$$\frac{\partial n}{\partial t} = G - R + \frac{1}{q}\nabla.\mathbf{J} \tag{2.1}$$

where n is the free electron number density
t is time
G is the rate at which electrons are promoted
R is the rate of recombination
q is the electronic charge and
J is the electron current density.

ii) The electron current is composed of terms due to drift and diffusion;

$$\mathbf{J} = q\mu\mathbf{n}\mathbf{E} + qD\nabla.\mathbf{n} \tag{2.2}$$

where μ is the free-electron mobility
n is the free electron distribution
E is the total electric field and
D is the diffusion constant.

iii) a rate equation for the immobile ionised donors

$$\frac{\partial N_D^+}{\partial t} = G - R \tag{2.3}$$

iv) Gauss's Law

$$\nabla.[\varepsilon\varepsilon_o\mathbf{E}] = q(N_D^+ - N_A) \tag{2.4}$$

where ε is the relative permittivity of the material and it is assumed that $n \ll N_D^+, N_A$.

2.2 Solution for Cosinusoidal Illumination

We consider here the common holographic case of an interference pattern generated by the coherent superposition of two plane waves.

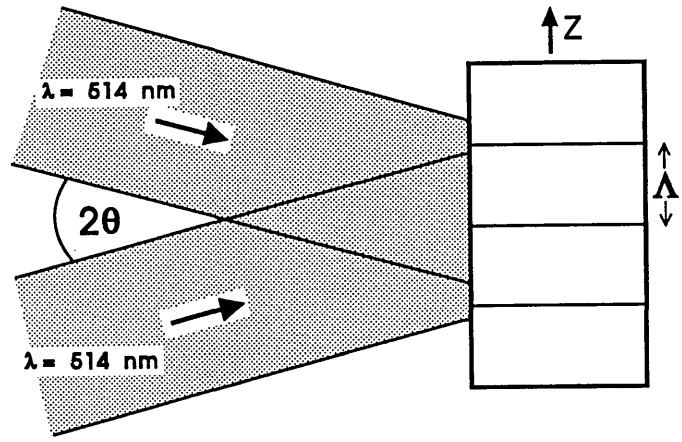

Figure 2.3 Diagram showing the configuration for the interference of two plane waves.

The intensity at the crystal will therefore be of the form;

$$I(z) = I_o[1 + m\cos(Kz + \psi_o)] \qquad (2.5)$$

where m is the modulation index given by $m = \frac{2(I_1 I_2)^{1/2}}{I_o}$, $I_o = I_1 + I_2$, $K = 2\pi/\Lambda$, and Λ is the fringe spacing given by $\Lambda = \frac{\lambda_{514}}{2\sin\theta}$ (see Figure 2.3). Rewriting equation (2.5) as a Fourier series expansion excluding second order terms and higher yields;

$$I(z) = I_o + \frac{I_o}{2}(me^{iKz} + m^* e^{-iKz}) \qquad (2.6)$$

where $I_o m = I_o |m| \exp(i\psi_o)$. ψ_o is an arbitrary phase shift of the fundamental component from the z = 0 origin.

We now assume that the spatial modulation of all the material

parameters can be adequately described by the d.c. and fundamental components of a Fourier series expansion. This approximation (linear in m approximation) has been shown to be valid for small values of m; i.e. $m \leq 0.6$ [2.4].

The resulting distribution of photoelectrons in the conduction band is thus of the form;

$$n(z) = n_o + \frac{n_o}{2}(ae^{iKz} + a^*e^{-iKz}) \tag{2.7}$$

where n_o is the number of photoelectrons that would be generated if the crystal were illuminated with uniform illumination of intensity I_o. The parameter a is a measure of the modulation of the photoelectron distribution. The form of the ionised donor distribution will then be given by;

$$N_D^+(z) = N_A + \frac{N_A}{2}(Ae^{iKz} + A^*e^{-iKz}) \tag{2.8}$$

where A is the modulation depth of the ionised-donor distribution. The spatial variation of the electric field in the sample is given by;

$$E(z) = E_o + E_{sc}(z) = E_o + \frac{1}{2}(E_{sc}\, e^{iKz} + E_{sc}^*\, e^{-iKz}) \tag{2.9}$$

where E_o is any external field applied to the crystal parallel to the grating vector (i.e. perpendicular to the grating planes), and E_{sc} is the amplitude of the fundamental component of the space-charge field. Note that an incoherent beam diffracted from a refractive index grating can be sensitive to the amplitude of the space-charge field and not its relative position. Since this thesis deals almost exclusively with such incoherent diffraction the prime interest here is in the temporal development of E_{sc}.

Equations (2.1-2.4) can be simplified by noting that in this instance all the material parameters vary only in the z direction. Thus they can be rewritten as;

$$\frac{\partial n}{\partial t} = G - R + \frac{1}{q}\frac{\partial J(z)}{\partial z} \tag{2.10}$$

$$J(z) = q\mu n(z)E(z) + qD\frac{\partial n(z)}{\partial z} \tag{2.11}$$

$$\frac{\partial N_D^+(z)}{\partial t} = G - R \tag{2.12}$$

$$\varepsilon\varepsilon_o\frac{\partial E(z)}{\partial z} = q(N_D^+(z) - N_A) \tag{2.13}$$

Note also that G will be given by;

$$G = \alpha\phi\frac{I(z)}{\hbar\omega} \tag{2.14}$$

α is the optical absorption, ϕ is the quantum efficiency, $\hbar\omega$ is the photon energy, and thermal generation is neglected. The recombination rate, R, is linearly proportional to the number of free electrons and the probability that a trap is empty.

$$R = \gamma_R N_D^+(z)n(z) \tag{2.15}$$

where γ_R is the recombination constant. Equations (2.10 - 2.13) are non-linearly coupled and as such are difficult to solve analytically without normalising the physical parameters [2.4]. However they are readily solved using some standard simplifying assumptions which have proved generally to be applicable to BSO. The solution that follows is based on the work of Petrov, Stepanov and Khomenko [2.7, 2.8] and is executed under what has been termed the 'quasi-stationary' approximation. This relies on the fact that the lifetime of the photo-carrier is very short (μs) compared with the time taken for the grating to build up (ms). Thus we can treat the free-electron density as stationary at any moment of the grating build-up. In other words, in equation (2.10) we can set $\frac{\partial n}{\partial t} = 0$. Clearly this simplifies (2.10) such that,

$$G - R = -\frac{1}{q}\frac{\partial J(z)}{\partial z} \tag{2.16}$$

By substituting equations (2.6-2.9) into (2.16) and performing the differentiations the following expression is obtained;

$$mg_o - (a + A)n_o\tau^{-1} = -iK\mu n_o(aE_o + E_{sc}) + K^2Dan_o \tag{2.17}$$

where $g_o = \alpha\phi\frac{I_o}{\hbar\omega}$ (note that $n_o = g_o\tau$), and τ is the free electron lifetime, $\tau = 1/\gamma_R N_A$ [2.4]. Performing the same operation on equations (2.12) and (2.13), respectively yields;

$$\frac{\partial A}{\partial t}N_A = mg_o - (a + A)n_o\tau^{-1} \tag{2.18}$$

and

$$iK\varepsilon\varepsilon_o E_{sc} = qAN_A \tag{2.19}$$

Expressions for a and A can be obtained from equations (2.17) and (2.19) respectively. Substituting into equation (2.18) produces the following form for the complex amplitude of the space-charge field,

$$\frac{\partial E_{sc}}{\partial t} = -\frac{m(E_o + iE_D) + E_{sc}(1 + K^2l_S^2 - iKl_E)}{\tau_M(1 + K^2r_D^2 - iKr_E)} \tag{2.20}$$

where $E_D = K\left(\frac{D}{\mu}\right)$ is the diffusion field (defined by the Einstein relations), $r_D = D\tau$ is the photoelectron diffusion length, $r_E = \mu\tau E_o$ is the drift length, $l_S = \sqrt{\frac{\varepsilon\varepsilon_o k_B T}{q^2 N_A}}$ is the Debye screening length, $l_E = \frac{\varepsilon\varepsilon_o E_o}{qN_A}$ is the length of electron "tightening" by the applied electric field, E_o and $\tau_M = \frac{\varepsilon\varepsilon_o}{q\mu n_o}$ is the Maxwell dielectric relaxation time. Equation (2.20) is the general expression which describes the time evolution of the amplitude of the space-charge field. Particular cases of practical interest can now be examined.

2.2.1 Steady-State Solution

The steady-state solution of the space-charge field is easily obtained from (2.20) by considering the case for $\frac{\partial E_{sc}}{\partial t} = 0$. This produces the following expression;

$$E_{sc} = - \frac{m(E_o + iE_D)}{1 + K^2 l_S^2 - iKl_E} \tag{2.21}$$

Note that the steady-state solution for the space-charge field contains no reference to the absolute intensities of the writing beams involved.

2.2.2 Formation of the Space-Charge Field

Equation (2.20) is a partial differential equation of the form $\frac{\partial E_{sc}}{\partial t} = a + bE_{sc}$. This has a general solution of the form, $E_{sc}(t) = - \frac{a}{b}(1 - e^{bt})$. Therefore, by inspection of (2.20) we can see that the space-charge field is represented by the following function of time;

$$E_{sc}(t) = - \frac{m(E_o + iE_D)}{1 + K^2 l_S^2 - iKl_E} \left[1 - \exp\left(- \frac{(1 + K^2 l_S^2 - iK l_E)}{\tau_M (1 + K^2 r_D^2 - i K r_E)} t \right) \right] \tag{2.22}$$

This expression tends to (2.21) as $t \to \infty$, as required. The argument of the exponential function in (2.22) is complex; this predicts that the formation of the grating will exhibit a damped oscillatory response. This will be fully developed in later chapters.

2.2.3 Decay of the Space-charge Field

In general the space-charge field would takes several days to dissipate if it were left in the dark. Usually the space-charge field is erased by uniform illumination of the crystal. We can examine the crystal response to this by letting m = 0 in equation (2.20), which produces the following expression;

$$\frac{\partial E_{sc}}{\partial t} = - \frac{E_{sc}(1 + K^2 l_S^2 - i K l_E)}{\tau_M(1 + K^2 r_D^2 - iK r_E)} \tag{2.23}$$

This is a differential equation of the form $\frac{\partial E_{sc}}{\partial t} = aE_{sc}$ and so has a solution of the form $E_{sc}(t) = E_{sc}(0)e^{-at}$ where $E_{sc}(0)$ is the value of E_{sc} at t = 0. Therefore, by inspection of (2.23) the solution for the light-induced decay of the space-charge field is given by;

$$E_{sc}(t) = E_{sc}(0)\exp\left[- \frac{t(1 + K^2 l_S^2 - iK l_E)}{\tau_M(1 + K^2 r_D^2 - i K r_E)} \right] \tag{2.24}$$

Equation (2.24) can be decomposed into terms with real and imaginary arguments, i.e.

$$E_{sc}(t) = E_{sc}(0)\exp\left\{ - \frac{t[(1 + K^2 r_D^2)(1 + K^2 l_S^2) + K^2 r_E l_E]}{\tau_M[(1 + K^2 r_D^2)^2 + K^2 r_E^2]} \right\}$$

$$.\exp\left\{ - \frac{it[(1 + K^2 l_S^2) K r_E - (1 + K^2 r_D^2) K l_E]}{\tau_M[(1 + K^2 r_D^2)^2 + K^2 r_E^2]} \right\} \tag{2.25}$$

The general form of equation 2.25 is given by;

$$E_{sc}(t) = E_{sc}(0).\exp\left\{ - \frac{t}{T_d} \right\}.\exp\left\{ -iK\omega_o t \right\} \tag{2.26}$$

The second term of (2.26) has a purely imaginary argument. This has been interpreted [2.7] as a uniform motion of the hologram amplitude whilst it is decaying. The characteristic decay time, T_d , is then given by;

$$T_d = \frac{\tau_M[\ (1 + K^2 r_D^2)^2 + K^2 r_E^2\ ]}{(1 + K^2 r_D^2)(1 + K^2 l_S^2)\ + K^2 r_E l_E} \qquad (2.27)$$

and the uniform drift of the hologram, in the applied field E_o, will be at the characteristic velocity, v_o , given by;

$$v_o = \frac{r_E(1 + K^2 l_S^2)\ - l_E(1\ + K^2 r_D^2)}{\tau_M[\ (1 + K^2 r_D^2)^2 + K^2 r_E^2\ ]} \qquad (2.28)$$

This uniform motion of the hologram at low values of m has been suggested as an explanation for the resonant enhancement of photorefractive gratings in BSO. Resonant enhancement involves moving the holographic fringes through the crystal in conjunction with the application of a d.c. electric field across the crystal. It was hypothesised in reference 2.7 that efficient recording of the hologram can only occur when the holographic fringes move at the same uniform velocity as the holographic grating; i.e. at v_o.

2.3 Refractive Index Gratings

It has been shown that light-induced charge migration in a photoconductor can produce a spatially varying electric field within the volume of the crystal. If the photo-conducting medium is also electro-optic, then this electric field will modulate the refractive index. As the original intensity pattern that created the space-charge field is generally sinusoidal in form, the refractive index variation will also be periodic and thus acts as a sinusoidal refractive index grating.

BSO is in fact a well-known electro-optic material, and has been used in many applications including the implementation of a spatial light modulator [2.9]. Its electro-optic and related properties, such as elasto-opticity, have been extensively studied [2.10-2.12]. BSO as a photorefractive material is commonly used in one of two different orientations, depending on the application. For a space-charge or modulating field in the crystallographic z-direction, the following axes of refractive index modulation will be produced [2.13];

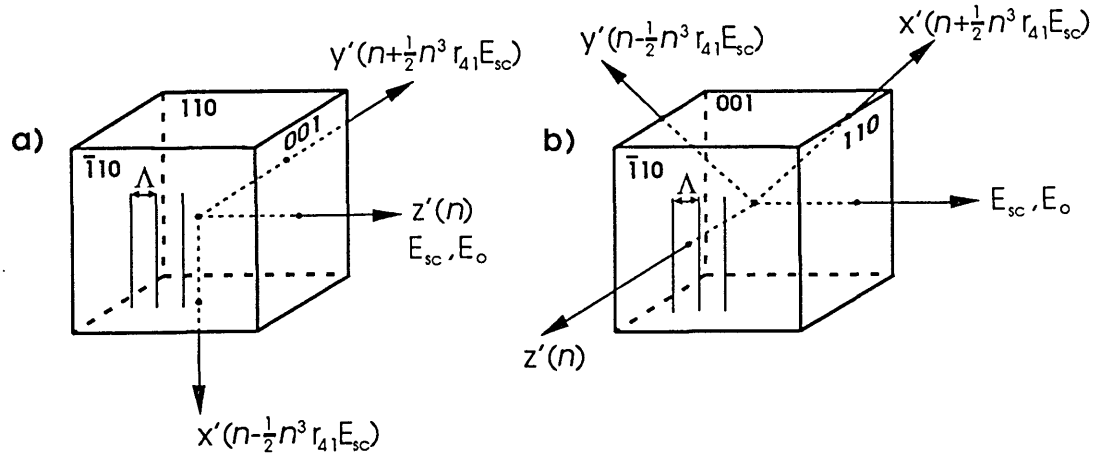

Figure 2.4 Orientations of BSO which are used for electro-optic modulation. n is the ordinary refractive index and r_{41} is the appropriate electro-optic co-efficient.

It is seen from figure 2.4 that a 'read-beam' incident on the T10 face will encounter a different set of refractive index axes, depending on the crystal's orientation. This has proved to be critical in the field of optical information processing [2.13]; the orientation in figure 2.4 a) is known as the '2-wave mixing orientation' and that of 2.4 b) is correspondingly known as the '4-wave mixing orientation'. The 2-wave mixing orientation produces non-reciprocal energy transfer which has been widely documented [2.14]. The 4-wave mixing orientation produces the largest magnitude of refractive index modulation and is therefore the orientation favoured for the work of this thesis. For the 4-wave mixing orientation the magnitude of refractive index modulation is given by [2.15];

$$\Delta n = n^3 r_{41} |E_{sc}| \tag{2.29}$$

where $|E_{sc}|$ is the magnitude of the space charge field.

Chapter Three
Characterisation Measurements

In this chapter some of the basic features of the photorefractive effect are experimentally demonstrated.

3.1 Diffraction Efficiency

3.1.1 Experimental Configuration

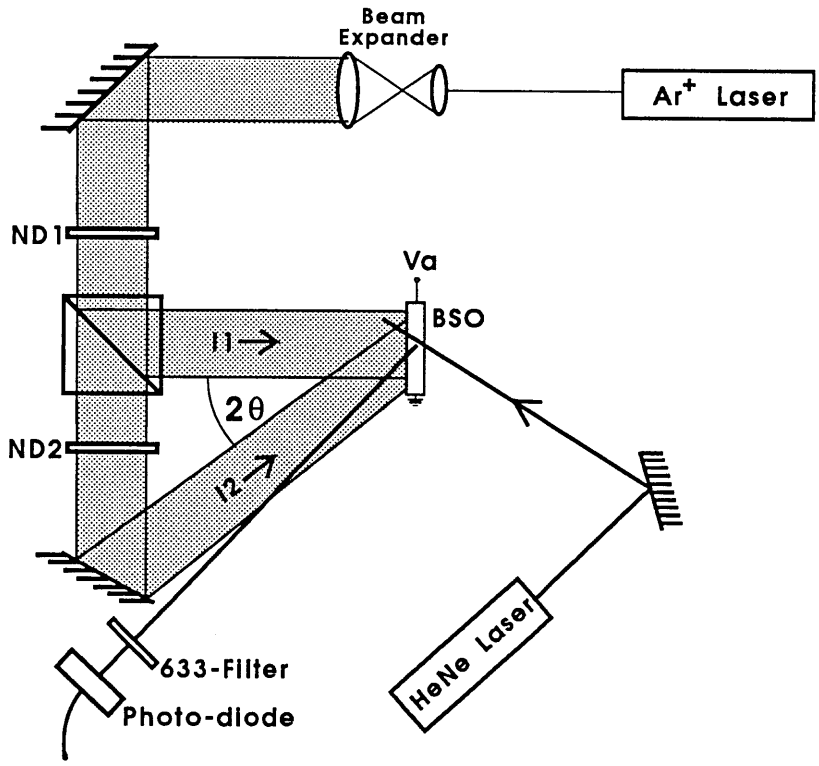

Figure 3.1 Experimental configuration for basic diffraction efficiency measurements. $2\theta = 26^{\circ}$, ND1-2, neutral density filters.

As explained in chapter 2, refractive index gratings can be formed within the volume of BSO, via the photorefractive mechanism. The resultant grating characteristics such as amplitude and speed of response can be investigated by diffracting a laser beam from the grating. The basic experimental configuration for producing such refractive index gratings is given in figure 3.1. Note that these are

the experimental conditions that were analysed in chapter 2; i.e. the gratings are generated by a sinusoidal intensity pattern formed by the interference of two coherent beams. In this case both beams are derived from the same argon-ion laser operating single-mode at 514.5 nm. A HeNe beam with an output intensity of a few milliwatts at 632.8 nm was used as the 'probe-beam'. The intensity of light diffracted from the grating is measured using a photo-detector connected to a power meter. The diffracted intensity is a direct indication of the amplitude of photorefractive response of the BSO crystal. The HeNe output at 633 nm is energetically insufficient to greatly affect the photorefractive gratings and so, together with its low intensity, provides non-destructive monitoring. The definition of diffraction efficiency, (η), used here is that of the diffracted intensity divided by the intensity of the HeNe beam transmitted through the crystal with no grating present. This allows comparison to be made between different BSO crystals which have different values of optical absorption.

3.1.2 Analysis

The analysis of the diffraction efficiency of PR materials is usually conducted using coupled wave theory, as developed by Kogelnik in 1969 [3.1]. For a volume phase transmission grating, as is the case for PR media, the diffraction efficiency is given by [3.2];

$$\eta = \left| -i\frac{\exp(-i\xi)\sin(\xi^2 + \nu^2)^{1/2}}{(1 + \xi^2/\nu^2)^{1/2}} \right|^2 \qquad (3.1)$$

where ξ and ν are parameters convenient for the problem. ξ is defined such that;

$$\xi = \delta\frac{2\pi}{\lambda_r}\ell\sin\beta \qquad (3.2)$$

where n is the normal refractive index, ℓ is the thickness of the medium, β is the Bragg angle appropriate to the wavelength of laser light used to probe the grating, λ_r, such that, $2\Lambda\sin\beta = \lambda_r$, and δ is the angular deviation of the probe-beam from the Bragg angle. The parameter ν is defined by;

$$\nu = \frac{\pi\Delta n\ell}{\lambda_r\cos\beta} \qquad (3.3)$$

It can be seen from inspection of equations 3.2 and 3.3 that ξ is in fact a measure of the deviation of the read beam from the Bragg angle, and ν is a measure of the magnitude of the depth of hologram modulation.

Only when the read beam is incident at the Bragg angle will optimum diffraction efficiency be permitted. For the remainder of this chapter it is assumed that the read beam is always incident at the Bragg angle. This was a condition that was experimentally justified by careful adjustment of the angle of incidence of the read beam such that maximum diffraction efficiency was obtained at all times. In this case, $\delta = 0 \rightarrow \xi = 0$. Thus, equation 3.1 is simplified to;

$$\eta = \sin^2\left(\frac{\pi \Delta n \ell}{\lambda_r \cos\beta} \right) \tag{3.4}$$

It should now be obvious (by inspection of equation 2.29) that the diffraction efficiency of gratings set up in any particular photorefractive material is determined by the magnitude of the space-charge field.

3.2 Steady State Results

From equation (2.21) the complex amplitude of the steady-state space-charge field was given by;

$$E_{sc} = - \frac{m(E_o + iE_D)}{1 + K^2 l_S^2 - iKl_E} \tag{3.5}$$

Using the definitions of E_D and E_Q (E_D is the field generated by diffusion of the charge-carriers, and $E_Q = \frac{eN_A\Lambda}{2\pi\varepsilon\varepsilon_o}$ is the trap-limited field, i.e. the maximum electric field that can be supported by the trap density N_A), equation (3.5) can be rewritten as;

$$E_{sc} = -mE_Q \frac{(E_o + iE_D)}{E_Q + E_D - iE_o} \tag{3.6}$$

Therefore, using the identity $|z_1/z_2| \equiv |z_1|/|z_2|$ where z_1 and z_2 are both complex, the well-known form for the magnitude of the space-charge field is easily obtained;

$$|E_{sc}| = mE_Q\left[\frac{E_o^2 + E_D^2}{(E_Q + E_D)^2 + E_o^2}\right]^{1/2} \tag{3.7}$$

Clearly it is desirable to control the extrinsic parameters contained in equation (3.7) so that the optimum conditions can be set up for any particular application.

3.2.1 Write-Beam Ratio

It is convenient to first consider some of the fundamental properties of the photorefractive effect without the added complication of an externally applied electric field. Thus, for these conditions, equation (3.7) simplifies to;

$$|E_{sc}| = m\frac{E_Q E_D}{E_Q + E_D} \tag{3.8}$$

The most important feature of equation (3.8) is that there is no direct scaling of $|E_{sc}|$ due to the absolute intensity of the writing beams, I_1 and I_2. It should be evident from the expression for m, the modulation index, that $0 \leq m \leq 1$, and that m will be equal to one when the writing beams are of equal intensity. Thus we expect the diffraction efficiency to be a maximum when $I_1 = I_2$.

To establish experimental verification of the above conclusion the ratio between the two write beams was varied by inserting various neutral density (N.D.) filters in the location ND2 in Fig. 3.1. This produced write-beam ratios from about 20:1 to 1:20. The experimental results obtained are shown in Figure 3.2 and show that indeed the intensity of the diffracted beam reaches a maximum for $I_1 = I_2$.

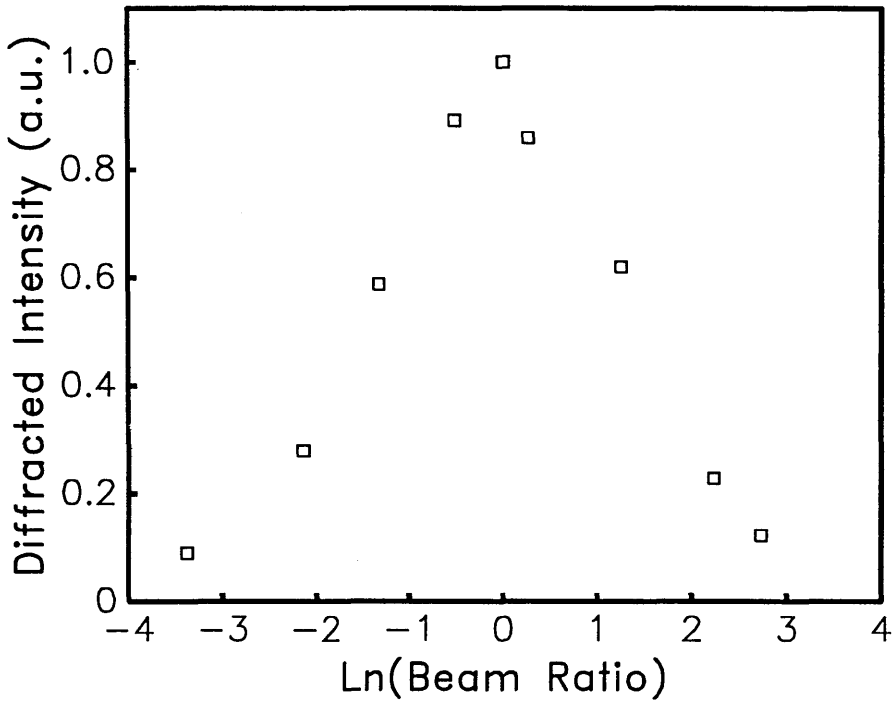

Figure 3.2 Variation of diffracted beam intensity with write-beam ratio. $\Lambda = 1$ μm, $E_o = 0$.

As $\eta < 5\%$ for all the experiments reported here, equation (3.4) can be represented by the small angle approximation, $\theta = \sin\theta$. Therefore, in this approximation, $\eta \alpha (\Delta n)^2$ and so from (2.29) and (3.4) we would expect that diffraction efficiency is proportional to the square of m.

To test this conclusion, the modulation index between the two writing beams was varied by the insertion of different values of N.D. filters at the location ND2 in Fig. 3.1. Plotting the resultant diffracted intensity against the square of m produces the expected linear relationship, as seen in Figure 3.3. The departure from a

linear relationship, witnessed at the higher values of m, demonstrates the lack of validity, in this region, of the linear-in-m approximation used to derive (2.20).

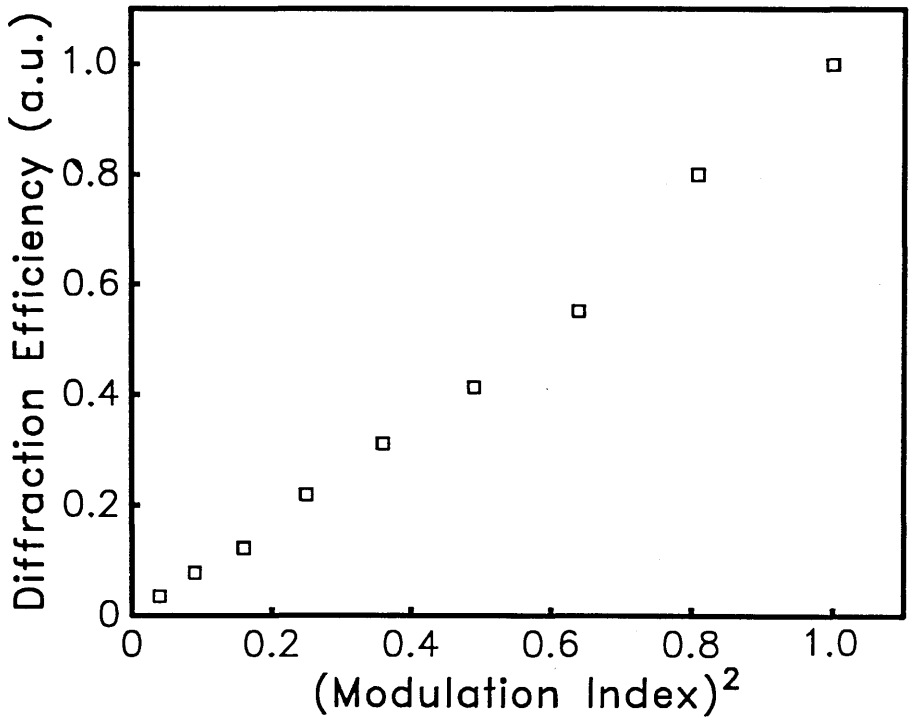

Figure 3.3 Variation of diffraction efficiency with the square of the modulation index. Λ = 1 μm, E_o = 0.

3.2.2 Write-Beam Intensity

To observe how the diffraction efficiency behaves as the absolute intensity of the write beams is increased, several values of N.D. filter were inserted at location ND1, whilst maintaining unity modulation between the writing beams. We can see from Figure 3.4 that there is no minimum amount of optical energy required to initiate the P.R. effect; indeed, the diffracted beam is detectable down to the limit of the optical detector. The effect saturates relatively quickly at low light intensities, corresponding to complete filling of the available trapping centres, of density N_A. The diffracted intensity saturates at ~ 2 mWcm^{-2} which is in common with the findings of other workers [3.3].

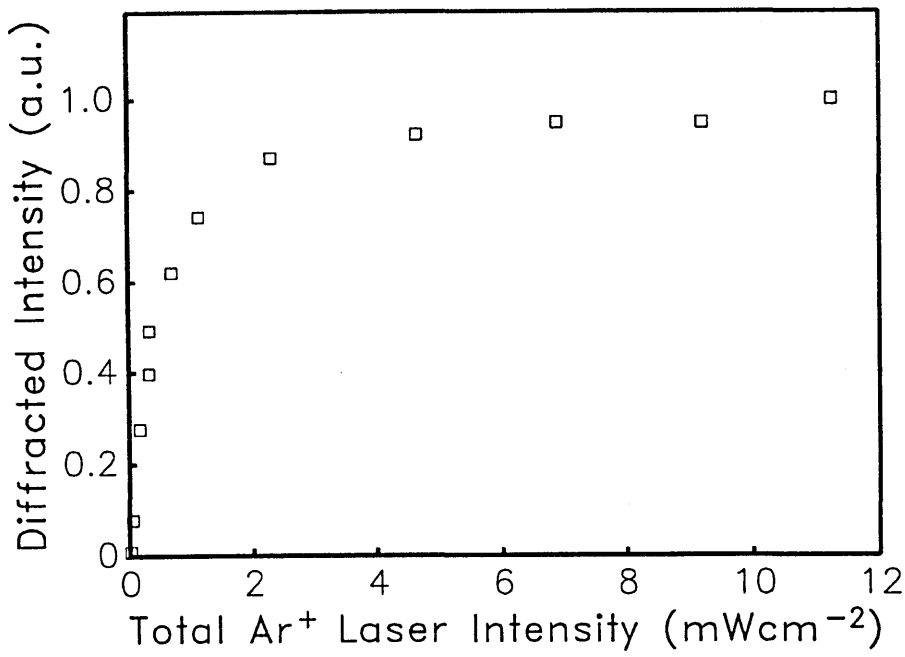

Figure 3.4 Diffracted beam intensity as a function of the overall write beam intensity. Λ = 1 μm, E_0 = 0, I_1 = I_2.

3.2.3 External Applied Field

It can be seen from expression (3.7) that applying an external electric field will have a significant effect on the magnitude of the space-charge field. In BSO this has a dramatic effect on the diffraction efficiency, with fields of about 5 kV/cm increasing η by a factor of ten. In applications of optical information processing using BSO there is invariably an electric field applied across the crystal. Nearly 100 % diffraction efficiency has been achieved with a combination of a 10 mm long crystal and ~ 15 kV/cm applied across it [3.4].

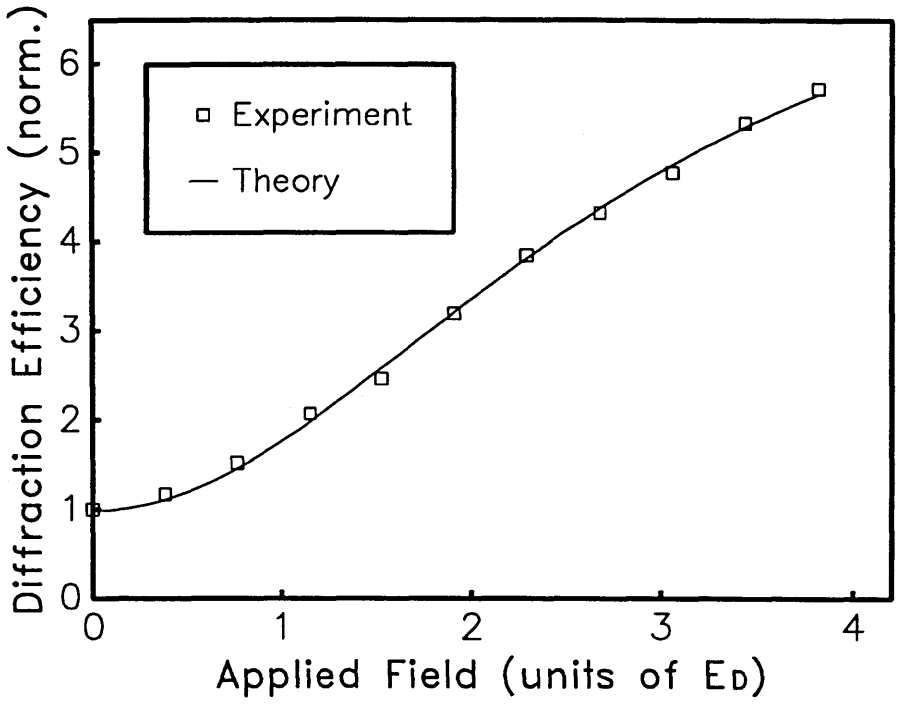

Figure 3.5 Diffraction efficiency as a function of applied electric field. Λ = 1 μm, $I_1 = I_2$.

Figure 3.5 shows the effect on diffraction efficiency of applying an external field to the BSO crystal. The quadratic nature is clearly visible with the effect of saturation noticeable at the higher applied fields; this was not observed with all BSO crystals, suggesting varying values of N_A.

For this particular crystal the electrodes were deposited onto the crystal during the production process, although silver-painted electrodes prove just as effective, due to the high resistivity of the crystal.

From inspection of equation (3.7) we can see that curve-fitting to the data can produce a value for N_A through E_Q. As E_D contains no physical parameters and is dependent only on the fringe spacing, which can be accurately measured at 1 μm, the applied field is scaled in units of E_D. The diffracted intensity is normalised to the value without the applied field. The curve-fitting produces a value for N_A of 3.1×10^{16} cm^{-3} which agrees well with values obtained elsewhere for other crystals [3.5].

3.2.4 Fringe Spacing

The variation of diffraction efficiency with holographic fringe spacing is implicitly contained in expression (3.7); due to E_D and E_Q being spatial frequency dependent.

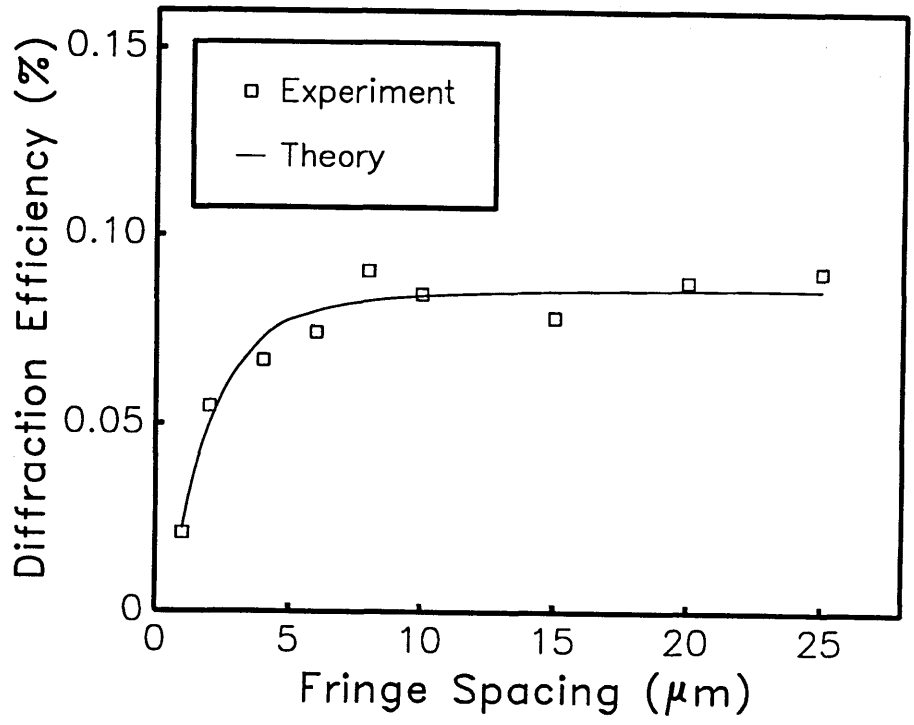

Figure 3.6 Diffraction efficiency as a function of fringe spacing. E_o = 6.3 kVcm^{-1}, $I_1 = I_2$.

The variation of diffraction efficiency with fringe spacing is shown in Fig 3.6. It should be noted that there is a reasonably flat response for $\Lambda \geq 5$ μm. This is because in this region the trap-limited electric field (being linearly dependent on Λ) is sufficiently large to allow $E_{sc} \rightarrow E_o$. Clearly the spatial frequency ($1/\Lambda$) response is relevant to the use of BSO for image processing tasks and as such will be discussed later in chapter 4.

Again, curve-fitting to the data will produce a value for N_A by allowing E_Q and an arbitrary scaling factor to vary in (3.7) The scaling factor allows for factors such as optical activity, multiple

beam reflections and non-linearities in the space-charge field, which all cause the diffraction efficiency to be less than the theoretical value. For this data a value of $N_A = 4.3 \times 10^{16}$ cm^{-3} is obtained via a least-squares fit to the non-linear equation. As this and the previous curve fitting were carried out using independent data we can say with reasonable certainty that for this crystal; $N_A = 3.7 \pm 0.6 \times 10^{16}$ cm^{-3}.

3.3 Transient Results

As diffraction efficiency is determined solely by the magnitude of the space-charge field, the transient properties will be given by the time-evolution of E_{sc}, given by equation (2.20). Therefore, as mentioned previously, the temporal properties of gratings in photorefractive media are characterised by the dielectric relaxation time, $\tau_M = \frac{\varepsilon\varepsilon_o}{q\mu n_o}$. It should be noted that τ_M is defined by the dielectric constant divided by the average photoconductivity, $q\mu n_o$. Thus we expect the time response of a photorefractive material to be determined by its bulk photoconductivity. It is therefore of interest to consider the conductivity of BSO as a function of incident intensity.

3.3.1 Photoconductivity of BSO

As stated above, the conductivity, σ, of a single-species semiconductor is given by;

$$\sigma = q\mu n_o \tag{3.9}$$

Due to the relative values of excitation and trapping centre densities (reference 3.2) it can usually be assumed that the excitation and recombination process is linear. Under these conditions, and ignoring thermal excitation, the average density of electrons in the conduction band at any time is given by $n_o = g_o\tau$. Substituting for g_o from equation (2.14) yields;

$$n_o = \alpha\phi \frac{I_o}{\hbar\omega}\tau \tag{3.10}$$

Thus the average photoconductivity is, as would be expected, linearly proportional to the average intensity at the crystal.

An experiment was carried out to determine the validity of the

above conclusion. This required that one beam only, of uniform intensity, was allowed to strike the crystal. Therefore, beam I_2 in Figure 3.1, was blocked leaving only I_1 to strike the crystal at normal incidence. This beam was sufficiently large in spatial extent that the Gaussian profile beam could be considered approximately constant in intensity across the area of the crystal. Therefore, the photoconductivity is considered uniform throughout the crystal in this measurement. An electrometer was connected in series with the crystal to measure the induced photocurrent and the voltage supply was set to 5 kV. The actual intensity striking the crystal was varied by the use of N.D. filters and measured using a calibrated Newport power meter with photodiode.

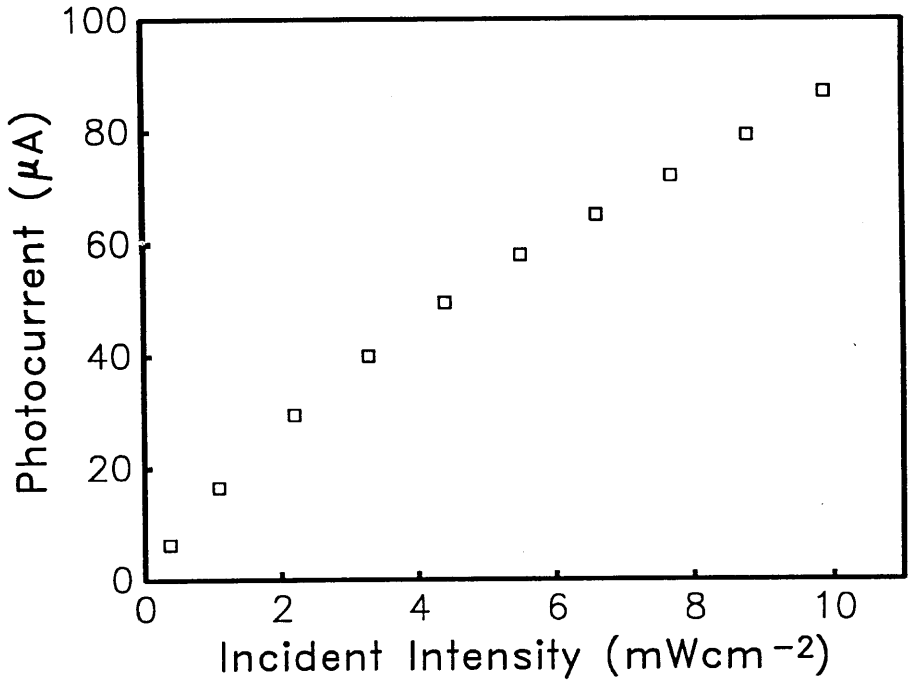

Figure 3.7 Photocurrent through the crystal as a function of incident intensity. V_a = 5 kV, I_2 = 0.

Figure 3.7 shows the behaviour of the photocurrent with incident intensity. The linear relationship expected is seen to be approximated by the data. It is believed that the sub-linearity at the higher intensity levels should be attributed to non-ohmic behaviour of the electrodes at the applied voltage, (5kV), rather than any non-linear excitation and recombination process. This was established by first setting the Ar^+ laser beam at the highest intensity level and varying

the applied voltage, which produced the same sub-linear behaviour (Fig. 3.8 a); then substituting a standard 50 MΩ resistor for the crystal to verify that the voltage supply and circuit were 'well-behaved' (Figure 3.8 b).

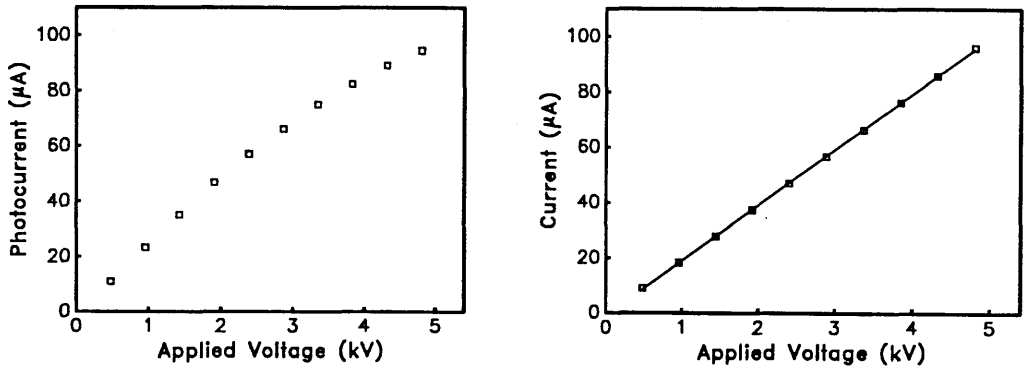

Figure 3.8 Variation of photocurrent as a function of applied voltage a) at a fixed level of incident intensity b) for a fixed standard resistance.

Having seen that the conductivity of BSO is approximately linearly proportional to the level of incident excitation, from equation (2.20) it is expected that the time response of a photorefractive crystal is inversely proportional to the average intensity.

3.3.2 Experimental Configuration

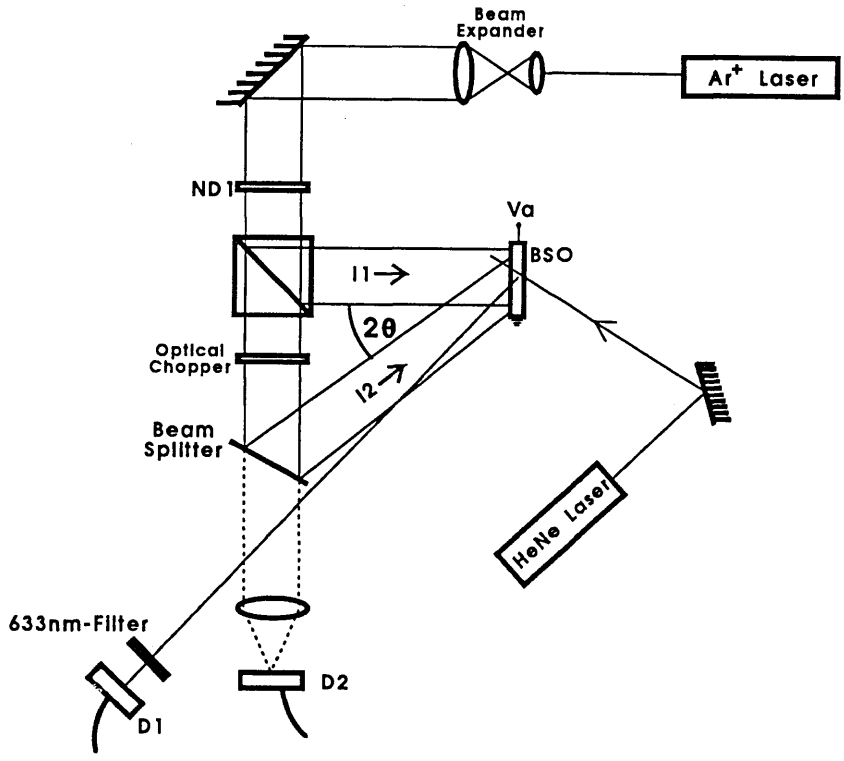

Figure 3.9 Experimental configuration for conducting transient experiments on the BSO sample. $2\theta = 26^{\circ}$, $I_1 = I_2$.

Experiments were carried out to investigate the transient properties of BSO using the system given in Figure 3.9. This set-up is similar to that of Fig. 3.1 with the exception that an optical chopper is used to alternately pass one of the writing beams. When both beams are present at the crystal a grating is written but when beam I_2 is blocked the grating will be erased by the beam I_1. Therefore the grating is cycled through a write-erase sequence. The diffracted intensity detected at photo-diode 1 therefore shows the creation and erasure of gratings. A typical trace is shown in Fig 3.10. Note that this particular trace was obtained with no electric field across the crystal. The introduction of an external electric field causes complications which will be discussed later.

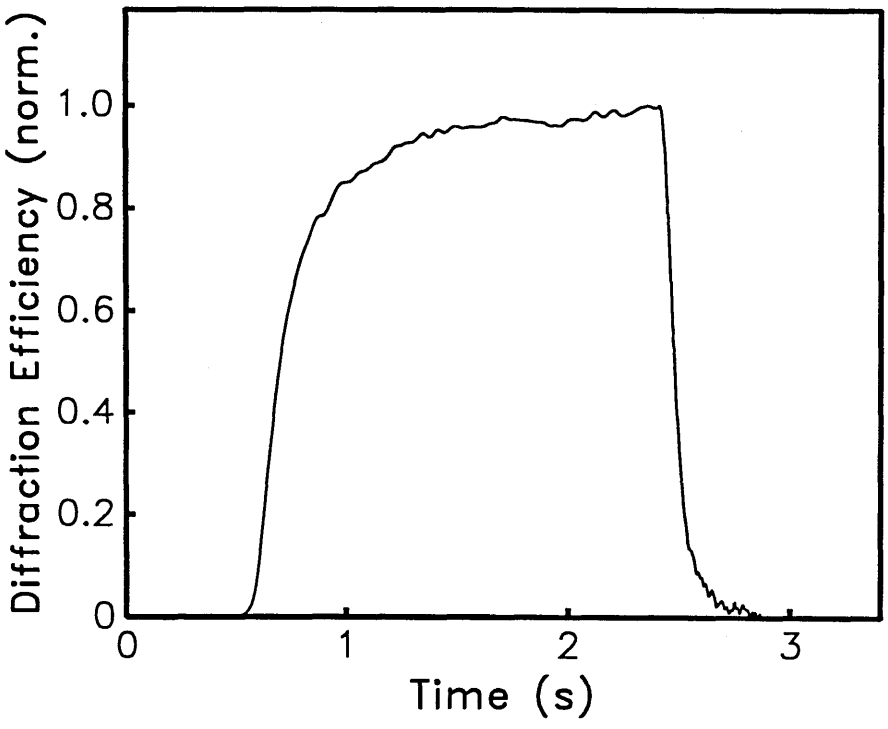

Figure 3.10 Example of write-erase cycle of holographic grating. Λ = 1 μm, $I_1 = I_2$, V_a = 0 V.

It is seen from Fig. 3.9 that I_2 continues beyond the beam splitter and is subsequently incident on a second photo-diode. The signal from this diode is used as a trigger for the digital storage oscilloscope in order that a series of traces may be captured for averaging. The rise and decay times were calculated from the acquired data simply by taking the time taken for the diffracted intensity to reach $(1\text{-}e^{-1})$ and e^{-1} of the steady-state value, for the rise and decay times respectively. The accuracy of this method proved sufficient for these elementary experiments although more stringent methods required later included; chopping the beam at the mutual focal plane of a two-lens system and performing a curve fitting algorithm on the acquired digital data to obtain a value for the response time.

3.3.3 Write-Beam Intensity

The first experiment to be carried out on the transient properties

was that discussed in section 3.3.1; the variation of the response time with write-beam intensity. This was undertaken by inserting various N.D. filters in the system at location ND1, to change the overall intensity at the crystal.

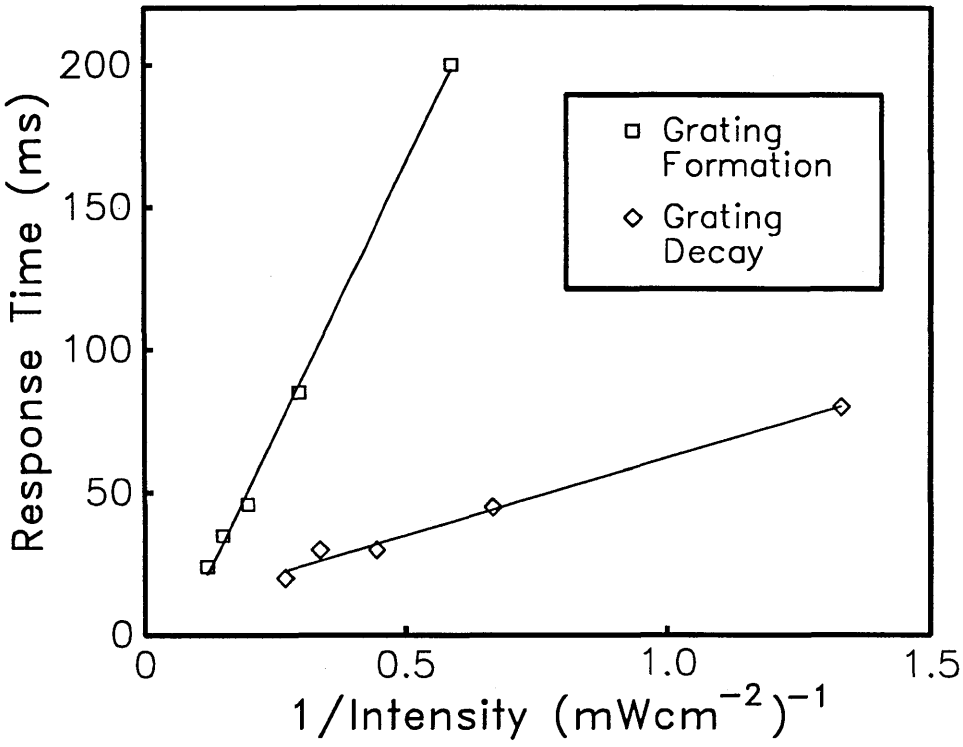

Figure 3.11 Variation of response time of the BSO crystal as function of overall write-beam intensity. Λ = 1 μm, I_1 = I_2, V_a = 0 V.

The experimental results for the variation of response time with intensity are given in Figure 3.11. As expected, both the rise and decay times are inversely proportional to the combined write-intensity. However, note that the two curves do not lie on the same straight line, i.e. the rise and decay times should be considered different in nature.

3.3.4 Applied Electric Field

Equation (2.27) predicts that there will be a fairly pronounced slowing down of the response time of BSO on application of an external electric field. This was observed experimentally and the results are shown in Fig. 3.12 for the decay response times only. The reasons for not presenting the data on grating formation times is that when an

electric field is applied the diffraction efficiency of gratings in BSO becomes very erratic, and therefore the acquisition of a 'smooth' exponential build-up would have been determined by a fairly subjective choice.

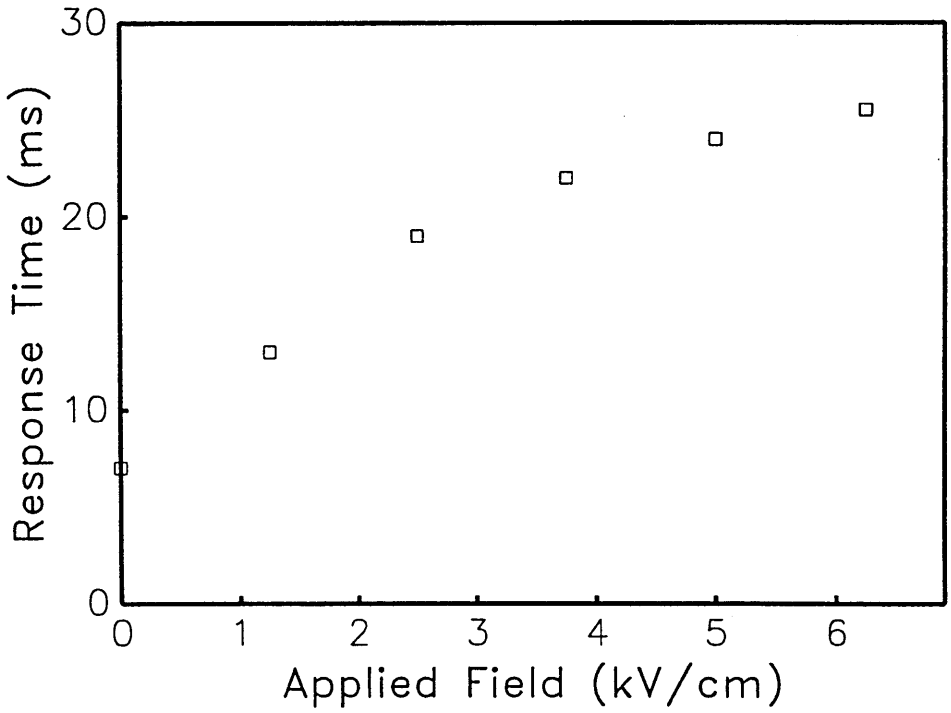

Figure 3.12 Grating decay time as a function of applied voltage. Λ = 1 μm, $I_1 = I_2$.

Chapter Four
Image Processing Considerations

This chapter presents and discusses some of the aspects of photorefractive BSO that have a significant influence on its applicability as an optical information processing medium. Thus, the results in general are presented from a practical point of view, with the emphasis placed on utilisation of the material in practical systems.

4.1 Optical Absorption

It is clear that the photorefractive properties of a material depend heavily on the crystallographic impurities, whether intentionally introduced or otherwise. Therefore a particular task may dictate the use of a group of materials based purely on the absorption at a specific wavelength of light. For instance, the photorefractive semiconductors such as GaAs are becoming much more attractive as semiconductor lasers become more refined and less expensive.

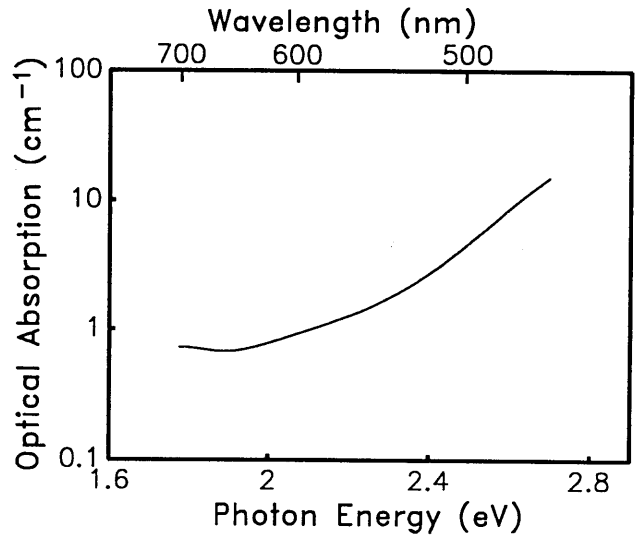

Figure 4.1 Optical Absorption Spectrum for BSO.

The absorption spectrum of the BSO crystal was investigated using a Perkin Elmer Computerised Scanning Spectrophotometer (model Lambda 2). The results are shown in Figure 4.1 for the region of the visible spectrum which could be accurately measured. The data for the far-blue

and far-red ends of the spectrum were erroneous due to the absorption being either too great or too small to measure, at least without resorting to a more sophisticated measurement technique (such as the use of a thinner crystal sample). The data have been corrected for Fresnel reflections at the crystal surfaces, using the refractive index data given in reference 4.1. The heavy absorption which is centred at about 480 nm has been attributed by some authors [4.2] as being due to a silicon vacancy in the crystal lattice. However, in what seems to be regarded as the definitive work, Oberschmid [4.3] determines from a combined study of BSO and BGO crystals that the most probable source of absorption centres is the incorrect occupation of a silicon site by a bismuth atom. This would provide an energy scheme which predicts the absorption from about 2.3 - 3.2 eV. The band gap of BSO is 3.2 eV, from which point there is strong absorption.

In terms of image processing using BSO, the most important property of Figure 4.1 is the fact that the absorption at red wavelengths is about an order of magnitude less than that at the blue wavelengths. Also, the quantum efficiency is lower [4.4] and so the probability of an incoming photon of energy 2.0 eV (~ 630 nm) producing a photoelectron is approximately two orders of magnitude less than that of energy 2.4 eV (~ 510 nm). This allows gratings to be written using the output of a laser such as an Argon ion or a frequency-doubled YAG whilst the readout can be non-destructive by using a HeNe laser at 633 nm. This is a common technique in image processing applications and will be used in chapter 6.

4.2 Optical Activity

BSO belongs to the crystallographic class 23. This means that its basic lattice shape is body-centred cubic. As the space group 23 does not contain a centre of symmetry or any mirror planes there is the possibility of there being a non-reciprocated progression of atoms through the crystal forming a 'screw' axis. Such a physical feature permits the phenomenon of 'optical activity' to occur. Optical activity is the rotation of the plane of polarisation of light as it propagates through the material. Although the screw axis must be present for optical activity to occur, it must not be thought that the

polarisation directly follows such a molecular pattern; otherwise the effect would be far greater than is observed and there could be no spectral dispersion.

BSO and its isomorphs ($Bi_{12}GeO_{20}$ and $Bi_{12}TiO_{20}$) have, for some time, been known to be optically active [4.5]. The optical activity of the BSO crystal was measured at the wavelengths of prime concern to this thesis; 514.5 and 632.8 nm. The results were as follows;

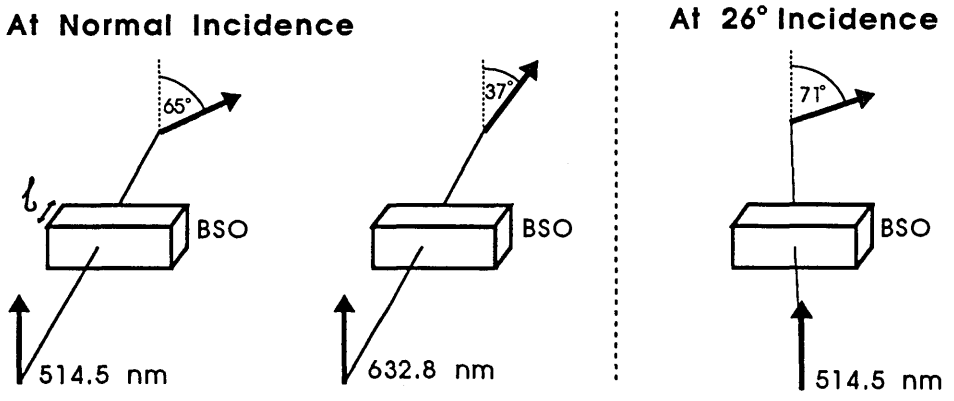

Figure 4.2 Rotation of polarisations for light at 514.5 and 632.8 nm.

The purpose of the measurement of the rotation at an incidence angle of 26° was to ascertain that the rotation at normal incidence was in fact 65° and not $n\pi + 65°$. All rotations shown above were clockwise in the direction of propagation of the laser beam, and so by convention [4.6], this crystal is classed as 'negative' optically active.

Although it has been shown that optical activity lowers the amplitude of PR response in BSO [4.7], it may also be considered an advantage in that it can significantly improve the signal-to-noise ratio at the output of an optical processor. This is due to the fact that the diffracted and transmitted components of a beam reading a grating may have significantly different polarisation states. This effect is presented in section 4.4.3

4.3 Crystallographic orientation

It was stated in section 2.4 that BSO is most commonly used in either of two crystallographic orientations, depending on the particular application. One orientation allows maximum energy transfer between the two 'write' beams (two-wave mixing orientation) whilst the other is for maximum diffraction efficiency (or phase conjugate reflectivity) of a third 'read' beam (four-wave mixing orientation).

4.3.1 Determination of Orientation

A technique was developed in reference 3.4 to distinguish between these two orientations. The distinguishing feature is that when the crystal is in the two-wave mixing orientation there will be energy transfer in one direction only, irrespective of the polarisation of the beams forming the grating; whereas when the crystal is in the four-wave mixing orientation there is energy transfer in either direction, depending on the writing beams' polarisation orientation. This technique was used to determine the crystallographic orientations of an unknown sample of BSO, in order that electrodes could be deposited in the orientation for maximum diffraction efficiency.

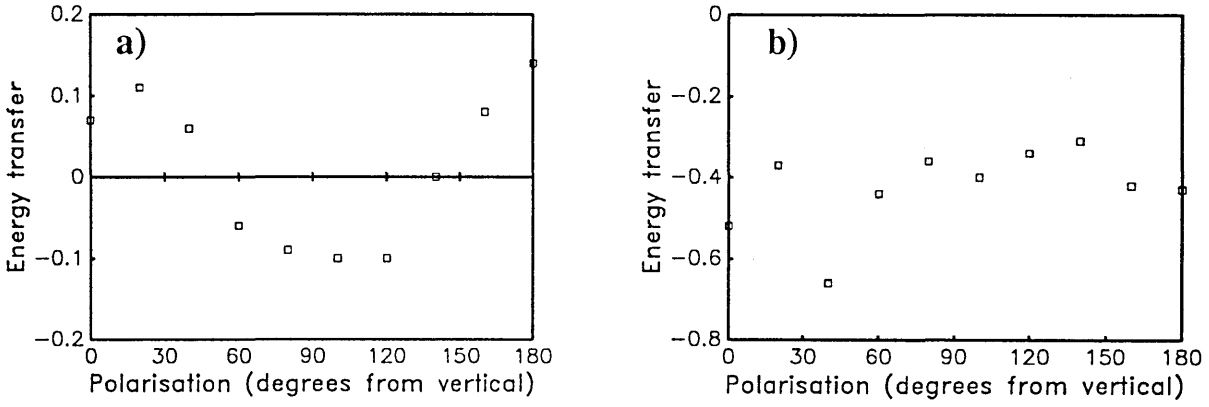

Figure 4.3 Graphs showing the variation of energy transfer with input polarisation for the two common orientations of BSO. Energy transfer is defined in the next section. Note that the polarisation angle refers to both write-beams, as parallel polarisation is maintained throughout the readings. a) Four-wave mixing orientation and, b) two-wave mixing orientation.

Figure 4.3 demonstrates the effect that the input polarisation angle has on the energy transfer from one beam to the other. The four-wave mixing orientation is easily identified as that in which the energy transfer direction alternates.

4.3.2 Comparison of Orientations

A quantitative measure of the amount of energy transferred between I_1 and I_2 is given by Γ, such that;

$$\Gamma = \frac{1}{\ell} \ln \left(\frac{I_1(\ell).I_2(0)}{I_1(0).I_2(\ell)} \right) \tag{4.1}$$

Thus, Γ can be calculated for each of the two orientations, and subsequently collated with the previously measured values of η. As was stated previously, it is expected that Γ and η will vary by a factor of four between the two orientations and that one orientation will show maximum η whilst the other shows maximum Γ. The following experimental results can now be compared;

Orientation	001 to top	110 to top
Γ (a.u.)	10	46
η (a.u.)	5.5	1.6

The expected behaviour is seen to be observed, with approximately the correct ratio between orientations.

For all of the applications presented in this thesis, maximum diffraction efficiency was desired. Therefore, in the following chapters, the crystal was always used in the four-wave mixing orientation.

4.4 Polarisation effects

The interaction of polarised light with a crystalline photorefractive medium is intrinsically vectorial, with the crystal orientation relative to the grating vector, applied field and beam polarisations being critical. A detailed study of the vector nature of the effect is beyond the scope of this thesis (see for example,

reference 3.5). Of interest here are the advantages that polarisation properties offer to optical applications. The studies reported here were all performed with linearly polarised light.

4.4.1 Polarisation of Write beams

The Ar^+ laser write-beams must possess parallel polarisations in order that maximum modulation can be attained. The variation of diffraction efficiency with the angle between the write-beams' polarisation follows the usual $\cos^2\theta$ dependency. It is of more interest to examine how the diffracted intensity varies as a function of the polarisation angle of both the writing beams; i.e., the write beams possess parallel polarisation which is rotated from the vertical. The resulting diffraction efficiency is shown in Fig. 4.4. It can be seen that there is no significant change in the diffracted beam intensity. Thus, it is concluded that as long as the two writing beams have parallel polarisation states, the angle that this polarisation vector makes to the crystallographic axes is irrelevant. This effect was verified for both crystallographic orientations.

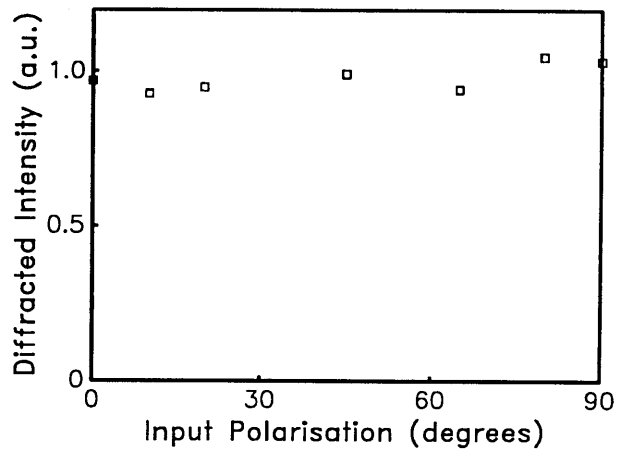

Figure 4.4 Variation of diffraction efficiency with write-beams polarisation.

4.4.2 Polarisation of the Read Beam

The behaviour of the intensity of the diffracted beam was examined, as the read-beam polarisation was varied. The results are shown below for both crystallographic orientations.

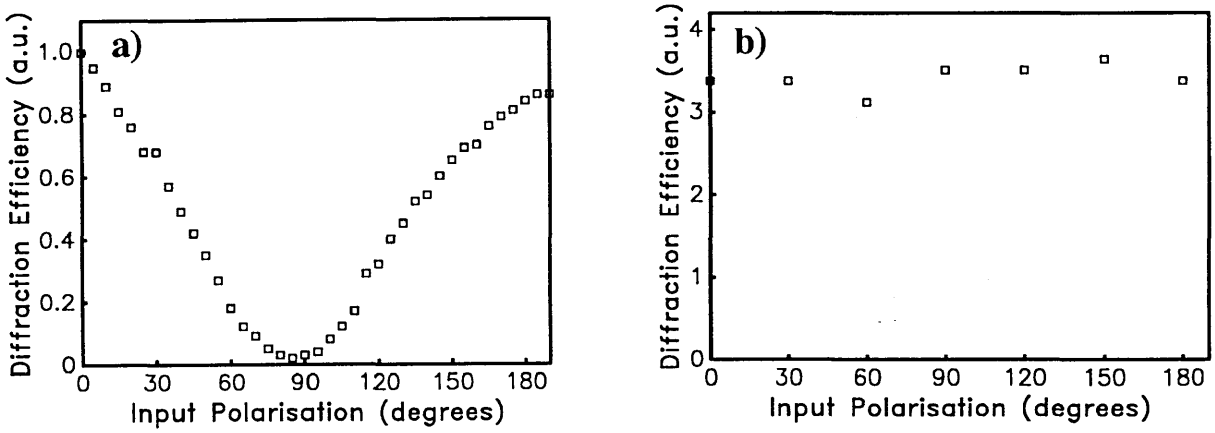

Figure 4.5 Variation of diffraction efficiency with read-beam polarisation a) 2-wave mixing orientation b) 4-wave mixing orientation

From Figure 4.5 it can be seen that different results are obtained for each orientation. In the four-wave mixing orientation case there is no significant variation in the diffracted output intensity as the angle of read-beam polarisation is varied, whereas in the two-wave mixing orientation the intensity exhibits a sinusoidal variation. An explanation for these results is suggested by examination of the birefringent axes induced in each of the orientations, as shown in the diagram on the next page.

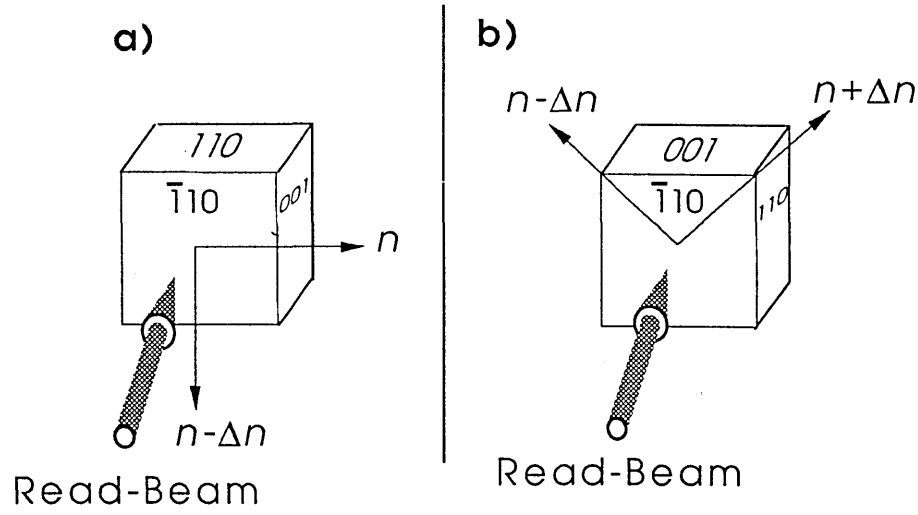

Figure 4.6 Birefringent axes for the two crystallographic orientations.

From Figure 4.6, it seems plausible that when the crystal is in the orientation for two-wave mixing, only a read-beam with vertical polarisation can detect the vertical birefringent axis, whereas in the four-wave mixing orientation, any angle of read-beam polarisation can sample the birefringent axis that is the resultant of the two orthogonal components.

4.4.3 Polarisation States of Emergent Beams

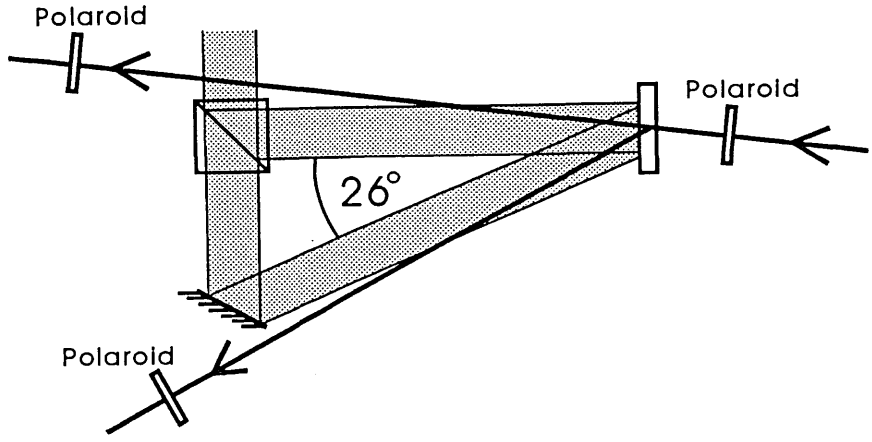

Figure 4.7 Experimental system used to study polarisation states of beams involved in the diffraction process.

Having seen how the diffracted intensity varies with the read-beam polarisation, it is now of interest to consider how the polarisation of the emergent transmitted and diffracted beams is affected. The system shown in Figure 4.7 was used to conduct this study, in order that the polarisation of each of the beams involved could be measured without the need to position beam splitting or mirrored components in the path of the read-beam.

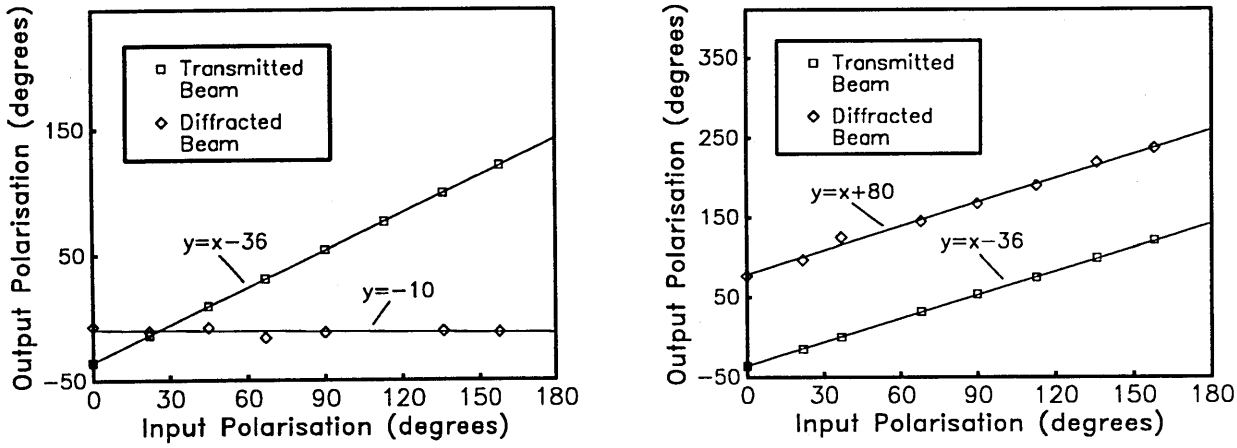

Figure 4.8 Output polarisation states of transmitted and diffracted beams a) 2-wave mixing orientation b) 4-wave mixing orientation

It is interesting to note from Figure 4.8 that the transmitted beam, in either case, is rotated according to the optical activity of the sample (in each case the straight line fitted is given by: transmitted poln. = incident poln. - 36±1°). The behaviour of the diffracted beam, however, depends on the crystallographic orientation. In the four-wave mixing orientation the diffracted beam polarisation is a constant angle from the transmitted component, and is thus also a constant angle from the incident beam. In the two-wave mixing orientation the diffracted beam emerges with the same polarisation angle (approximately vertical) no matter what the incident polarisation is. Again these results are suggested by examination of Figure 4.6. If the only component of the read-beam that can be diffracted, in the two-wave mixing orientation, is vertical, then we may expect that the emergent beam is formed by the coherent summation of solely vertical components,

and as such must also be approximately vertical (depending on the exact orientation of the holographic fringes/birefringent axis). In the four-wave mixing orientation, however, any orientation of read-beam polarisation can read the grating and so the output beam is derived from the summation of all components. There is no reason to expect therefore that the diffracted beam should emerge from the crystal with anything other than a fixed relationship with the incident beam.

It is evident that both of the crystallographic orientations offer ample opportunity to enhance the signal-to-noise ratio in optical processors, through the use of polaroid sheet at the output stage to filter out the background transmitted light. Although orthogonal diffracted and transmitted components cannot be obtained in the four-wave mixing orientation (for this particular sample thickness) it is the preferred orientation due to its higher diffraction efficiency and insensitivity to beam polarisations.

It should be noted that all of the above measurements were made without the added complication of an applied electric field. It has been shown that an external voltage applied to BSO not only causes an induced linear birefringence (due to the electro-optic effect), but can also cause a change in optical activity (a change in the circular birefringence). This effect has been termed 'photoactivity' [4.8]. However, this does not negate the preceding results, as although photoactivity causes the emergent beams to be elliptically polarised, their major axes will still be sufficiently different to allow the noise suppression techniques to be implemented.

4.5 The effect of an Applied Field on the Spatial Frequency Bandwidth of BSO

It was observed in Figure 3.6 that the diffraction efficiency of BSO, when an external electric field is applied, is dependent on the grating spacing. This obviously poses considerations in terms of optical information processing when input scenes will possess a wide range of spatial-frequency content. Complete experimental curves have been presented elsewhere [references 2.12 and 3.5] of the variation of diffraction efficiency with applied field and fringe spacing. Instead,

a simulation of the dependence, as predicted by equation 2.21, is shown below in Figure 4.9. These curves were generated using the value of E_Q obtained from the non-linear curve-fitting algorithms used in chapter 3. It was shown in the above two references that equation 2.21 adequately predicted the experimental data.

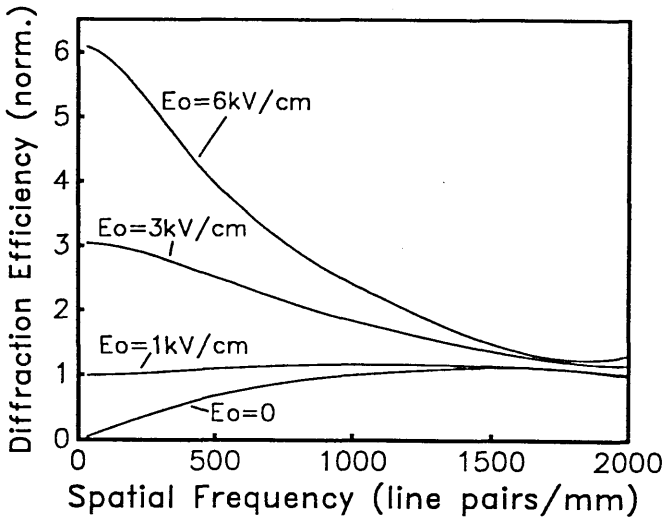

Figure 4.9 Variation of diffraction efficiency with spatial frequency. The curves were generated using the value of E_Q obtained in the curve-fitting of chapter 3.

Figure 4.9 shows the variation of diffraction efficiency with spatial frequency (the reciprocal of fringe spacing), for various applied fields. It is observed that only for fields of about 1 $kVcm^{-1}$ is there a flat response across a wide range of spatial frequencies. At other applied voltages there is a non-linear frequency response. Specifically, although the application of a high electric field significantly improves the diffraction efficiency at lower spatial frequencies, the flat response desired for an information processing material is sacrificed.

4.6 Tolerance of Bragg matching to the Volume Hologram

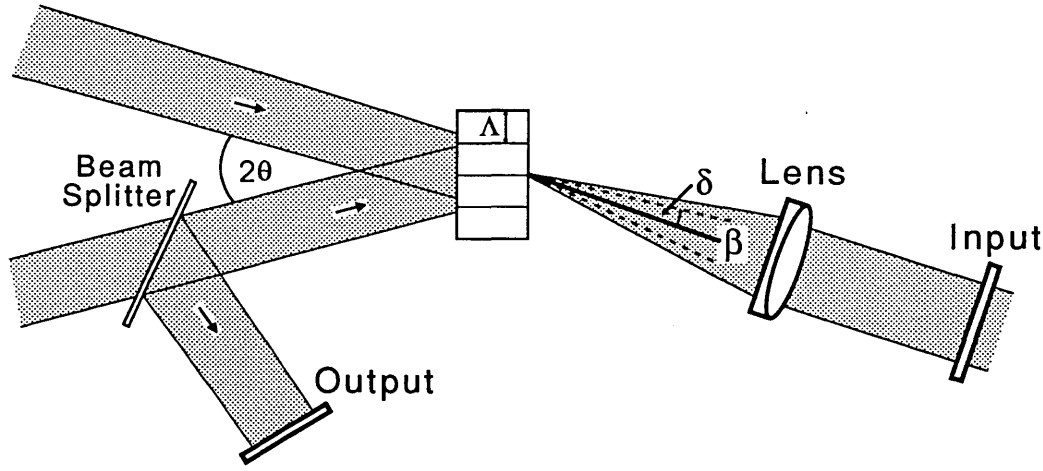

Figure 4.10 A typical optical configuration using a photorefractive crystal.

In the preceding section it was observed that the spatial frequency response of a PR crystal, as a component of an optical system, may not be linear. It is therefore convenient to examine also how geometric factors affect the spatial-frequency bandwidth. A typical imaging system is shown in Figure 4.10. The lenses used in such a set-up are assumed to possess a sufficiently large aperture to allow us to neglect their influence. It can be seen from Fig. 4.10 that a major influence on the optical performance of the system is the magnitude of deviation, δ, from the Bragg angle within which a diffracted beam can still be obtained. From chapter 3, the expression for diffraction efficiency was given by;

$$\eta = \left| -i\frac{\exp(-i\xi)\sin(\xi^2 + \nu^2)^{1/2}}{(1 + \xi^2/\nu^2)^{1/2}} \right|^2 \qquad (4.2)$$

As ξ is a measure of δ, it is convenient to plot a graph of normalised diffraction efficiency as a function of ξ. Such a graph is shown in Figure 4.11 below. The values for ν of $\pi/24$ and $\pi/4$ were chosen to represent typical values for BSO. In BSO with $\Lambda = 1$ μm and $E_o = 0$, $\Delta n \simeq 1 \times 10^{-5} \rightarrow \nu \simeq \pi/24$, and for $\Lambda = 20$ μm and $E_o = 6.3$ kVcm^{-1}, $\Delta n \simeq 6 \times 10^{-5} \rightarrow \nu \simeq \pi/4$. Therefore, for the experiments presented in this thesis; $\pi/24 < \nu < \pi/4$.

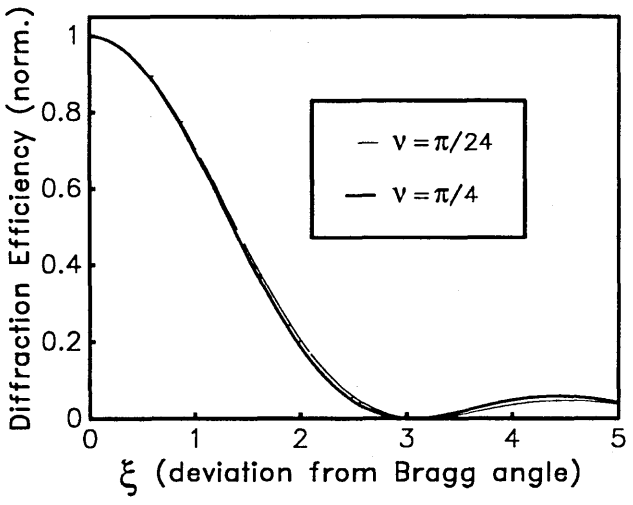

Figure 4.11 Plot of normalised diffraction efficiency against $\xi = \delta(2\pi/\lambda_r)\ell\sin\beta$, for two values of the parameter $\nu = \pi\Delta n\ell/\lambda_r\cos\beta$.

It is seen from Figure 4.11 that $\eta \to 0$ at $\xi \simeq 3$, within the experimental range of ν. Therefore, to compute a value for δ for which the diffraction efficiency is zero, we should set $\xi = 3$ in equation 3.2, yielding;

$$\delta = \frac{3\lambda_r}{2\pi\ell\sin\beta} \simeq \frac{\lambda_w}{\lambda_r}\frac{\lambda_r}{2\ell\sin\theta} \tag{4.3}$$

or, from the definition of Λ (section 2.2);

$$\delta \simeq \frac{\Lambda}{\ell} \tag{4.4}$$

In other words, the angular acceptance around the Bragg angle is dependent on the ratio of fringe spacing to the thickness of the crystal. For any particular sample, the thickness is fixed, leaving only the fringe spacing as a means for maximising the acceptance angle. In practice, this generally entails increasing Λ as much as possible, while still producing diffracted and transmitted beams which are spatially separated within the confines of the optical system (i.e. if Λ was increased the zero and first order diffracted beams would overlap).

Figure 4.12 demonstrates the effect that varying the fringe spacing has on an image that is diffracted through a system such as that depicted in Figure 4.10. It should be noted from this diagram that, not only is the spatial frequency bandwidth of the system dependent on

Λ, but also the spatial extent of the information passed. The relative roles of each of these effects is determined by the distance between the lens and the crystal, i.e. whether there is any decomposition of the optical information into its spatial frequency components.

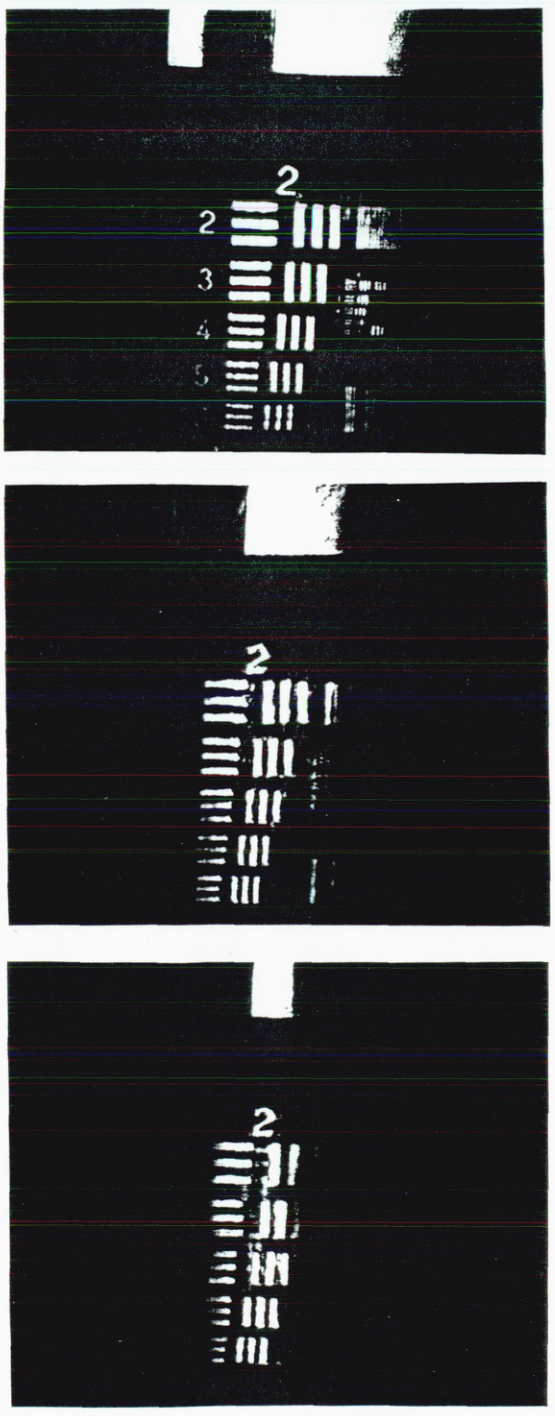

Figure 4.12 Demonstration of variation of field-of-view restriction at various average spatial frequencies. From top to bottom, a) 4.0 μm b) 2.5 μm and c) 1.1 μm.

4.7 Spatial Filtering by Local Variations in the Modulation Index

It was observed in chapter 3 that the diffraction efficiency is dependent on the modulation index, as determined by I_1 and I_2. This effect can be exploited to produce spatial filtering in the Fourier transform (F.T.) plane [4.9]. This opportunity for spatial filtering arises because of the wide dynamic range of spatial frequency information at the F.T. plane. Therefore, if a reference beam of (approximately) uniform intensity is used to form a hologram with an image beam, then the modulation, and thus diffraction efficiency, will vary according to the local intensity of the F.T. pattern. In other words, the system can be adjusted so that the optical information corresponding to the higher spatial frequencies of an input scene is accentuated; i.e. edge-enhancement is achieved. Figure 4.13 shows an example of such edge enhancement.

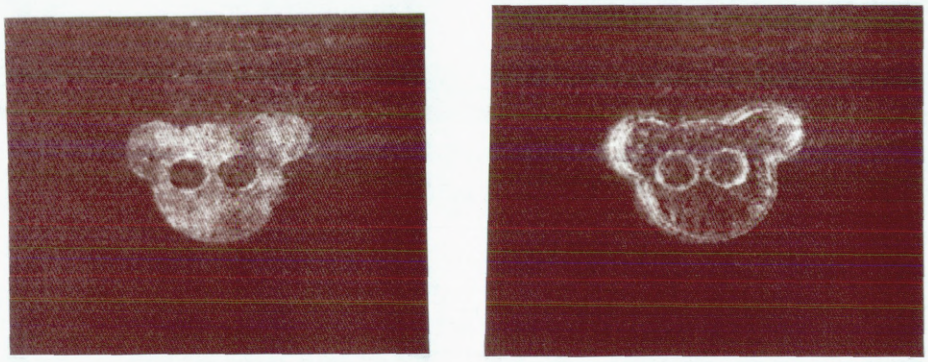

Figure 4.13 Example of edge enhancement obtained by varying the beam ratio such that non-linear recording of the hologram is obtained to accentuate the higher spatial frequencies of the input object.

4.8 Interaction of Object Functions

The final section in this chapter examines how the superposition of spatial information onto two coherent beams affects the resulting hologram formed by their interference.

Suppose that the two coherent beams forming a grating have objects inserted into them, with arbitrary transmission functions f(x,y) and g(x,y). These beams will generally pass through an optical system (such as a series of lenses) to produce a linear transform (such as the

Fourier transform) of the functions f(x,y) and g(x,y), at the BSO crystal. Suppose then that the transformed light at the crystal plane (p,q) is given by F(p,q) and G(p,q). As these two beams are coherent (it is also assumed that they are of parallel polarisation) they will interfere to produce an intensity distribution of the form;

$$I(p,q) = | F(p,q) + G(p,q) |^2 \qquad (4.5)$$

It was demonstrated in chapter 2 that, in accordance with the Kukhtarev model of the photorefractive effect, this intensity pattern will inhomogeneously generate photoelectrons within the volume of the crystal. These charge-carriers move by drift and diffusion into the dark regions where they are subsequently re-trapped. In the 'drift-mode' of grating formation, applicable to the fringe spacings used in the optical processing tasks considered in this thesis, this charge migration will form a space-charge field which is approximately proportional to the applied electric field and the inhomogeneous illumination (from consideration of equation 3.7 it is clear that at $\Lambda \approx 20\ \mu m$, $|E_{sc}| \sim mE_o$). Considering only the term of (4.5) that is associated with the correlation output of this system, the fundamental component of the space-charge field, E_{sc}, is then;

$$E_{sc}(p,q) \propto F(p,q)G^*(p,q) \qquad (4.6)$$

Via the linear electro-optic effect this optically induced local electric field modulates the refractive index. The change in refractive index for this orientation of BSO is given by;

$$\Delta n(p,q) = -\frac{1}{2} n^3 r_{41} E_{sc}(p,q)$$

where n and r_{41} are as previously stated. Thus a readout HeNe beam would encounter a phase modulation given by;

$$\phi(p,q) = \frac{2\pi}{\lambda_r} \ell \Delta n(p,q) \qquad (4.8)$$

The transmission function of the crystal is then;

$$t(p,q) = \exp\{ i \phi(p,q) \} \qquad (4.9)$$

or for the case of BSO where the induced phase modulation is small;

$$t(p,q) \simeq 1 + i \gamma F(p,q)G^*(p,q) \qquad (4.10)$$

where $\gamma = \ell \frac{2\pi}{\lambda_r} n^3 r_{41}$. Thus if a readout beam, of arbitrary distribution R(p,q), is incident on the crystal such that it satisfies

the Bragg-matching criterion for the term shown in equation (4.10), the light distribution just beyond the crystal will be proportional to;

$$R(p,q).F(p,q).G^{*}(p,q) \qquad (4.11)$$

In other words, the diffracted component of the readout beam conveys information about the original distributions f and g, such that multiplication of the two-dimensional information is achieved at the crystal plane. This readout beam itself may contain spatial information (see section 6.2), or it may be a plane wave (section 6.1). The light distribution at the crystal plane is generally passed through another lens to form either the F.T. of equation (4.11), or the image of it.

Chapter Five
The Effect of Optical Bias on the Transient Characteristics of BSO

5.1 Introduction

In chapter 2 it was observed that damped oscillatory behaviour can be expected on formation of the space-charge field which is produced by the interference of two plane waves. In other words, a transient peak will be evident in the field which, via the linear electro-optic effect, is also manifested in the diffraction efficiency of the resulting refractive index grating. Therefore, transient enhancement will be experienced in beams which are subsequently diffracted from such a grating.

In this chapter results are presented to demonstrate that this transient peak can be controlled by a suitable choice of external conditions. As before, gratings are written using an Ar^+ laser operating at 514 nm and a HeNe laser at 633 nm performs the readout. It will be demonstrated that a necessary and regulating condition for this transient enhancement is uniform illumination in excess of the cosinusoidal interference pattern; i.e. optical bias. The experimental conditions for optimising this effect will be presented, and detailed measurements noted in an attempt to comprehend its physical basis. Analysis of the phenomenon will be attempted, and its relevance to device considerations assessed.

It should be borne in mind that an incoherent diffracted beam can be sensitive only to the magnitude of the space-charge field and not to any (time-dependent) phase shift between the recording pattern and resulting grating. Thus, these results should be viewed as supplementary to those previously reported on transient energy transfer (TET) using the sillenite crystals [2.13]. It is anticipated, therefore, that these results will offer further insight into the fundamental nature of grating formation in BSO and its isomorphs.

5.2 Experimental Configuration

The experiments were carried out on the sample of BSO obtained from Sumitomo Industries. This effect has also been observed in other BSO crystals.

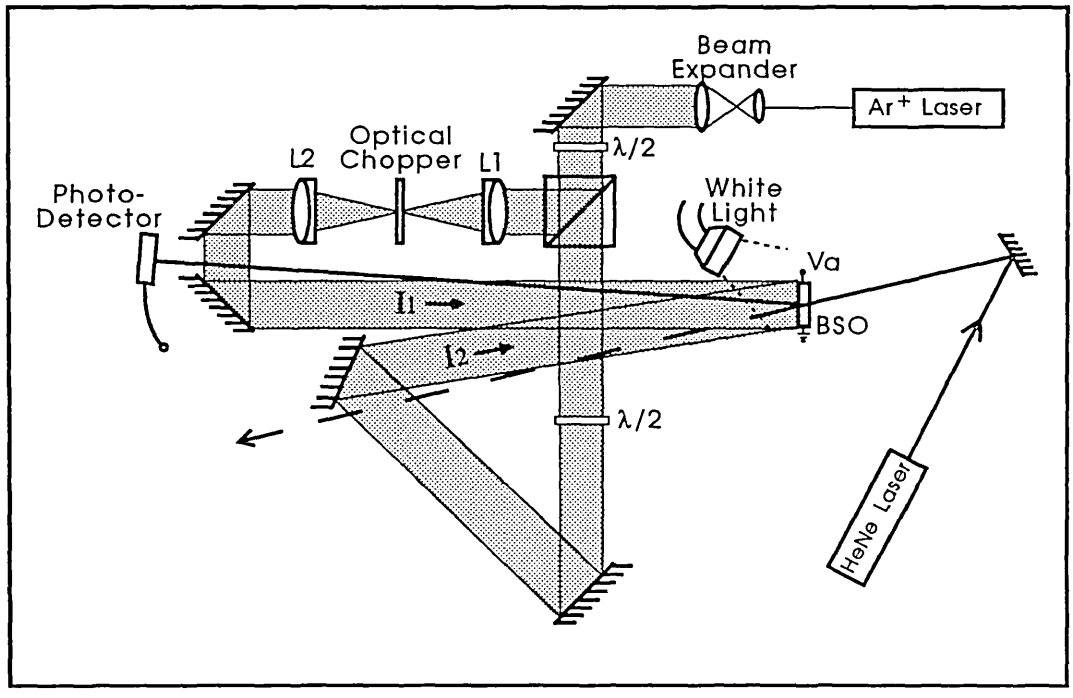

Figure 5.1 Experimental arrangement used to study the effect of optical bias on the grating formation characteristics.

The experimental arrangement used to carry out this study is shown in Figure 5.1. A single-longitudinal-mode Ar^+ laser beam is split into two beams, I_1 and I_2, of equal intensity, which then recombine within the volume of the crystal at an angle which can be varied to provide fringe spacings, Λ, from 1 to 25 μm. One of the beams is chopped at the mutual focal plane of a two lens system, L1 and L2, both of focal length 45 cm. Thus the switching of this beam occurs on a sub-millisecond time scale, but can also be varied by axial movement of the optical chopper. The extra uniform illumination is provided initially by a Schott white light source with fibre optic light-guide. This allows variation of the uniform (white light) intensity I_3 with respect to the intensity of the coherent writing beams. A low-power

(< 1mW) HeNe beam is diffracted from the refractive index grating formed and the diffracted beam intensity is measured using a photodetector and power meter. The analogue output of this meter is fed to an A/D input card on a PC so that averaging and analysis of signals can be directly carried out.

The grating vector is arranged to be parallel to the [110] direction to maximise diffraction efficiency and to alleviate the complication of a time-varying modulation index due to energy transfer. A voltage of up to 5kV is applied, also in the [110] direction, to enhance the amplitude of response and facilitate the formation of gratings at the larger fringe spacings.

5.3 Results and Discussion

5.3.1 Effect of White-Light Illumination

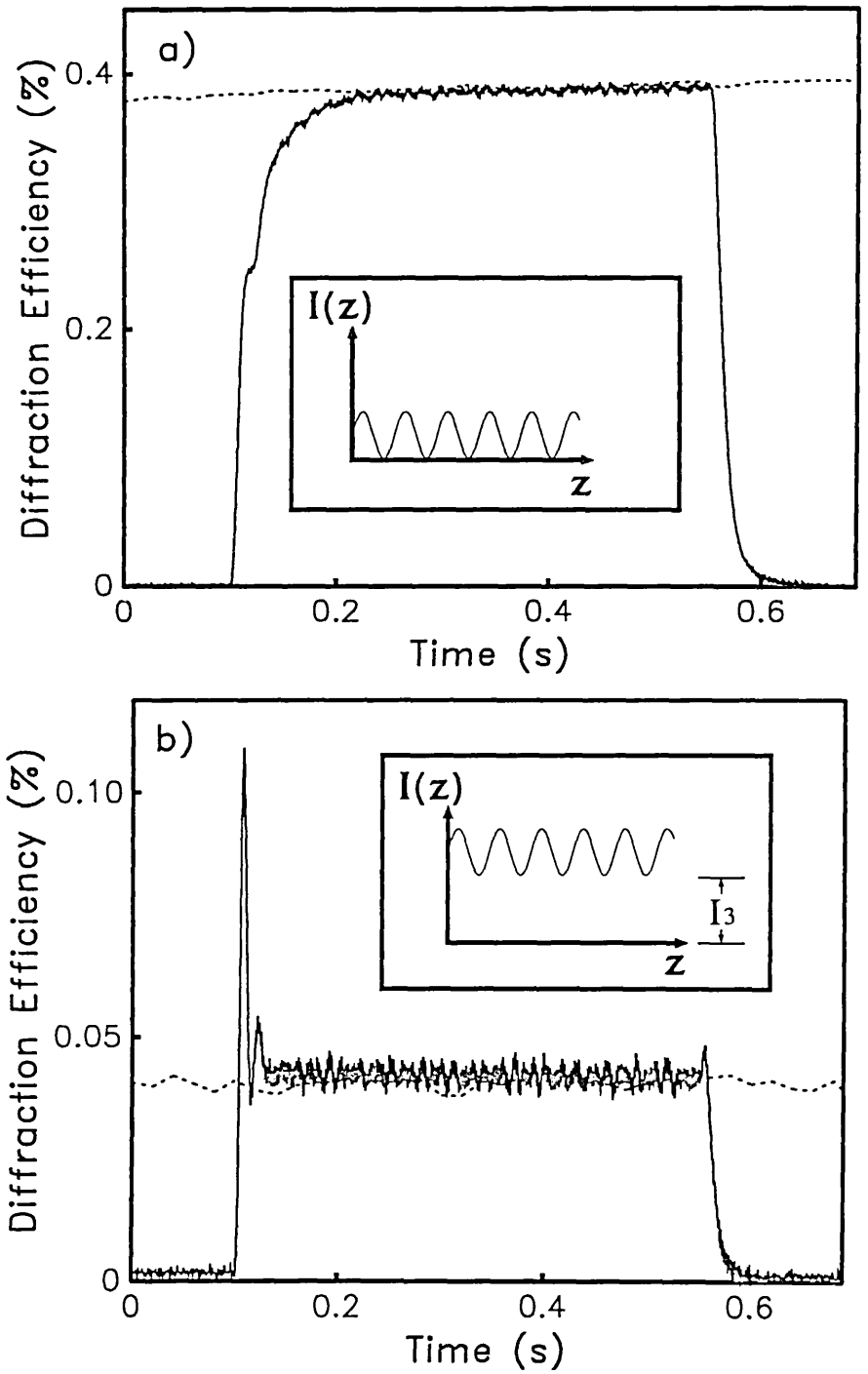

Figure 5.2 Diagram showing the effect of optical bias on the transient diffraction efficiency. From top to bottom; a) coherent write-beams present only, and b) optical bias (white light) introduced. The dashed line shows the steady-state diffracted output, and the solid line shows the case with beam I_1 chopped.

The intensity of the white light illumination was varied by the use of neutral density filters. The two extreme cases are shown in Fig. 5.2; a) is the trace obtained with only the two coherent writing beams present and b) is for the case when white light is introduced. The white light has two effects: the additional intensity has the usual effect of reducing the modulation index, m, and so the steady state diffraction efficiency, η, is reduced according to the approximate dependency of η with m^2 [2.4]. The second and more interesting effect to observe is that as this reduction in the steady state value of diffraction efficiency takes place, it is accompanied by an increase in the transient peak relative to that steady state value. That is, in a) the diffraction efficiency rises monotonically to its steady state value, whereas in b) the diffraction efficiency reaches a transient peak before falling back down to its steady state value, i.e. transient enhancement is achieved.

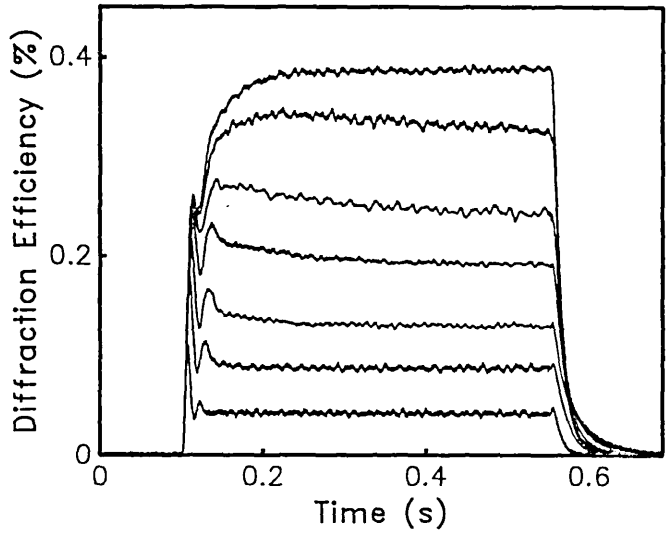

Figure 5.3 Plot showing the progression between the two extreme case cases that were shown in figure 5.2.

The progression between the two states shown in Figure 5.2 is given in Figure 5.3. Note that, in each case, the grating formation follows the same rise curve before being damped down to the steady-state value of η, as determined by the modulation index calculated from I_1, I_2 and I_3. The ratio of peak-to-steady-state intensity is seen to increase as

the white light intensity is increased. If this ratio is plotted as a function of the white light intensity (Figure 5.4, below) it is seen that there appears to be a simple relationship. This will be examined further in due course.

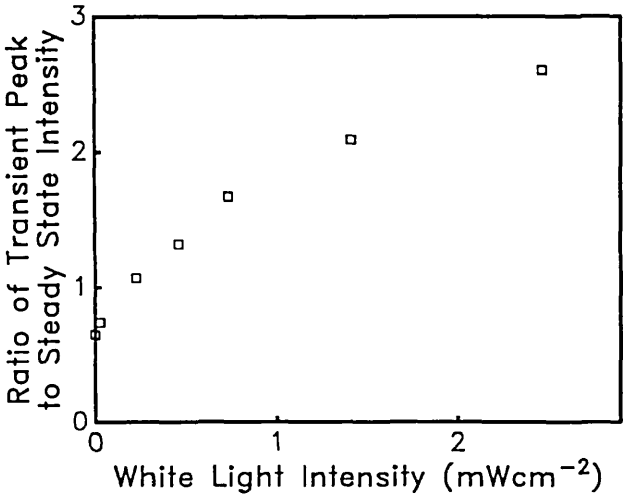

Figure 5.4 Plot of the transient-peak to steady-state intensity ratio as a function of the white light intensity. The white light intensity was measured via the use of a glass slide to 'pick off' a component of the intensity, prior to the crystal.

5.3.2 Spectral Dependence

Up to this point the light that was used to provide the optical bias has simply been a (polychromatic) white light source. It is of interest now to examine the behaviour of this phenomenon as a function of wavelength.

To select a specific wavelength from the white light intensity a set of narrow bandpass (~ 10 nm) interference filters was used. This produced a range of fairly monochromatic sources throughout the visible spectrum. Constant intensity at the crystal was maintained following careful calibration of the system comprising a glass beam splitter (~ 5 % reflectance) positioned just in front of the crystal, and a Newport photodetector with calibrated power meter.

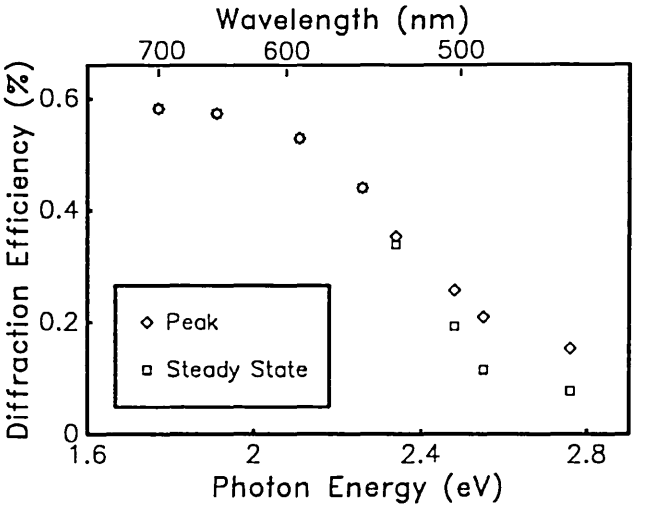

Figure 5.5 Variation of transient and steady-state diffraction efficiency with the wavelength of the optical bias.

The steady-state and transient diffraction efficiency are plotted, as a function of photon energy, in Figure 5.5. Note that the transient peak does not begin to overshoot the steady-state diffraction efficiency until about 2.3-2.4 eV, from which point the steady-state diffraction efficiency is reduced as before, and the transient peak becomes more prominent. This suggests that what is in fact causing the transient enhancement is the production of (spatially uniform) photocurrent within the crystal, howsoever generated.

Therefore, in order that an accurate and useful measurement of the white light intensity at the crystal can be obtained, it is assumed that, ultimately, all that is of consequence in the formation of the grating is the production of photoelectrons. A relative measure of the conduction-band electron density is given by the photocurrent through the crystal. Thus the crystal itself can be used effectively as an optical power meter if the photocurrent passed by the (electrically) biased crystal is measured. The white light intensity can now be scaled in units of the sum of the photocurrent induced by the two write-beams. This technique avoids any problems inherent in the measurement system used to determine the intensity of white light.

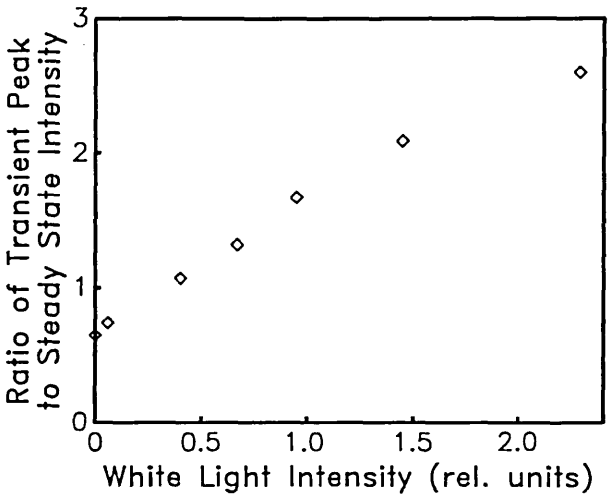

Figure 5.6 Transient-peak to steady-state ratio as a function of the photocurrent induced by the white light.

Figure 5.4 can now be re-plotted using the photocurrent as a measurement of the 'useful' white light intensity. From Figure 5.6 it is seen that a linear relationship between the transient-to-steady-state ratio and the optical bias level is now apparent.

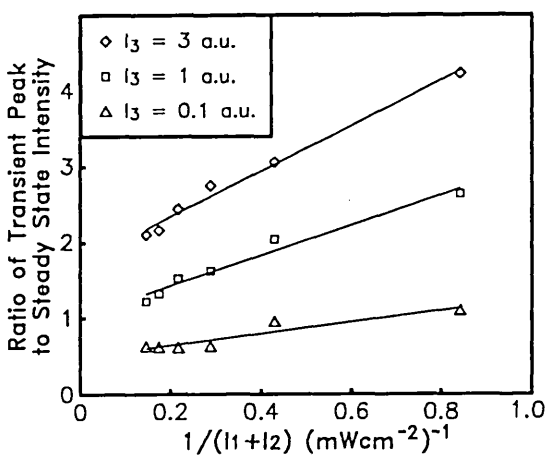

Figure 5.7 Transient-to-steady-state ratio as a function of various white-light to write-beam intensity ratios.

For the next experiment the white light intensity was fixed at three levels and, at each, the combined Ar^+ write beam intensity was

varied. From Figure 5.7 the ratio of peak to steady state intensity is seen to be approximately linearly dependent on the ratio of white light to write-beam intensity over this range and ratios up to a factor of four are achieved with this crystal before the diffracted intensity becomes immeasurable. It is now clear that the ratio of transient-to-steady-state diffraction efficiency is determined by the ratio of optical bias to write-beam intensity.

5.3.3 Effect of the Source of Optical Bias.

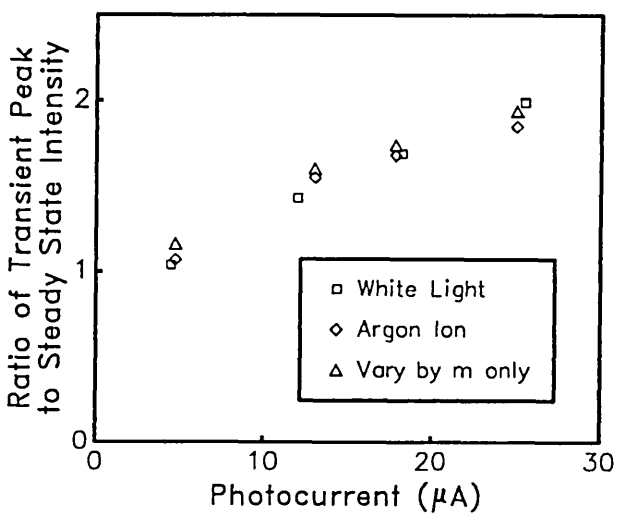

Figure 5.8 Variation of the ratio of transient-peak to steady-state diffraction efficiency for different sources of optical bias.

By using the photocurrent as a measure of the optical bias it is possible to compare the effect of using different light sources for the optical bias. Readings were thus taken of the variation of the transient-to-steady-state ratio at four settings of white light intensity. Then the corresponding optical bias was obtained using a third beam derived from the same Ar^+ laser as the two write-beams. Finally, the same conditions were established by varying the ratio of the two write-beams alone. It is seen from Figure 5.8 that no significant variation is observed between the different sources of optical bias. Thus, it is concluded that the optical bias has only to be present to generate a uniform photocurrent; the actual characteristics of the illumination are irrelevant.

5.3.4 Variation with Overall Intensity

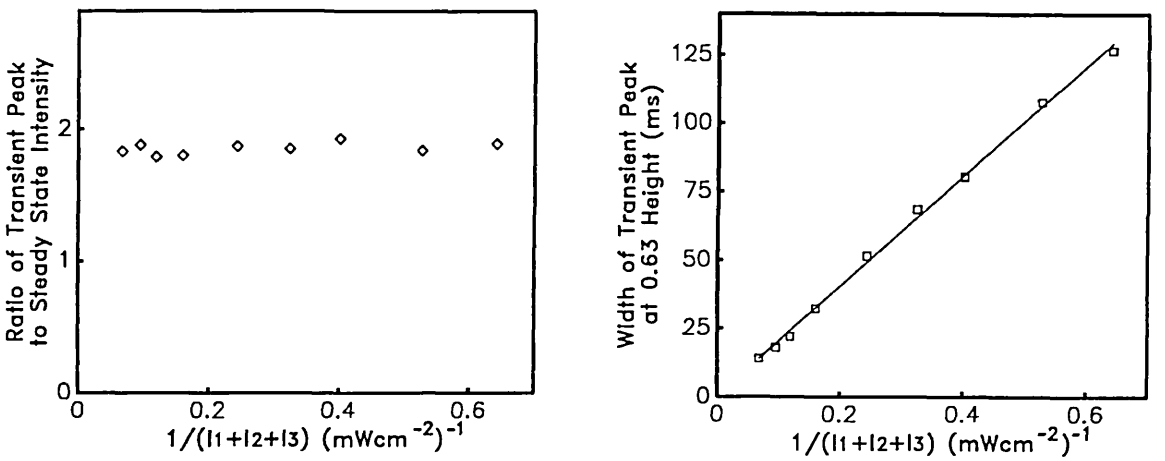

Figure 5.9 Variation of a) transient-to-steady-state ratio, and b) width of transient peak, as a function of the combined (I_1 + I_2 + I_3) intensity.

It is evident from chapter 3.3 that the formation of a photorefractive grating is driven by the photogeneration of charge carriers. The transient response is therefore characterised by the Maxwell relaxation time. It is expected then, that the 'width' of the transient peak (defined here as the width at 63% height) can be controlled by adjustment of the intensity of the beams involved. To demonstrate this effect it was chosen to use for the optical bias an Ar^+ laser beam that was derived from the same laser as the two writing beams. This allowed the overall power of the beams to be increased collectively while maintaining the same ratios between them. It can be seen from Figure 5.9 a) that as the intensity is increased the ratio of peak to steady state is unchanged, but from Figure 5.9 b) that the width of the peak is inversely dependent on the overall intensity. This demonstrates that the peak-to-steady-state ratio is determined only by the ratio of optical bias to coherent intensity whereas the width of the peak is determined by the overall intensity. Peak widths of around 20 ms are easily obtained with only 2 mW of coherent optical power required at the crystal; i.e. devices based on this effect could produce recovery of the optical processor at T.V. frame rates at low values of coherent intensity.

Finally in this section, the behaviour of the transient peak (in terms of both transient-to-steady-state ratio and peak width) at a constant white light intensity was studied while varying the Ar^+ laser write-beam intensity. This experiment should ascertain whether the optical bias alone determines the peak width, or if all beams present (i.e. including the write-beams) are influential.

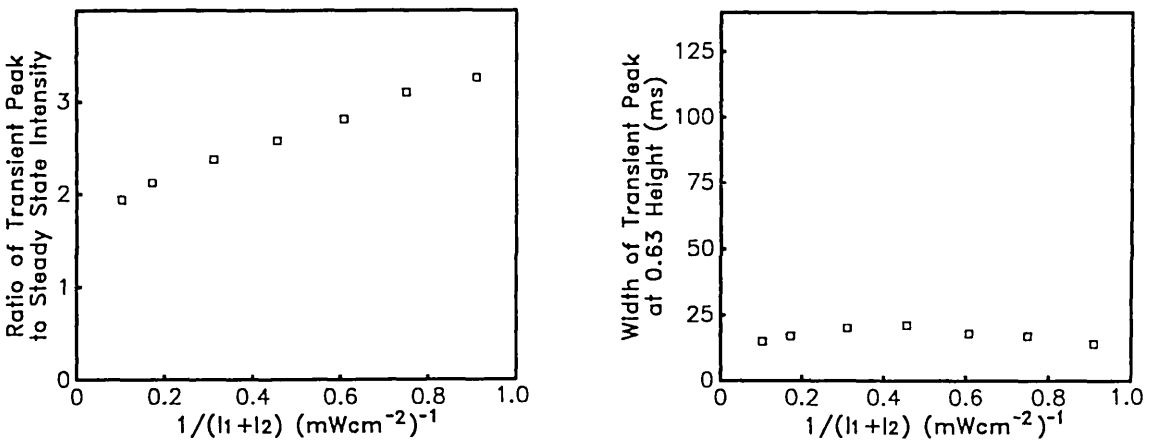

Figure 5.10 Demonstration that the optical bias alone appears to determine the peak width, regardless of the write-beam intensity.

From Figure 5.10, it is seen that although the transient-to-steady-state ratio is determined by the ratio of white light to write-beam intensity, as before, the width of the transient peak does not significantly change over the same range of write-beam intensity as in Figure 5.9. Therefore it appears that the optical bias alone determines the peak width, irrespective of the write-beam intensity.

In summary, the ratio of transient-peak to steady-state diffraction efficiency is determined by the ratio of optical bias to (useful) write beam intensity, while the peak width of the transient peak is determined by the absolute intensity of the optical bias.

5.3.5 Effect of Fringe Spacing

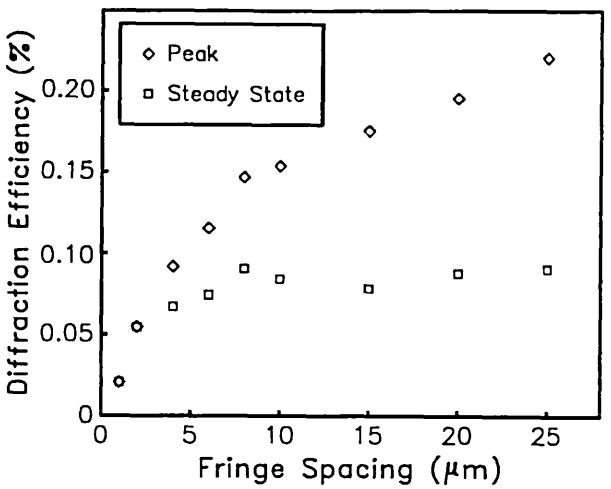

Figure 5.11 Variation of transient and steady-state diffraction efficiency as a function of fringe spacing.

For this experiment the fringe spacing was set to various values by adjusting the angle between beams I_1 and I_2. At each setting of Λ the HeNe incidence angle was adjusted for optimum Bragg-matching, passing through the same region of the crystal each time. The relative beam intensities were set such that a transient-to-steady-state ratio of about 2:1 was obtained at Λ = 20 μm. It can be observed from Figure 5.11 that the transient peak is greater than the steady state diffraction efficiency for grating periods greater than about 4 μm. It is interesting to note that this is similar in magnitude to the reported fringe spacing [2.13] above which transient energy transfer is in excess of the steady state transfer. Also, a prerequisite for TET is that there must be an intensity imbalance between the two writing beams; i.e. optical bias must be present, as here.

5.3.6 Effect of Applied Field

An experiment was conducted to investigate the effect of an applied field on the transient peak. For this experiment the grating spacing was set to 20 μm and the white light intensity was adjusted to give a transient-to-steady-state ratio of approximately 2:1. The voltage applied across the 8 mm wide crystal was adjusted between 1500 and 5000 Volts.

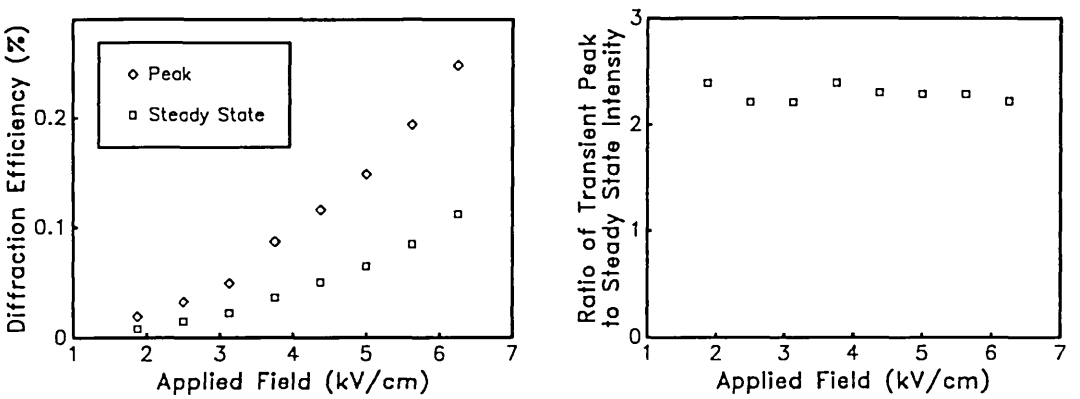

Figure 5.12 Variation of a) transient and steady-state diffraction efficiency, and b) transient-to-steady-state ratio, as a function of applied electric field.

The results that were obtained on increasing the field were interesting in that although both the steady-state and transient diffraction efficiencies increased as expected (see Figure 5.12 a), following the quadratic dependence [5.1], the ratio between them was fixed (Figure 5.12 b); i.e. the applied field does not significantly affect the transient-to-steady-state ratio over this range.

5.3.7 Variation with Chopping Time

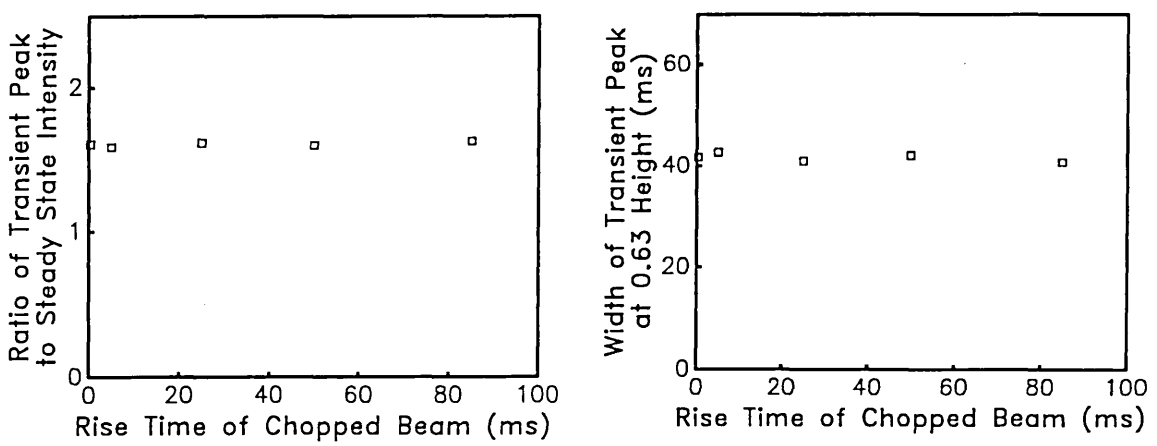

Figure 5.13 Variation of a) transient-to-steady-state ratio, and b) transient peak width as a function of 'chop-time'.

An experiment was conducted to determine the effect of the chopping characteristics of beam I_1 on the transient properties of the diffracted beam. The chopping time is defined here as the rise time of the intensity of beam I_1 after it has passed through the two lens and optical chopper system. The chop-time was then varied simply by moving the chopper axially. It is seen from Figure 5.13 that the chop-time has no effect on either the transient-to-steady-state ratio or (more surprisingly) the transient peak width.

5.3.8 Crystallographic Orientation

The transient effect was studied under identical conditions for both crystallographic orientations (two-wave and four-wave mixing orientations). It was found that neither orientation produced a greater transient enhancement but the four-wave mixing orientation was preferred because of its higher (steady-state and transient) diffraction efficiency.

5.3.9 Comparison of the Transient Characteristics of Photocurrent and Diffracted beam

In an attempt to comprehend the physical basis of this phenomenon, the transient characteristics of all parameters involved in the grating formation were studied. A system was set up to measure simultaneously the diffracted beam, the photocurrent passing through the crystal and the write-beams (to detect any transient energy transfer). This was achieved using the system shown in Figure 5.14.

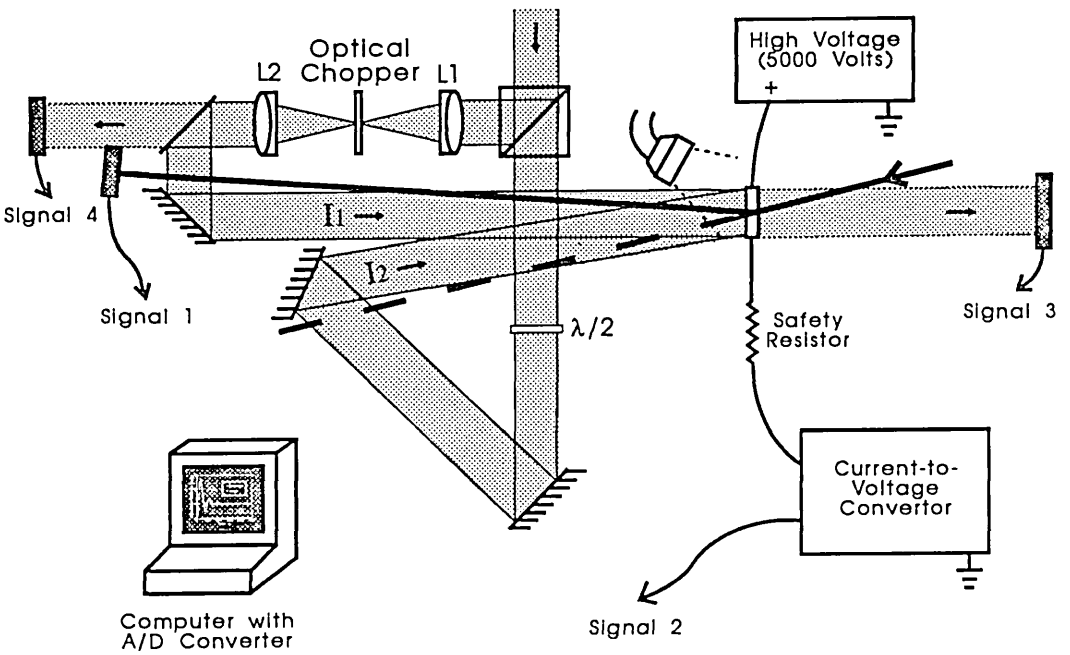

Figure 5.14 System used to measure the diffracted beam, the photocurrent, and the write-beam simultaneously. All signals pass to a multi-channel A/D converter (Metrabyte DASH8) in the PC.

The diffracted beam was measured as before using a photodetector. Also, the write-beam which would receive energy during transient energy transfer was incident on a photodetector after traversing the crystal.

The photocurrent was measured using a high-input-impedance Op-Amp (LF411CN) as a current-to-voltage converter. The sampling and feedback resistors of the electronic circuit could be changed such that the sensitivity of the device was adjusted to produce a 5 Volt output (compatible with the input sensitivity of the A/D converter) from inputs

across the range 1 μA to 100 μA. The details of this circuit are given in Appendix A.

A third photodetector was positioned to measure a component of I_1 after the optical chopper, which would act as a reference for the signals.

All the signals from the Op-Amp and the photodetectors were fed into a Metrabyte DASH8 multi-channel A/D converter. The data acquisition was controlled via the ASYST software package, which allowed immediate viewing and analysis of the data. Figure 5.15 shows the set of data that was acquired for the case when there was a significant level of optical bias on the crystal; i.e. corresponding to the trace shown in Figure 5.2 b). It is observed that there is no significant corresponding transient peak in the photocurrent or energy transfer. This experiment, therefore, provided no further direct elucidation of this transient enhancement effect. However, it did show that the effect could exist without the presence of significant transient energy transfer.

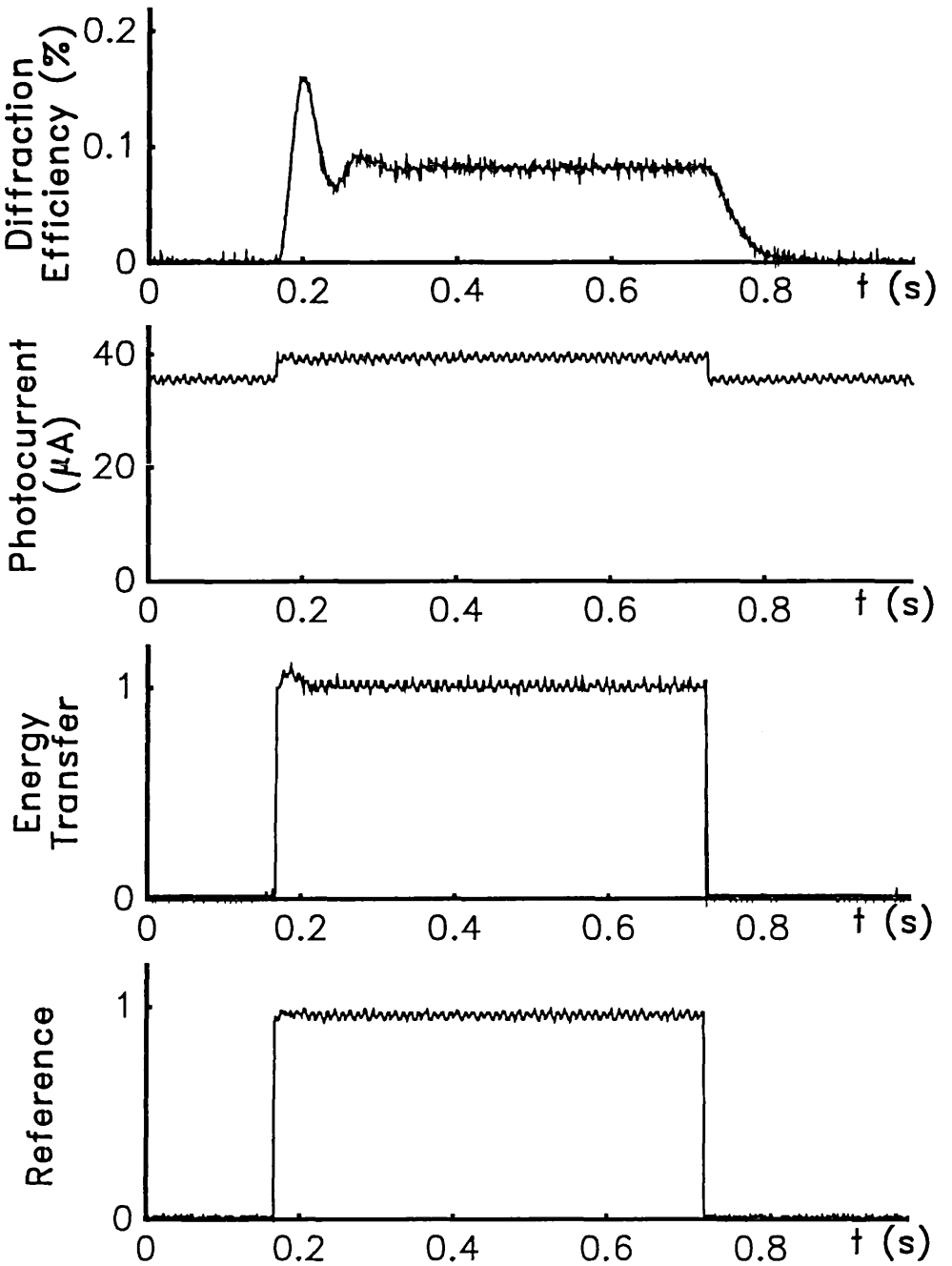

Figure 5.15 Set of plots allowing comparison of the transient characteristics of (from top to bottom) the diffracted beam, the photocurrent, the Ar^+ laser write-beam that receives energy transfer, and the reference derived from the chopped beam I_1.

Complete sets of data were acquired using the above experimental configuration for four levels of optical bias (in this case using an Ar^+ laser beam to avoid modulated photocurrent effects). Also,

corresponding data were obtained for the optically and electrically identical situation except that the two write beams were perpendicular; i.e. no grating was formed. The results obtained for these experiments are presented in Appendix B. It is interesting that in most cases when a grating is formed there is significant temporal variation of the photocurrent, whereas in the case for perpendicularly polarised write-beams the photocurrent rise time is essentially instantaneous.

The first consequence of this result is that clearly, under these conditions, the photocarrier density is not fixed with time as the photocurrent is a direct indication of the photocarrier density. This means that there should be careful examination of the linearising assumption, $\frac{\partial n}{\partial t} = 0$, that was used to solve the Kuhktarev equations in chapter 2 and by other authors.

Also, from examination of the data, it is seen that when the grating is formed with maximum modulation, the photocurrent decreases with time, whereas when the grating is erased (with uniform light) the photocurrent increases with time (both on time scales comparable to the formation and decay times of the diffraction efficiency). What this suggests is that in fact there is a limited number of photocarriers available within the volume of the crystal, and as the photocarriers move through the dark regions of the crystal they are trapped and take no further part in the photoconduction process. This limited number of photocarriers is not commensurate with the band transport models of Kuhktarev and others, but is fully in line with a charge hopping model such as that postulated by Feinberg et al. This will be discussed further later in this chapter, following an attempt to mathematically model the experimental data using the band transport equations.

5.3.10 HeNe or Ar^+ Laser Readout

Finally, for practical device considerations it is of interest to consider the possibility of using an Ar^+ laser beam (or other beam of similar wavelength) to play the dual role of supplying the optical bias and reading out the grating. This would mean that the expected drop in the steady-state diffraction efficiency (due to the addition of the optical bias) would be compensated for by the increase in the beam that is actually reading the grating. In other words, transient enhancement

could be obtained, because of the addition of the optical bias, without the attendant drop in the absolute diffracted intensity. Clearly, in terms of devices based on this phenomena, this would be highly beneficial.

This possibility was investigated by providing as the optical bias an Ar^+ laser beam which was incident at the Bragg angle. Therefore,this beam was both supplying the optical bias and reading out the grating. A HeNe laser beam was simultaneously incident at the Bragg angle appropriate to its wavelength, and so readout was maintained at both the HeNe and Ar^+ laser wavelengths as the optical bias (third Ar^+ laser beam) was increased.

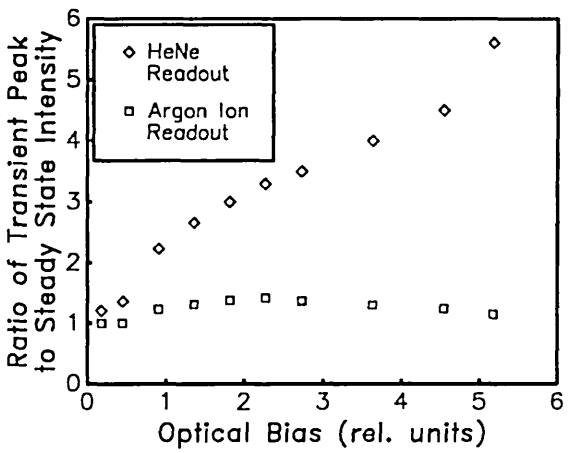

Figure 5.16 An experimental plot showing the transient enhancement achievable when different forms of readout are used.

Unfortunately, Figure 5.16 shows that no significant transient enhancement was detected in the Ar^+ laser read-beam, although the HeNe laser beam does exhibit a steadily increasing enhancement.

The reason for the absence of significant transient enhancement when using an Ar^+ laser beam to perform the dual role is unknown. It is hoped however, that these data will provide further background information in the pursuit of a reasonable explanation for the transient effects presented in this chapter.

5.4 Analysis

To establish whether the Kukhtarev single-carrier band transport model predicts the observed transient effects with optical bias, it is necessary to re-evaluate the temporal evolution of E_{sc}, using expressions for the incident intensity and resulting photoelectron distributions which explicitly contain a term corresponding to the optical bias.

The intensity at the crystal should thus be expressed as;

$$I(z) = I_{ob} + I_o + 2(I_1 I_2)^{1/2}(e^{iKz} + e^{-iKz}) \tag{5.1}$$

where I_{ob} is the intensity of optical bias (it is clear that $I_{ob} \equiv I_3$) and $I_o = (I_1 + I_2)$. The resulting photoelectron distribution will then be of the form;

$$n(z) = n_{ob} + n_o + \frac{n_o}{2}(ae^{iKz} + a^* e^{-iKz}) \tag{5.2}$$

where n_{ob}, n_o are the number of photoelectrons that would be generated if the crystal was illuminated with uniform illumination of intensity I_{ob} and I_o, respectively.

It is clear that the ionised donor distribution must still be limited by N_A, and so the expression for the spatial variation of ionised donors remains;

$$N_D^+(z) = N_A + \frac{N_A}{2}(Ae^{iKz} + A^* e^{-iKz}) \tag{5.3}$$

where A is the parameter that indicates the level of modulation of the available trapping density.

Also, the spatial distribution of the electric field in the sample will be unaffected by the level of optical bias (assuming the BSO crystal is by far the dominant source of resistance in the electrical circuit - this was experimentally verified and values are quoted in Appendix A) Therefore;

$$E(x) = E_o + E_{sc}(z) = E_o + \frac{1}{2}(E_{sc}\, e^{iKz} + E_{sc}^* e^{-iKz}) \tag{5.4}$$

In order that a solution for the temporal variation of E_{sc} can be obtained, it is necessary to substitute the experimental conditions, given by equations (5.1) to (5.4), into the one-dimensional rate equations (2.10) - (2.13). Specifically the rate equation for the immobile ionised donors was given as;

$$\frac{\partial N_D^+(z)}{\partial t} = G - R \tag{5.5}$$

By substituting equations (5.1) to (5.4) into (5.5) and equating coefficients of e^{iKz}, one obtains;

$$\frac{\partial A}{\partial t} N_A = (n_{ob} + n_o)\tau^{-1}\left[m' - A - \Re a\right] \tag{5.6}$$

where m′ and $\Re$ are defined by $m' = \frac{2(I_1 I_2)^{1/2}}{I_1 + I_2 + I_3}$ and $\Re = \frac{n_o}{(n_{ob} + n_o)}$.

Gauss's Law was stated in the form of equation (2.13) as;

$$\varepsilon\varepsilon_o \frac{\partial E(z)}{\partial z} = q(N_D^+(z) - N_A) \tag{5.7}$$

Substitution of equations (5.1) to (5.4) into (5.7) yields;

$$iK\varepsilon\varepsilon_o E_{sc} = qAN_A \tag{5.8}$$

In order that equations (2.10) to (2.13) could be linearised to provide an analytically soluble system of equations, the quasi-stationary approximation was used, i.e. $\frac{\partial n}{\partial t} = 0$. We can now see that, from the data given in Appendix B, this approximation is only valid for the case with significant optical bias ($I_{ob} \simeq 2I_o$). In other words, for this case there is no significant temporal variation of the photocurrent (a direct indication of the photocarrier distribution) on the same time scale as the grating formation. Therefore, this solution is again only valid for low grating modulation, a condition that has already (coincidently) been imposed. Therefore;

$$G - R = -\frac{1}{q}\frac{\partial J(z)}{\partial z} \tag{5.9}$$

Substituting equations (5.1) to (5.4) into (5.9) yields;

$$(n_{ob} + n_o)\tau^{-1}\left[m' - A - \Re a\right] = -iK\mu(n_{ob} + n_o)E_{sc} - iK\mu n_o a E_o + K^2 D a n_o \tag{5.10}$$

An expression for a can be obtained on rearrangement of equation (5.10);

$$a = \frac{1}{\Re}\,\frac{m' - A + iK\mu\tau E_{sc}}{1 + K^2 D\tau - iK\mu\tau E_o} \qquad (5.11)$$

By substituting this expression for a and the expression for A from equation (5.8) into equation (5.6) produces the following expression for the temporal variation of E_{sc};

$$\frac{\partial E_{sc}}{\partial t} = -\frac{(n_{ob} + n_o)q\mu}{\varepsilon\varepsilon_o}\left[\frac{m'(E_o + iE_D) + E_{sc}(1 + K^2 l_S^2 - iKl_E)}{(1 + K^2 r_D^2 - iKr_E)}\right] \qquad (5.12)$$

This differential equation has the following solution;

$$E_{sc} = -\frac{m'(E_o + iE_D)}{1 + K^2 l_S^2 - iKl_E}\left[1 - \exp\left(-\frac{(1 + K^2 l_S^2 - iKl_E)}{\tau_M'(1 + K^2 r_D^2 - iKr_E)}\,t\right)\right] \qquad (5.13)$$

where $\tau_M' = \dfrac{\varepsilon\varepsilon_o}{q\mu(n_{ob} + n_o)}$.

By comparison of equations (5.13) and (2.21) it can be seen that the steady-state values of E_{sc} for the cases with and without optical bias are scaled by the values of m′ and m respectively, as expected. The other change, also as expected, is that the overall transient characteristics of E_{sc} are scaled by a Maxwell relaxation time which now contains a component due to the optical bias.

Of more interest here is how equation (5.13) relates to the prime experimental measurements, i.e. the effect of optical bias on the transient-to-steady-state diffraction efficiency ratio.

It is seen that the general form of equation (5.12) is given by;

$$E(t) = (a + ib).[1 - \exp\{-(c + id)t\}] \qquad (5.14)$$

where a,b,c and d are real parameters. The characteristics of equation (5.14) can now be studied and related to the physical process.

As was mentioned before, it is the complex argument of equation (5.14) that predicts that damped oscillatory behaviour will occur. In other words, a transient peak is expected in the space-charge field. Clearly then, the general form of equation (5.14) qualitatively predicts

the transient enhancement results obtained experimentally. However, further investigation is necessary to assess whether it quantitatively predicts them.

In chapter 2 it was seen that η, the diffraction efficiency, is proportional to $|E_{sc}|^2$. Thus the general form for the temporal variation of η is given by;

$$\eta(t) \propto |(a + ib).[1 - \exp\{-(c + id)t\}]|^2 \qquad (5.15)$$

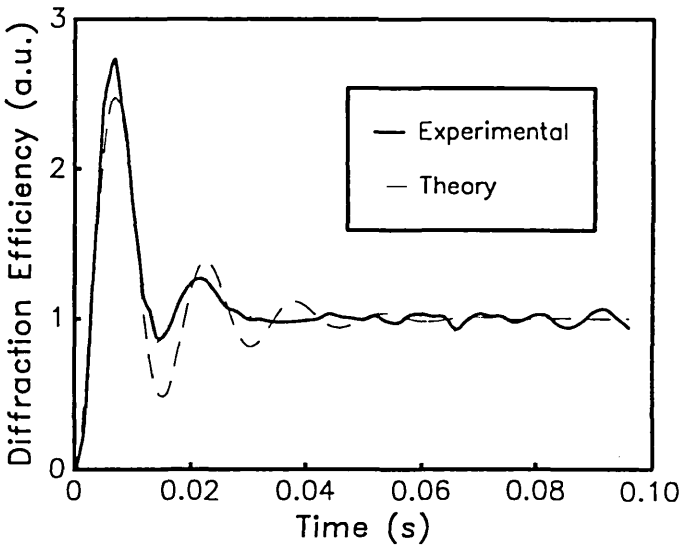

Figure 5.17 Comparison of the experimental data for $I_{ob} \sim 2I_o$ with the general expression given by equation (5.1). $m' \sim 0.2$, $\Lambda = 20\ \mu m$, $E_o = 6.3\ kVcm^{-1}$.

A non-linear curve fitting routine was employed to fit equation (5.15) to the experimental data obtained for the case when $I_{ob} \sim 2I_o$. It is observed (Figure 5.17) that, qualitatively, a reasonable fit to the data is obtained, although the experimental data appear to be overdamped. This overdamping has been observed by other authors in related holographic 'time-of-flight' experiments [5.2] and has been attributed analytically to a spatially varying drift mobility.

If equation (5.15) is taken, to a first approximation, as the general form required to model the experimental data, then it is necessary to examine how the parameters *a,b,c* and *d* relate to the prime experimental 'figure-of-merit' - the transient-to-steady-state

diffraction efficiency ratio.

From computer simulations of equation (5.15) it was found that, for values corresponding to the range of experimental data, there was a linear relationship between the ratio of the first maximum, η_p, of (5.15) to the steady-state value, η_{ss}, and the ratio d/c (to within 3 %). Specifically;

$$\frac{\eta_p}{\eta_{ss}} \approx 0.35 \frac{d}{c} + 0.8 \tag{5.16}$$

over the experimentally obtained values of η_p/η_{ss}. Thus, if equation (5.15) is the general form of the solution for the temporal variation of diffraction efficiency, then the transient-to-steady-state intensity ratio is determined by the ratio of the imaginary to real components of the argument of (5.15); (and the steady-state value is given by $|(a + ib)|^2$).

A normalised form of solution to equation (5.12) is given by;

$$E_{sc} = 1 - \exp\left[- \frac{(1 + K^2 l_S^2 - iK l_E)}{\tau_M'(1 + K^2 r_D^2 - i K r_E)} t \right] \tag{5.17}$$

Thus, the ratio of d/c can be seen to be;

$$\frac{d}{c} = \frac{K r_E + K^3 r_E l_S^2 - K l_E - K^3 l_E r_D^2}{1 + K^2 r_D^2 + K^2 l_S^2 + K^4 r_D^2 l_S^2 + K^2 l_E r_E} \tag{5.18}$$

This expression can be simplified to a certain degree, by examining the specific experimental conditions initially used to investigate the effect of optical bias; i.e. $\Lambda = 20$ μm and $E_o = 6.3$ kVcm^{-1}. Thus, using the value for r_D of 0.6 μm from reference 5.1;

$$\frac{d}{c} = \frac{K r_E + K^3 r_E l_S^2 - K l_E}{1 + K^2 l_E r_E} \tag{5.19}$$

The most immediate feature of equation (5.19) is that it contains no reference to any terms derived from the optical bias. Clearly then, the single-carrier band transport model does not predict in detail the behaviour of the experimental data on varying the level of optical bias, as presented in this chapter.

There are several possibilities for modification of the mathematical analysis, in order that it may predict the experimental data. These are; the use of a model which allows for two species of photocarrier - this produces grating dynamics with two (fast and slow) characteristic time-constants [5.3,5.4]; the use of a multiple trap-level model which allows the possibility of multiple phase-shifted gratings with independent characteristic time-constants [5.5]; and finally the use of a charge-hopping model such as that derived by Feinberg et al. The hopping model predicts damped oscillatory behaviour in the build-up of the space-charge field, and some experimental evidence suggests that it may in fact be the dominant transport mechanism in BSO [5.6,5.7,section 5.3.9 above].

Due to time constraints, detailed investigation of these possibilities was not accomplished within the confines of this thesis. However, it is anticipated that these options will provide a rich source for future work, with efforts incorporating the data presented in Appendix B.

5.4 Conclusions

While a detailed analysis of the transient effect was not readily achieved, the experimental study carried out provided ideal characteristics to be established for the implementation of transient devices using BSO. As this was the ultimate aim of this thesis, efforts were switched to development of applications (details given in the next chapter) based on the reported experiments. The control over the transient properties of a diffracted beam that is afforded by this system makes it very attractive for devices. It is believed that this control makes it more useful than other methods of transient enhancement (such as the use of TET), and this is discussed in the context of the demonstration of a novelty filter.

Chapter Six
Optical Information Processing Systems

In this chapter, details are given of various optical processors that were constructed using BSO as a dynamic holographic medium. Unfortunately, the implementation of completely real-time optical processing systems is hampered by the cost and quality of the currently available spatial light modulators (SLM's). Most of the applications described here, therefore, are simply demonstrations of principle, using static transparencies or test slides as the input objects. It is expected that these results can be generalised to completely real-time systems when suitable SLM's become available.

6.1 Coherent Optical Correlator

In this section details will be given of a coherent optical correlator based on BSO, and results presented for the case of simple binary amplitude transparencies as the input objects.

The process of optically correlating (or convolving) two input signals generally relies on the Fourier transforming property of a converging lens. This enables the Fourier transform (F.T.) of the input signal to be formed (essentially instantaneously) within the volume of the holographic medium. If two or more of these input signals are illuminated with spatially and temporally coherent beams, then the resulting optical interference pattern will be proportional to the multiplication of the Fourier transforms. This interference pattern can then be recorded in a holographic material, in this case via the photorefractive effect as a volume phase grating. Consequently, the profile of a beam which is diffracted from the refractive index grating will contain optical information of the input signals. This diffracted beam, if subsequently Fourier transformed by another lens, will produce the desired optical correlation in its focal plane.

6.1.1 Joint-Transform Correlator

Various types of optical correlator have been previously

demonstrated using BSO [6.1-6.3]. After exploratory work on several different configurations it was found that the most successful was the Joint-Transform Correlator (JTC) [6.4] previously demonstrated using BSO by Pichon et al in 1980 [6.1]. In this type of correlator the holographic grating is produced by the interference pattern formed from the Fourier transforms of two input signals. This grating is then read out by a plane wave beam. In a frequency-plane correlator [6.2], on the other hand, the grating is produced by the interference of the F.T. of one input signal with a plane wave reference beam, in analogy to the conventional VanderLugt filter [6.5]. The resulting frequency-plane filter is then probed by the F.T. of the second input signal. Both the joint-transform and frequency plane configurations have their respective merits, and will be assessed later in section 6.1.5. The distinction between the joint-transform and frequency-plane geometries is only necessary when a PR medium is used as a dynamic holographic medium, as here. When a phase conjugate geometry is used to implement the correlator, all beams have equal status; i.e. there are no distinct write/read processes.

6.1.2 Analysis of JTC Optical System

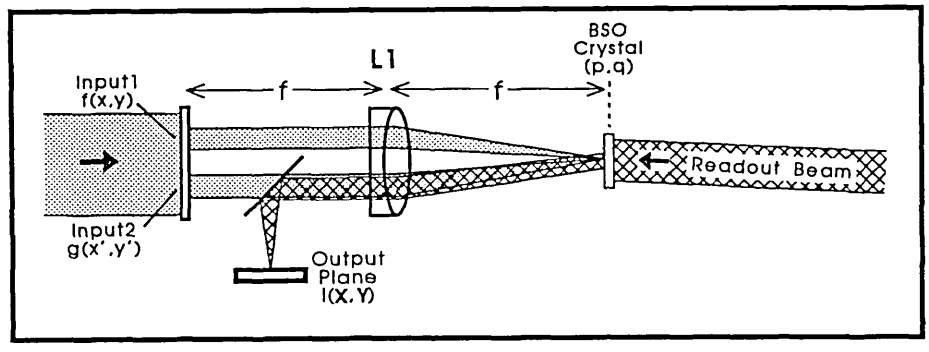

Figure 6.1 Schematic diagram showing the various input, filter and output planes of the joint-transform correlator.

The relationship between the input, BSO and output planes can be seen in figure 6.1. Inputs 1 and 2 are binary amplitude objects described by f(x,y) and g(x',y') respectively, where x'= x - b and y' = y; i.e. b is the distance between the two inputs in the (x,y) plane. The light field pattern at the crystal plane, (p,q), (located

in the back focal plane of L1) will then be given by the F.T. of inputs 1 and 2. The F.T. of f(x,y) is given by;

$$F(p,q) = \int_{-\infty}^{\infty}\int f(x,y).\exp\{ \frac{-i2\pi}{\lambda_{514} f} [xp + yq]\} dxdy \qquad (6.1)$$

where f is the focal length of L1. Similarly, the F.T. of g(x',y') will be given by;

$$G(p,q) = \int_{-\infty}^{\infty}\int g(x',y').\exp\{ \frac{-i2\pi}{\lambda_{514} f} [x'p + y'q]\} dx'dy' \qquad (6.2)$$

The intensity pattern in the plane of the crystal is then;

$$I(p,q) = | F(p,q) + G(p,q) |^2 \qquad (6.3)$$

From chapter 4.8 it was seen that this intensity pattern will produce a crystal transmittance which can be expressed in the form;

$$t(p,q) \simeq 1 + i \gamma F(p,q)G^*(p,q) \qquad (6.4)$$

The readout HeNe beam is incident on the BSO crystal at the angle which accommodates the change in wavelength, such that it Bragg-matches to the volume phase grating. The readout beam is then given by;

$$R(p,q) = R_o \exp\{ \frac{-i2\pi}{\lambda_{633}} p \sin\theta \} \qquad (6.5)$$

where θ is the external angle that the readout beam makes with the normal to the (p,q) plane. The light pattern immediately following the crystal will then be given by;

$$E(p,q) = R(p,q)\ t^*(p,q) \qquad (6.6)$$

where the conjugate transmission function is encountered by the readout beam as it is counter-propagating with respect to the writing beams. The output of the JTC is readily calculated as the diffracted light will propagate back through L1 and so the light at the (**X**,**Y**) plane will be the Fourier transform of E(p,q). Thus the output light distribution, I(**X**,**Y**), is given by;

$$I(\mathbf{X},\mathbf{Y}) = \int_{-\infty}^{\infty}\int R(p,q)\ t^*(p,q).\exp\{ \frac{-i2\pi}{\lambda_{633} f} [p\mathbf{X} + q\mathbf{Y}]\} dpdq \qquad (6.7)$$

substituting equations (6.1), (6.2), (6.4) and (6.5) into (6.7) and

performing the integration yields the following expression for the output light distribution;

$$I(X,Y) = \int_{-\infty}^{\infty}\int f(x - D - \frac{514}{633} X,\ y - \frac{514}{633} Y).g^{*}(x - D,\ y)\ dxdy \qquad (6.8)$$

which is the cross-correlation of f(x,y) with g(x,y). The displacement, D, from the optic-axis is given by $D = b + \frac{514}{633} f \sin\theta$ and the output plane is scaled by the metric, $\frac{514}{633}$.

6.1.3 Experimental Configuration for the JTC

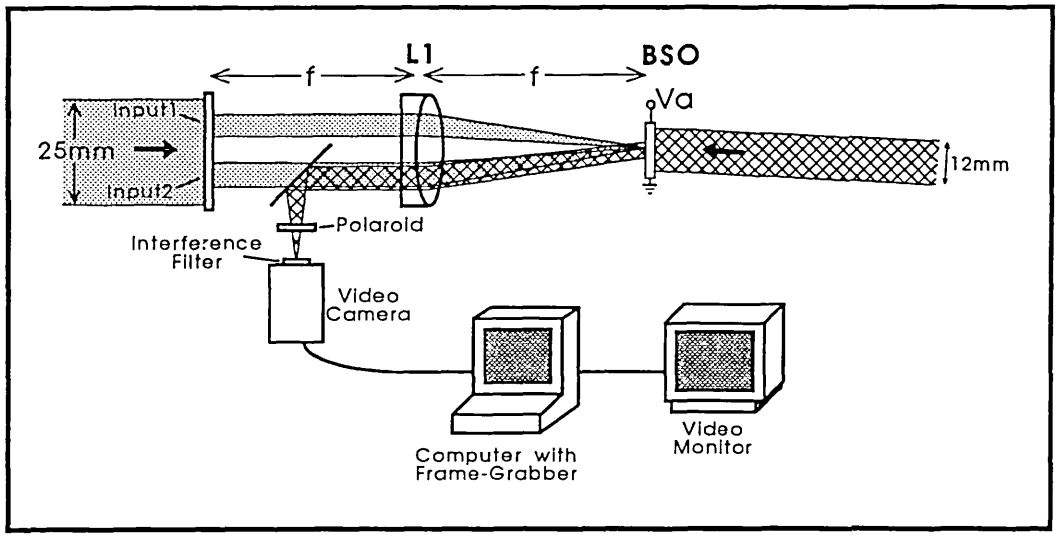

Figure 6.2 Experimental configuration used to implement the joint-transform correlator.

The experimental set-up for the coherent joint-transform correlator is shown in figure 6.2 . Inputs 1 and 2 were produced using high contrast photographic film and are each approximately 4 mm in extent. They were produced on the same slide and are separated by 4 mm. The Ar^{+} laser is spatially filtered and expanded to about 25 mm to give approximately uniform illumination across the full extent of both the input objects. The Fourier transforms of both of the inputs are formed at the crystal plane by L1. The average spatial period of the holographic fringes, and consequently the grating formed, is 20 μm. This fringe spacing was chosen to provide a reasonable field of view of

the diffracted image (section 4.6). The grating vector is parallel to the [110] crystallographic direction. A voltage of 5kV is applied across the crystal also in this direction to provide a sufficient range of charge migration to allow grating formation and to enhance the diffraction efficiency of the resulting grating.

The focal length, f, of L1 was chosen to provide a reasonable scale of F.T. It is a combination of this focal length and the greatest spatial dimension of the input objects that determines the axial deviation from f, Δz, over which the Fourier transform relationship is valid [6.6], such that;

$$\Delta z < \frac{2 f^2 \lambda_{514}}{r_{max}^2} \qquad (6.9)$$

where r_{max} is the maximum spatial extent of either of the input objects in any direction. Thus we see that the BSO crystal must lie within the tolerance Δz of the focal length of the lens to ensure that the F.T. is present throughout the volume of the crystal, otherwise a deterioration in the correlation will occur. In this configuration f = 300 mm and r_{max} = 4 mm so that Δz = 5.7 mm. Experimental verification of equation (6.9) was carried out in reference 6.1. For their experimental conditions $\Delta z \sim 5.5$ mm, and it was demonstrated that a $\pm$ 3 mm axial deviation of the crystal from the geometric focal plane resulted in a drop in the output auto-correlation peak power by a factor of two. Such practical constraints were also evident during construction of this correlator.

The readout HeNe laser beam is spatially filtered and expanded to 12 mm diameter and is incident on the BSO crystal at the Bragg angle. The diffracted component is picked off by the beam-splitter following passage through L1, which produces the F.T. in its focal plane. This plane is coincident with the input array of a CCD video camera. A 633 nm interference filter eliminates scattered Ar^+ laser light. The video signal is fed directly to a monitor for viewing and also to a PC with frame-grabber to enable capture of single video frames. The Ar^+ laser intensity was set to about 2 $mWcm^{-2}$ at the crystal. The grating response time at this setting of Ar^+ laser intensity is about 50 ms. The HeNe beam intensity is around 200 μWcm^{-2} which, together with the spectral sensitivity of BSO (section 4.1) ensured non-destructive

readout of the holographic grating. As presented in section 4.4.3, the diffracted and transmitted components of the HeNe beam emerge from the crystal with significantly different polarisation states due to the natural optical activity of BSO. This permits a good signal-to-noise ratio to be obtained via the use of a polaroid sheet at the output stage.

6.1.4 Results

Various input objects were chosen for the JTC to demonstrate the correlation/convolution nature of the output. Inputs 1 and 2 are shown in Figures 6.3-6.6 a) and b) respectively, with the corresponding output of the system shown in part c) of each figure.

It should be noted that when the inputs to the system are purely real objects (i.e. containing only amplitude information), there is no physical distinction between the operations of correlation and convolution. Whether the output obtained from this correlator is proportional to $F(p,q)G^{*}(p,q)$ (correlation) or to $F(p,q)G(p,q)$ (convolution) is simply determined by the relative orientations of the inputs. In other words to transform $G(p,q)$ to $G^{*}(p,q)$ one simply has to rotate $g(x',y')$ by 180^{o}. This is because if $g(x',y')$ is purely real, then $F.T.[g(-x',-y')] = G^{*}(p,q)$ [6.7].

It is thus simply a matter of nomenclature whether an operation carried out by a physical correlator is a correlation or convolution. It is generally regarded as a correlation operation when one input object is compared with another for a 'match'. On the other hand, the convolution operation is when one object is distributed at the locations of a set of smaller inputs. Thus Figures 6.3 and 6.4 may be regarded as the correlation of the input signals whereas Figures 6.5 and 6.6 demonstrates the operation of convolution of the two input signals.

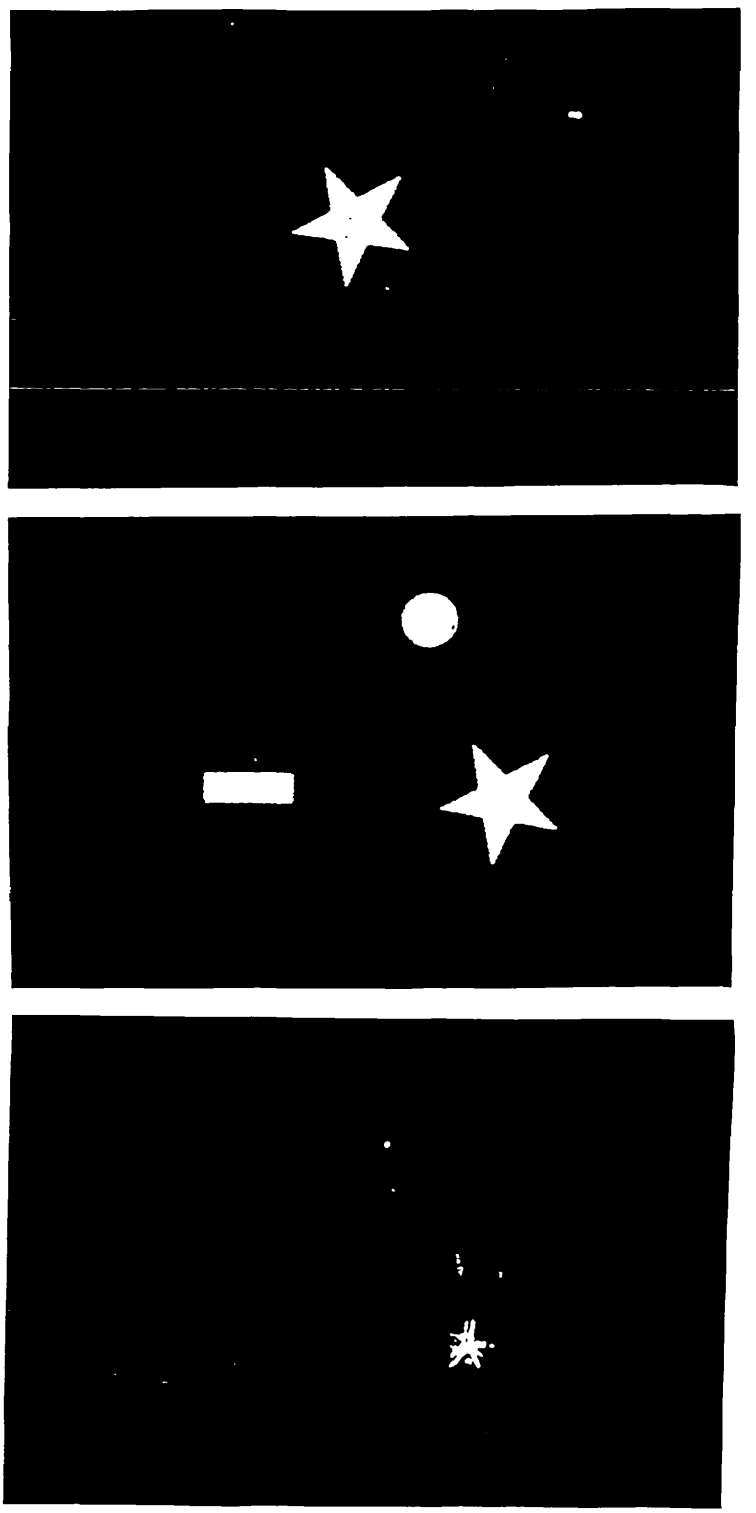

Figure 6.3 Experimental demonstration of the joint-transform correlator. From top to bottom a) Input 1, b) Input 2, and c) the corresponding output intensity pattern.

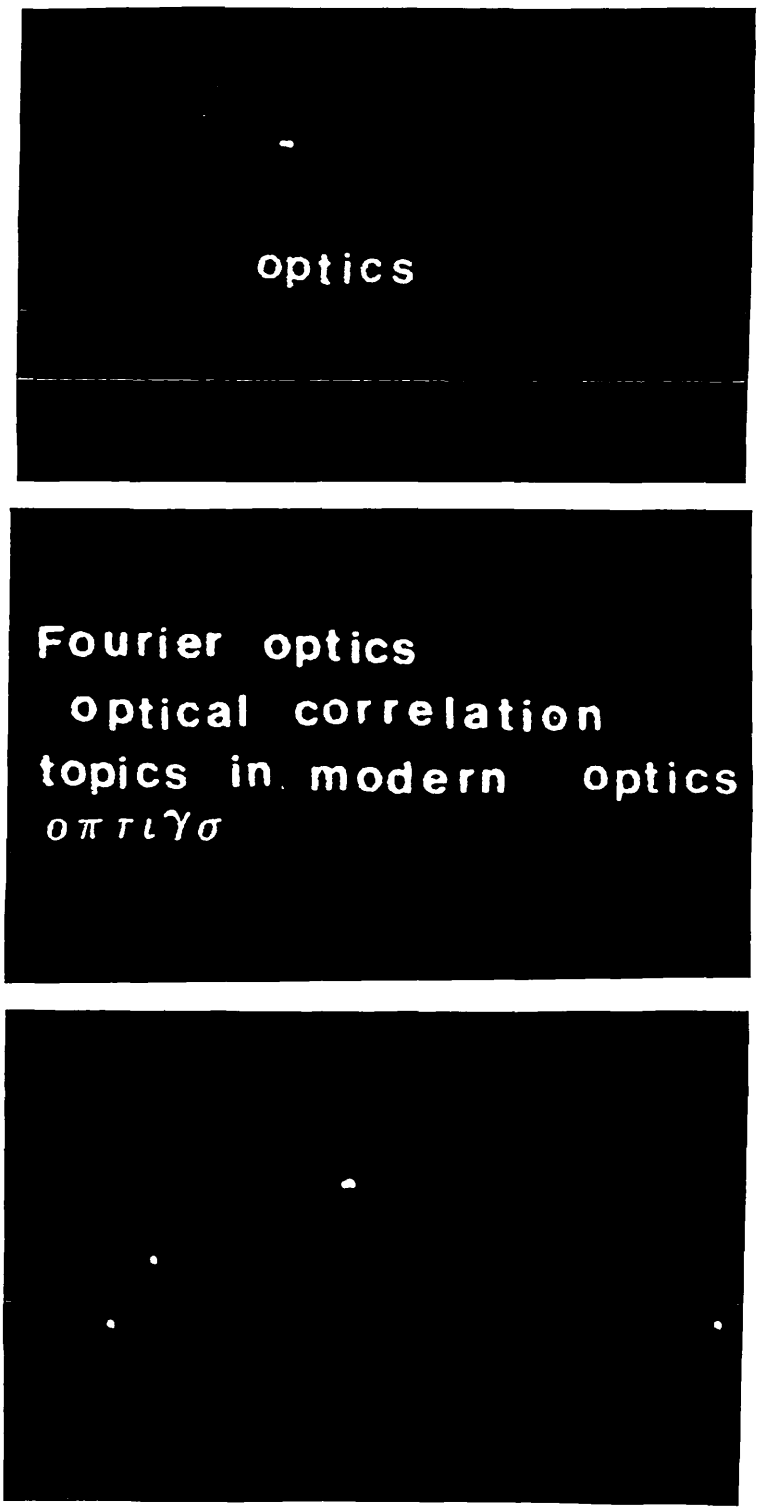

Figure 6.4 Experimental demonstration of the joint-transform correlator. From top to bottom a) Input 1, b) Input 2, and c) the corresponding output intensity pattern.

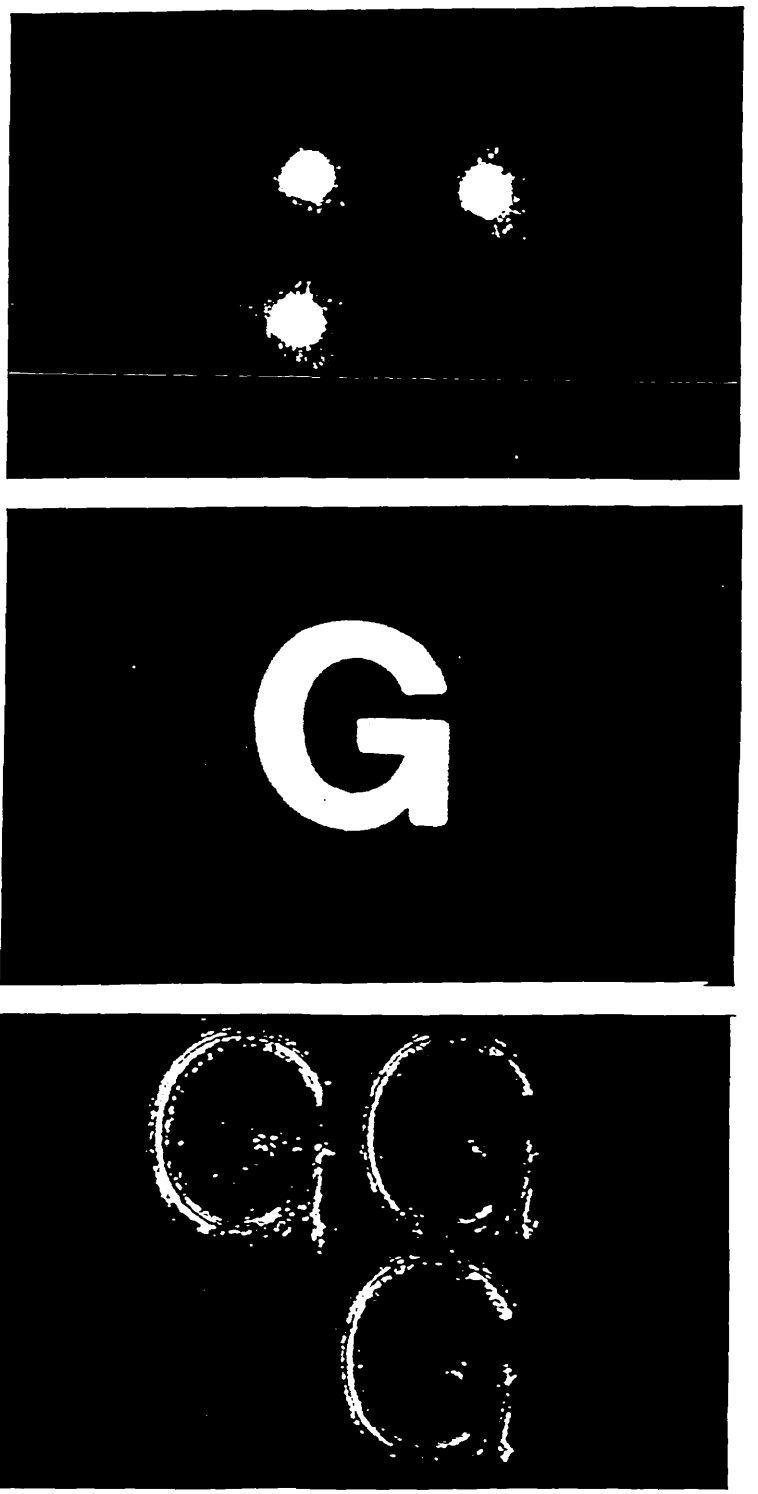

Figure 6.5 Experimental demonstration of the joint-transform correlator. From top to bottom a) Input 1, b) Input 2, and c) the corresponding output intensity pattern.

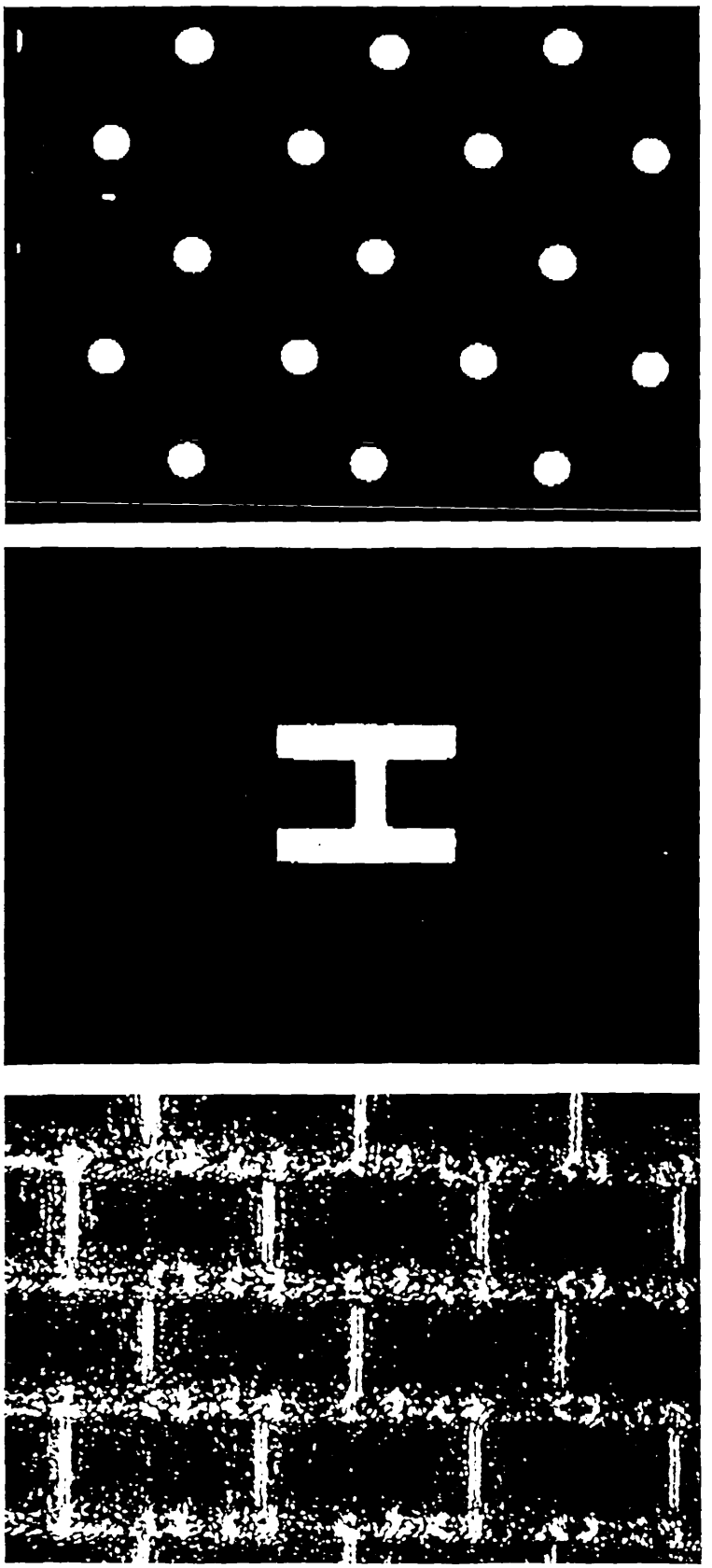

Figure 6.6 Experimental demonstration of the joint-transform correlator. From top to bottom a) Input 1, b) Input 2, and c) the corresponding output intensity pattern.

6.1.5 Conclusion

The salient features of the correlator described above can be summarised as follows;

1) With the joint-transform correlator the three F.T. operations required for correlation can be performed using just one high quality lens.

2) The use of a HeNe laser to read out the holographic gratings is non-destructive and allows the suppression of scattered Ar^+ light via the use of an interference filter.

3) The significantly different polarisation states of the transmitted and diffracted beams allows further suppression of background HeNe light by the insertion of a polaroid sheet.

4) The noise reduction techniques given by 2) and 3) above allowed respectable S/N ratios of up to 50:1 to be attained.

5) The small angle between the writing beams provided a large field of view (and good resolution) in the diffracted output, but required the application of an external electric field to facilitate formation of the grating.

6) The joint-transform correlator is good for matching identical objects as there will be good modulation at all spatial frequencies (as the intensity pattern is formed by the interference of two identical F.T. distributions), but consequently spatial filtering cannot be used to improve discrimination (section 4.7), as is possible in the frequency plane correlator [6.2].

7) The time response of the crystal is the limiting factor of this design as each time either of the inputs changes a new grating has to be formed; in contrast to the frequency plane correlator where a reference object can be stored and non-destructively read out at any rate (i.e. only when it is necessary to change the reference object of the frequency-plane correlator must a new grating be formed).

6.2 Optical Intensity Correlator

This section presents work carried out on an optical intensity correlator using BSO. The basic difference between this and the work presented on the coherent joint-transform correlator is that the intensity correlator uses spatially incoherent light to read out the grating formed in the holographic medium. This produces a correlator system with several distinct practical advantages which are outlined below.

6.2.1 Introduction

As mentioned in section 6.1, the implementation of coherent correlators based on dynamic volume holographic materials is hindered by the requirements of precise positioning of the medium at the focal plane of the transforming lens(es) [6.1], and also good overlap of the Fourier transforms of the input signals is required [6.8]. It has been demonstrated that an optical intensity correlator is free from these positional constraints [6.9]. This increased tolerance in positioning eases the implementation of an intensity correlator based on BSO. Further, due to the spatially incoherent nature of the readout beam, any spatial phase variation of components in the readout portion of the system will have no influence on the correlator output. This allows an inexpensive liquid crystal television (LCTV) to be used as a spatial light modulator (SLM) to address the holographic filters, despite its inherent phase inhomogeneities caused by the transparent electrodes and liquid crystal molecular distribution. The disadvantage of the intensity correlator is that its discrimination ability is significantly lower than that of its coherent counterpart.

Experimental results will be presented using BSO and an LCTV. Fresnel transforms of the input objects are written within the volume of a single crystal of BSO using an Ar^+ laser operating at 514 nm and simultaneously read out using a HeNe laser at 633 nm. This provides an updateable hologram as the reference of the correlator which is interrogated at frame rates by the LCTV.

6.2.2 Theoretical Basis

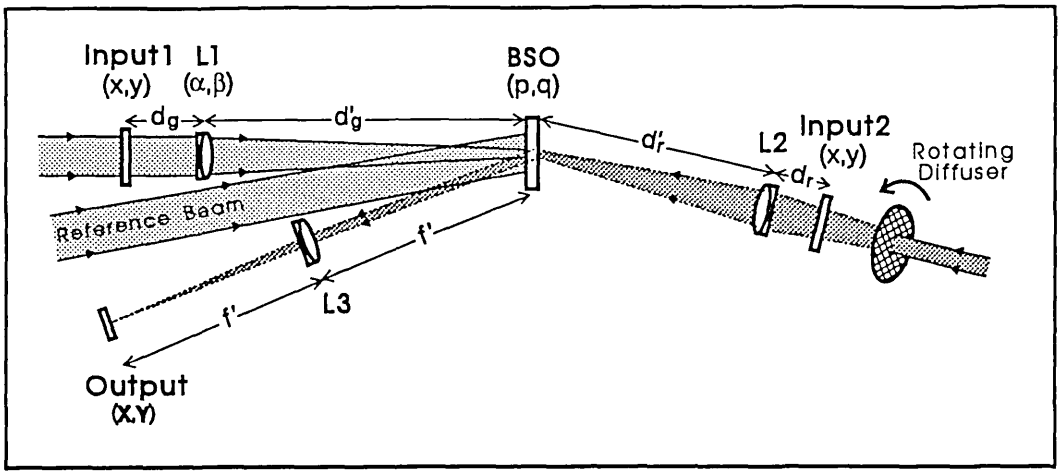

Figure 6.7 Schematic diagram of the input, filter and output planes of the optical intensity correlator

A schematic diagram of the various input, filter and output planes of the optical intensity correlator is given in Figure 6.7. Input 1 is a binary amplitude object described by o(x,y). The light field pattern at the crystal plane (p,q) due to input1 can be evaluated by considering the impulse response of the optical sub-system comprising input 1, L1 and the BSO crystal. Suppose an input impulse, $\delta(x-x_o,y-y_o)$, is in the plane of input 1. To evaluate the resultant light pattern at (p,q) we must first evaluate the distribution at the plane of the (thin) lens (α,β) due to the diffraction of o(x,y), which is analysed using the Fresnel approximation. We should then consider the phase transformation due to the lens and finally the light at (p,q) will be the Fresnel diffraction pattern of the light at (α,β). Thus, ignoring the pupil function of the lens, the response function is given by;

$$h(p,q;x_o,y_o) = \int_{-\infty}^{\infty}\int \exp\{\frac{i\pi}{\lambda_{514}d_g}[(\alpha-x_o)^2+(\beta-y_o)^2]\}.\exp\{\frac{-i\pi}{\lambda_{514}f}(\alpha^2+\beta^2)\}$$

$$.\exp\{\frac{i\pi}{\lambda_{514}d'_g}[(p-\alpha)^2+(q-\beta)^2]\}\,d\alpha d\beta \qquad (6.10)$$

where f is the focal length of the transforming lens L1 and d_g and

d_g' are the distances as shown in Fig. 1. In practice $d_g \ll f$ for the optical intensity correlator and so we are concerned here with a non-imaging system. Evaluation of the integral in (6.10) then yields the impulse response as;

$$h(p,q;x_o,y_o) = \exp\{i\pi[(\frac{1}{C_1} - \frac{K}{C_1^2})(x_o^2 + y_o^2)+(\frac{1}{C_2} - \frac{K}{C_2^2})(p^2 + q^2) - \frac{2K}{C_1 C_2}(x_o p + y_o q)]\} \quad (6.11)$$

where $C_1 = \lambda_{514} d_g$, $C_2 = \lambda_{514} d_g'$ and $C_3 = \lambda_{514} f$

and K is defined by $\frac{1}{K} = \frac{1}{C_1} + \frac{1}{C_2} - \frac{1}{C_3}$

The crystal plane is at a distance from L1 which is not generally equal to the focal length of L1. Thus the light distribution in the crystal plane may be termed the Fresnel transform of o(x,y) [6.10], of which the Fourier transform is a specific case at $d_g' = f$. The Fresnel transform of o(x,y) can be calculated from the convolution of o(x,y) with the impulse response function, i.e.;

$$O(p,q) = \int_{-\infty}^{\infty}\int o(x,y).h(p,q;x_o,y_o)\, dxdy \quad (6.12)$$

The reference beam is a plane wave and can be described by,

$$R(p,q) = R_o \exp\{ - \frac{i2\pi}{\lambda_{514}} p \sin\theta \} \quad (6.13)$$

where θ is the angle that the reference beam makes with the normal to the (p,q) plane. Assuming that the object and reference beams are of parallel polarisation, the intensity pattern in the plane of the crystal is given by;

$$I(p,q) = | O(p,q) + R(p,q) |^2 \quad (6.14)$$

As before, the necessary term of this interference pattern can be linearly recorded in BSO as a volume phase grating.

$$t(p,q) \simeq 1 + i \gamma O(p,q)R^*(p,q) \quad (6.15)$$

To calculate the output of the optical intensity correlator it is convenient to employ a procedure similar to that used to derive equation (6.11). However in this instance the illumination of input 2 is first

rendered spatially incoherent by propagation through a rotating diffuser. This produces time-averaged spatially-incoherent illumination which has been shown to be equivalent to using an extended illumination source. Thus we are interested in the irradiance, or intensity, impulse response of the optical system. Suppose that an input impulse $\delta(x-x_o,y-y_o)$ is at the plane of input 2, then by inspection of (6.11) it is clear that the complex light distribution just behind the plane of the BSO crystal will be given by;

$$E(p,q) = t^*(p,q).\exp\{i\pi[(\frac{1}{C_1} - \frac{K}{C_1^2})(x_o^2+y_o^2) + (\frac{1}{C_2} - \frac{K}{C_2^2})(p^2+ q^2) - \frac{2K}{C_1 C_2}(x_o p + y_o q)]\} \qquad (6.16)$$

where the conjugate transmission function is encountered by this beam because it is counter-propagating to the writing beams. Note that d_r , d_r' and the focal length of L2 were all chosen to accommodate the change in wavelength, i.e. $d_r = \frac{514}{633} d_g \rightarrow \lambda_{633} d_r \equiv \lambda_{514} d_g \equiv C_1$ and so on. This ensures that the Fresnel transforms formed at the crystal of inputs 1 and 2 are the same scale. The complex light distribution at the output plane (X,Y) will be given by the Fourier transform of E(p,q);

$$h(X,Y;x_o,y_o) = \int_{-\infty}^{\infty}\int E(p,q).\exp\{ \frac{-i2\pi}{\lambda_{633} f'} [\, pX + qY \,]\}\, dpdq \qquad (6.17)$$

where f' is the focal length of lens L3 such that $f' = \frac{\lambda_{514}}{\lambda_{633}} f$. The coherent impulse response of the system can be evaluated by substituting equations (6.12), (6.13), (6.15), and (6.16) into (6.17) and performing the integration. For convenience, the case of unity magnification between the input and output planes is considered here. This means choosing C_1, C_2 and C_3 to satisfy the condition $\frac{K C_3}{C_1 C_2} = 1$ and yields the following expression for the coherent impulse response;

$$h(X,Y;x_o,y_o) = \xi(X,Y;x_o,y_o).o^*(x_o + f\sin\theta + X,\ y_o + Y) \qquad (6.21)$$

where $\xi(X,Y;x_o,y_o)$ contains all the purely imaginary components of the solution. The irradiance impulse response of the optical system,

$h_i(X,Y;x_o,y_o)$, will then be given by;

$$h_i(X,Y;x_o,y_o) = | \; o(x_o + f\sin\theta + X,\; y_o + Y) \; |^2 \qquad (6.22)$$

If an optical signal with an intensity distribution of $|o(x,y)|^2$ is in the input 2 plane, the intensity at the output plane, according to optical linear system theory, would be the convolution of $|o(x,y)|^2$ with $h_i(X,Y;x_o,y_o)$ i.e.;

$$I(X,Y) = \int_{-\infty}^{\infty}\int |o(x,y)|^2 \; | \; o(x + f\sin\theta + X,\; y + Y) \; |^2 \, dxdy \qquad (6.23)$$

which is recognised as the intensity auto-correlation of o(x,y).

6.2.3 Experimental Configuration

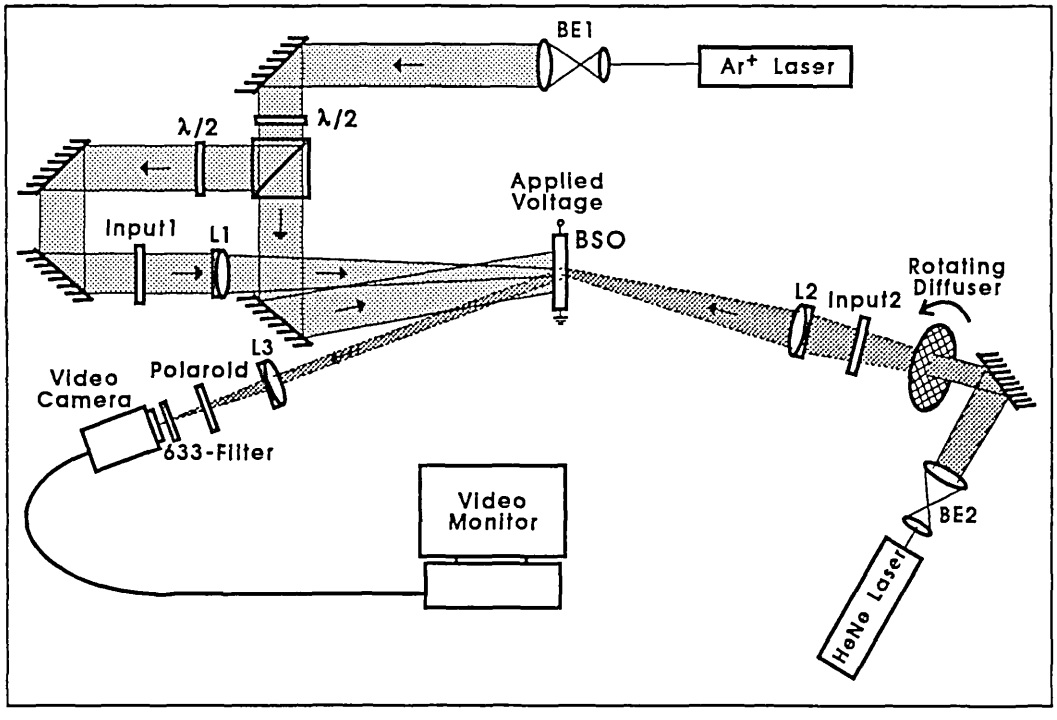

Figure 6.8 Experimental configuration for the optical intensity correlator. BE1,BE2, beam expanders; L1-3, achromatic doublet lenses, L1 :- 30 cm focal length, L2,3 :- 25 cm focal length; λ/2, half-wave plates.

The experimental set-up for the optical intensity correlator is shown in Figure 6.8. A BSO crystal of dimensions 10 x 8 x 2 mm^3,

supplied by Sumitomo Industries, was used for the experiment. The Ar^+ laser operates in single longitudinal mode and the output beam is spatially filtered and expanded to 15 mm diameter before being split by a polariser cube. One beam passes through input 1 and a convenient scale of Fresnel transform is formed in the volume of the crystal by L1. The second beam acts as the reference and is directly incident on the (1$\bar{1}$0) face of the crystal. The average spatial period of the holographic fringes is 20 μm. The HeNe read beam is expanded to 10 mm diameter before passing through a rotating diffuser to minimise the speckle size of the emergent spatially incoherent beam. This beam illuminates input 2 and a Fresnel transform of this input image is obtained at the crystal by L2. The readout beam is incident on the crystal with the usual restriction of Bragg-matching to the volume phase hologram. The component of the read beam diffracted by the refractive index grating is collected by lens L3 to produce the intensity correlation in its back focal plane, which coincides with the face of a video camera. Background noise is considerably reduced by the use of an interference filter and polaroid. The video output from the camera is connected to a monitor. The total Ar^+ laser intensity at the crystal was set at about 2 $mWcm^{-2}$. The HeNe intensity is at least two orders of magnitude lower than this. All beams are incident on the crystal with horizontal polarisation.

6.2.4 Experimental Results

For preliminary demonstration of the optical intensity correlator both inputs 1 and 2 were binary amplitude objects fabricated from high-contrast photographic film and are as viewed in Figure 6.9 a) and b) respectively. The corresponding output from the optical intensity correlator is seen in Figure 6.9 c). The output shown is a photograph of the monitor screen and is thus the time-average of several frames. An axonometric plot of this output is shown in Figure 6.9 d) and demonstrates that under these conditions the correlator possesses sufficient discrimination to distinguish the similar letters O and G.

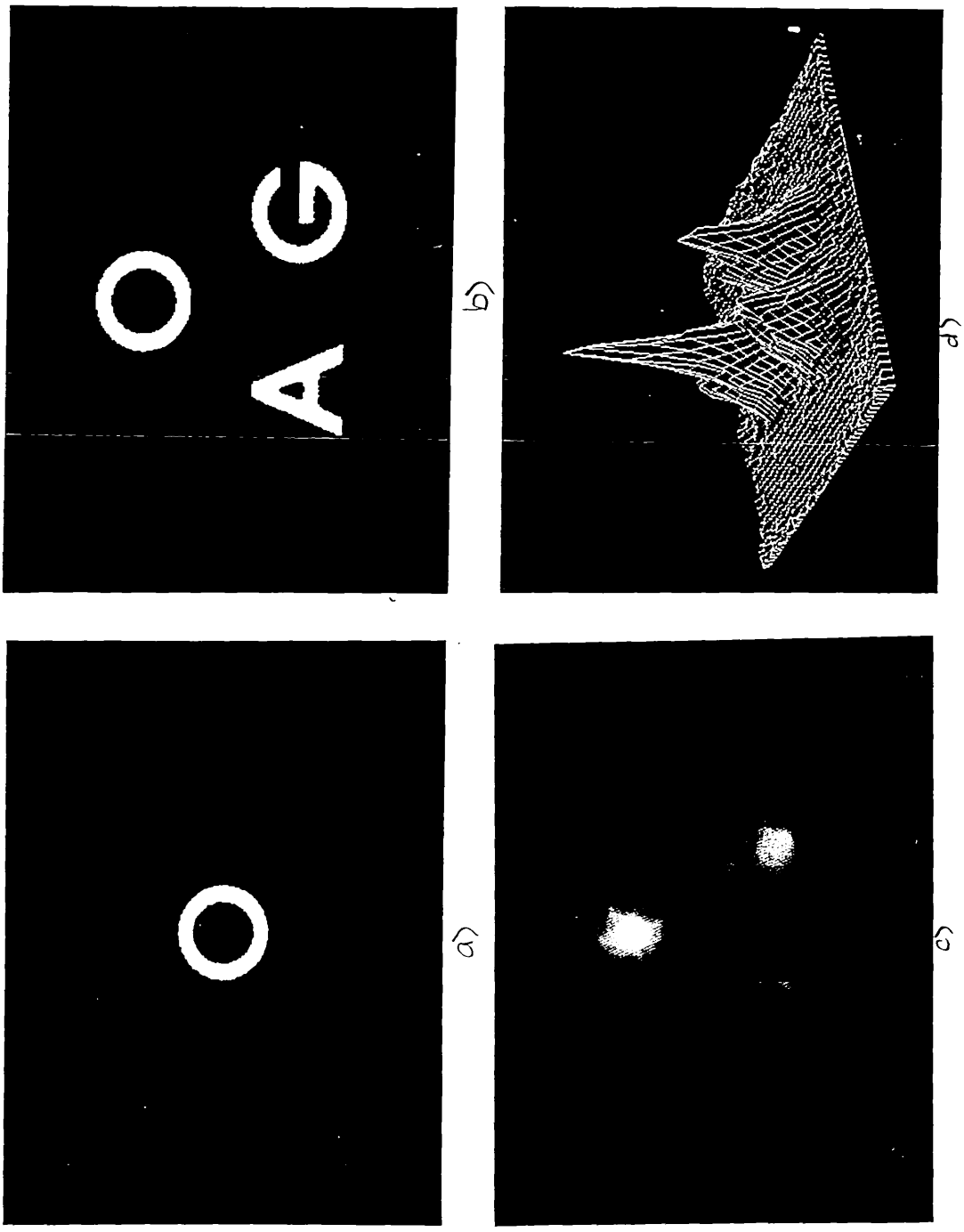

Figure 6.9 Experimental demonstration of the correlator using high contrast photographic transparencies for both inputs 1 and 2; a) input 1, b) input 2, c) corresponding output intensity pattern, and d) axonometric representation of output.

An important advantage of the optical intensity correlator using spatially incoherent readout is that there is little restriction on the

placement of the optical filter. The in-plane movement of a real-time filter, of course, has no effect provided that the beams still overlap in the volume of the crystal. However it was found that the on-axis placement of the BSO crystal in this optical system is greatly relaxed compared to the coherent optical correlator. The correlator was set up as in the above experiment, with the exception that the BSO crystal was mounted on a translation stage to allow axial movement. The crystal could be moved axially through a distance of 2 cm without any significant deterioration of the output intensity pattern (see figure 6.10). This is compared to typical values of d_g and d_g' of between 10 and 15 cm. This increased 'depth of field', compared to a coherent correlator [6.1], suggests that a crystal of longer interaction length, L, could be used as the dynamic medium in the intensity correlator. As the diffraction efficiency of a volume hologram scales as L^2 [3.1], an increase in intensity would be achieved at the output stage. This would improve the signal-to-noise ratio of the correlator, and offer possibilities of operating such a system in low light-level conditions.

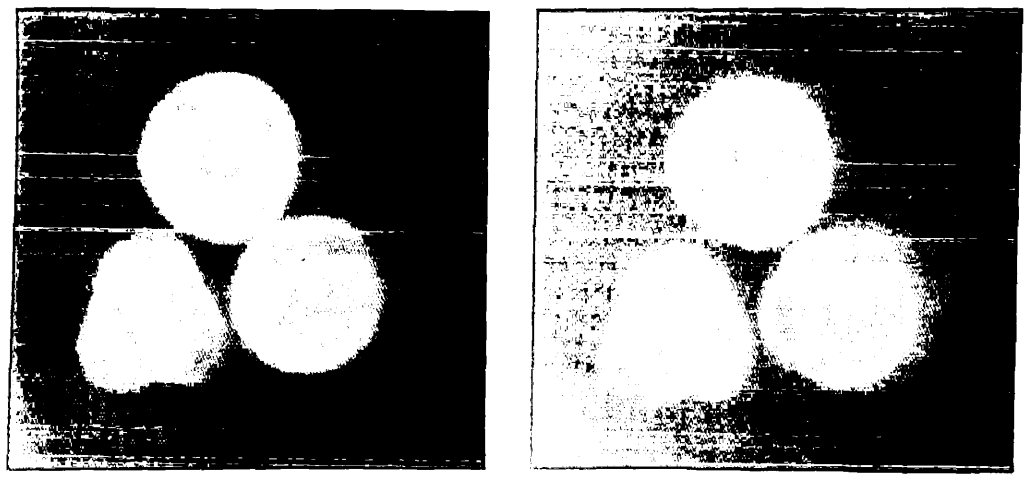

Figure 6.10 Demonstration of the extended 'depth of field' of the intensity correlator. From left to right; a) output intensity pattern when the distances d_g' and d_r' are set according to the ratio of the respective wavelengths, and b) output intensity pattern after the BSO crystal is moved 2 cm towards L2.

It was also found that the position of input 2 could be moved axially and a displacement of almost ± 2 cm had no significant effect on the intensity of the auto-correlation peak (Fig. 6.11). Thus the insertion of an SLM into the system, to act as input 2, can be easily

achieved. The in-plane movement of input 2 is restricted by the Bragg-matching constraint.

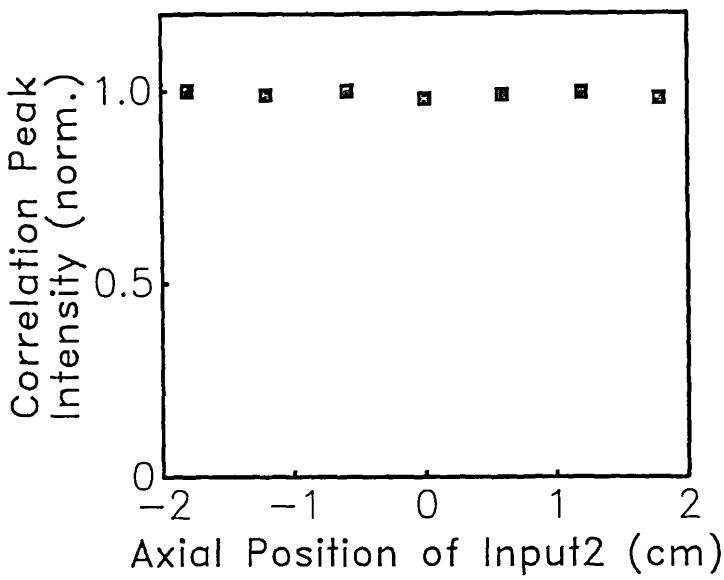

Figure 6.11 Variation of the intensity in the auto-correlation (of the 'O' with the 'O') peak on moving input 2 axially.

The second experiment was conducted using an LCTV as a real-time SLM for input 2. A CITIZEN T530 colour LCTV was used. A monochromatic contrast ratio of 10:1 was obtained on projection of the HeNe laser through the TV screen. Images were obtained on the LCTV screen by connecting to it the video signal from a camera with zoom lens trained on the real objects. The reference object of the correlator was the single letter O to which the letters O,G and A were presented sequentially by placing them in front of the camera. The results are as viewed in Figure 6.12. Note that no attempt was made to compare the absolute intensities at the output plane as the usual fluctuations of the diffraction efficiency of gratings formed in BSO in 'drift-mode' would have precluded comparison. Thus each of the results shown in Figure 6.12 c) has been normalised. The full widths at half maximum (FWHM) of the auto-correlation (of the 'O' with the 'O') and cross correlation (of the 'O' with the 'G') peaks are in the ratio 3 : 4. It is seen that although the discrimination of the correlator is quite low, as expected, it is again sufficient to distinguish between the letters O and G. The lower discrimination of the correlator when using the LCTV

rather than lithographic film as input 2 is almost certainly accounted for by the low resolution and contrast of the LCTV.

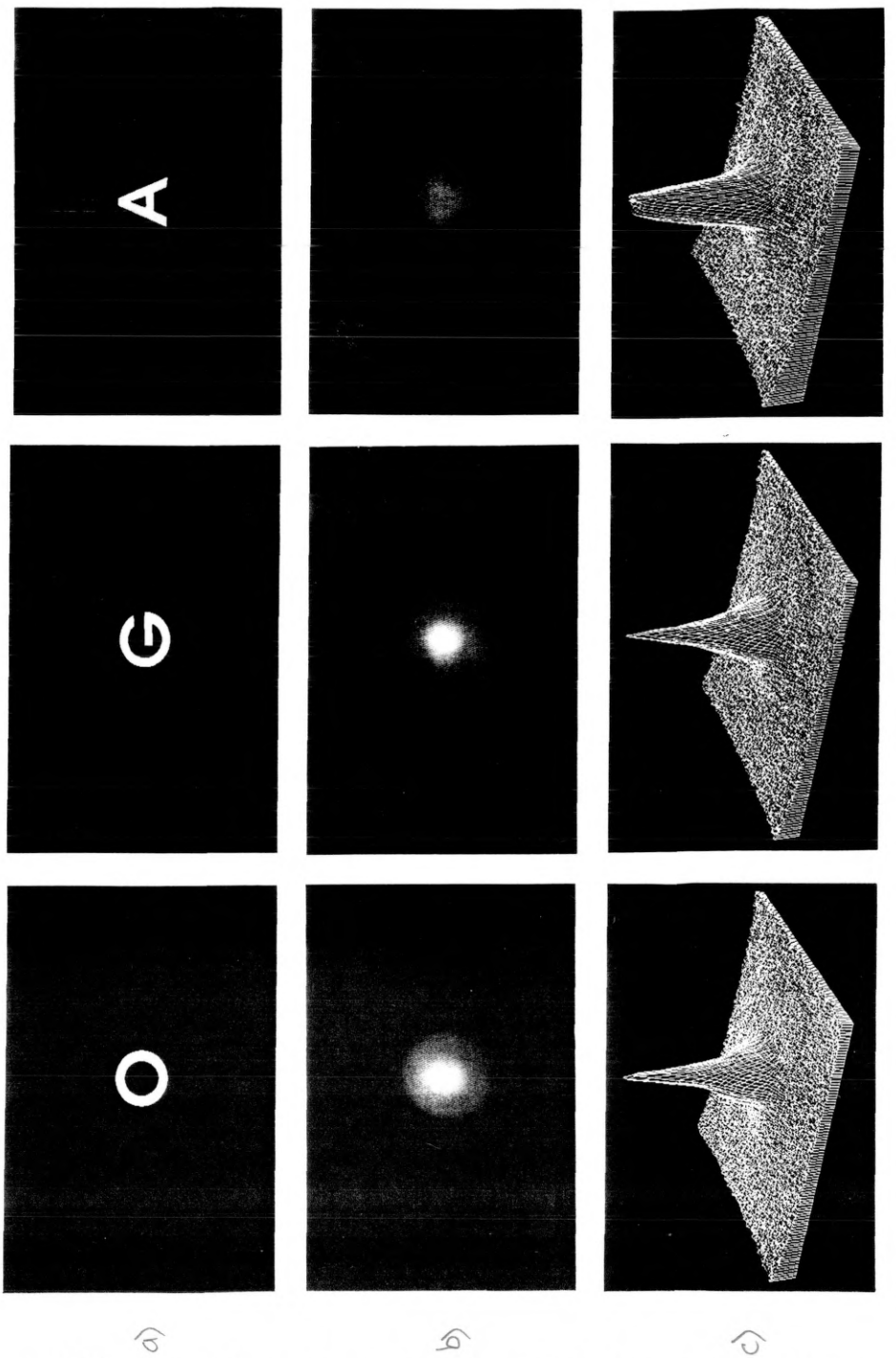

Figure 6.12 Experimental results of optical intensity correlator using the LCTV as a real-time SLM for input 2. The reference object of the correlator was the single letter O to which the letters O,G and A were presented sequentially. From top to bottom; a) input object, b) output plane and c) 3-D representation of the output. The plots shown in c) have been normalised

6.3 Optical Novelty Filter

6.3.1 Introduction

Many industrial, medical and other applications require a reduction of image data to be processed. In a lot of instances this involves removing the recurrent static information of an optical scene, e.g. removal of the background of a cell culture to examine the moving organisms [6.11]. Such an operation has been termed 'image differentiation in time' or 'novelty filtering'. The output of an ideal novelty filter should thus remain blank until a portion of the input scene changes. This moving portion only should then be observed at the output. There have been various successful implementations of all-optical systems to carry out this operation [6.11-6.15].

In this section the operation of novelty filtering is demonstrated using a hybrid system which consists of an optical processor using BSO, with further real-time processing achieved via a PC fitted with a frame-grabber card. As in previous applications, a BSO crystal is used as a dynamic holographic medium within which gratings are written at 514 nm and read out at 633 nm. The transient peak in the diffraction efficiency of a grating formed in 'drift-mode' is enhanced and controlled by the imposition of various extrinsic conditions. It is felt that this particular system has the following inherent advantages: BSO is relatively fast in its response, reliable in its performance and is available with good optical quality over large surface areas; the stationary state output of the system is very stable allowing complete suppression of static information; the temporal duration of response to a step-like change can be controlled to produce re-setting of the optical processor at T.V. frame rates, i.e. the system as a whole is updated at frame rates; good signal-to-noise is achieved through the use of different wavelengths and polarisations to write and read the holographic grating, respectively; the ratio of transient to steady state intensity can be controlled simply by the addition of white light intensity. Temporal discrimination is further improved by digital thresholding with a low-cost PC. The digitised image information at the output of this device may be passed either to another digital system or used to feedback into an optical system for further

processing.

6.3.2 Transient Enhancement under Optical Bias

The device presented here relies upon the transient enhancement of a beam diffracted from a dynamic holographic grating formed in BSO as reported in chapter 5. It was seen that the transient properties of the diffracted beam can be controlled by the level of optical bias. Specifically, the ratio of transient-peak to steady-state diffraction efficiency is determined by the ratio of optical bias to (useful) write beam intensity, while the peak width of the transient peak is determined by the absolute intensity of the optical bias.

Thus the method of introducing incoherent optical bias provides a versatile, (inexpensive) means of controlling the transient properties of a readout beam. A further bonus of the effect for this particular application is that the steady-state diffraction efficiency when under the influence of the optical bias is much more stable than is the case with maximum modulation.

6.3.3 Experimental Configuration

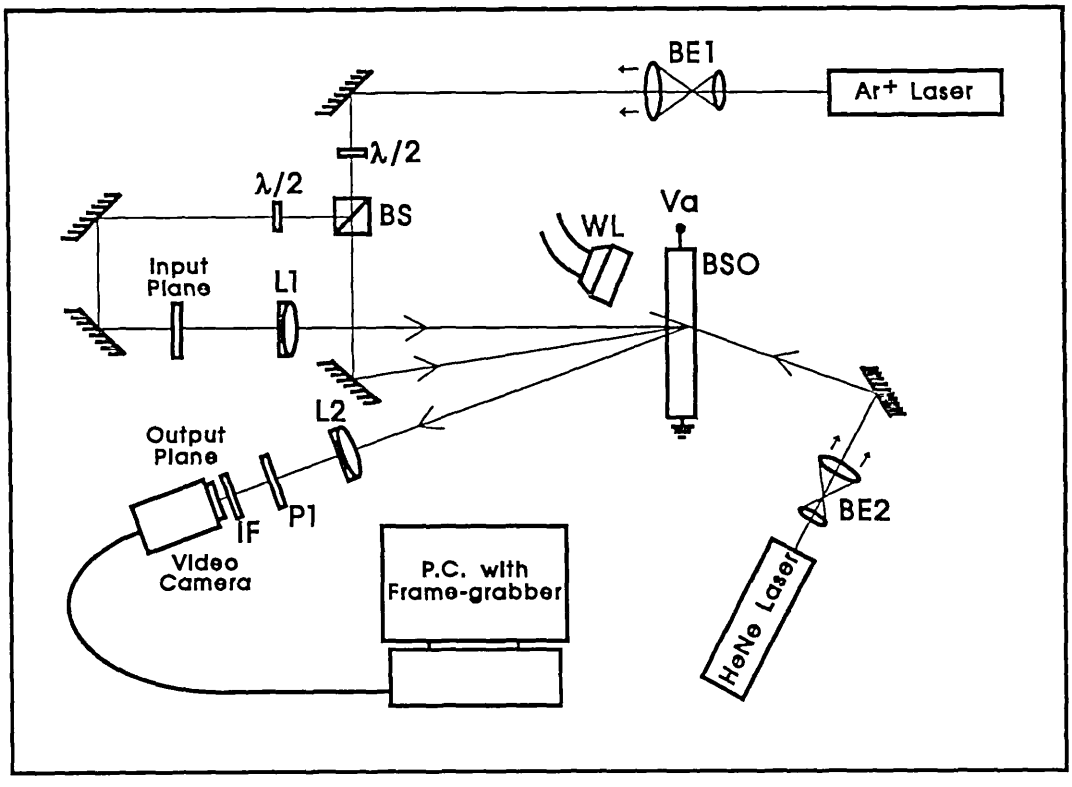

Figure 6.13 Experimental set-up for optical tracking novelty filter. BE1,BE2, beam expanders; λ/2, half-wave plate; BS, beam splitter; L1,L2, 40 cm focal length plano-convex lenses; Va, applied voltage (5kV); WL, white light source; IF, 633 nm interference filter; and P1, polaroid sheet.

The experimental set-up for the novelty filter is shown in Figure 6.13. A BSO crystal of dimensions 10 x 8 x 2 mm^3 supplied by Sumitomo Industries was used. The Ar^+ laser operates in single longitudinal mode and the output beam is spatially filtered and expanded to 15 mm diameter. The beam is then split by a polariser cube and one component passes through the input device which is imaged onto the crystal by L1. The second beam acts as the reference and is directly incident on the crystal to allow formation of the holographic fringes. The spatial period of these fringes, and consequently the grating formed, is 20 μm. This fringe spacing was chosen as it provides a reasonable ratio of transient to steady state intensity (section 5.3.5) and also permits a reasonable field of view of the diffracted image. The grating vector

is parallel to the [110] crystallographic direction. 5kV is applied across the crystal also in this direction to facilitate grating formation at this fringe spacing and to increase the diffraction efficiency of the resulting grating. The white light is fed to the crystal via a fibre optic system with I.R. filter and is incident at an arbitrary angle. Its intensity was adjusted with respect to the Ar^+ intensity to provide a significant transient enhancement. A HeNe beam is expanded to 10 mm diameter and is incident on the crystal at the Bragg angle. The diffracted component is imaged by L2 onto the input face of a video camera. Background noise is considerably reduced by the use of an interference filter and polaroid sheet. The output from the video camera is fed into a PC with a frame-grabber card. This card is used as a real-time thresholding device by the assignment of binary values in a digital look-up table.

The principle of the device is that when the the grating is stationary the diffracted output will be fixed at its stabilised, low intensity steady-state value. When a portion of the input moves then a new grating is continuously formed in the crystal at the spatial location corresponding to the moving region. On formation this grating has the transient enhancement as observed in Figure 5.2 and so the diffracted output will be considerably enhanced in the region of movement. This enhancement is converted into a binary state by the thresholding operation of the frame-grabber. Once the object stops moving the diffracted intensity will once again return to its suppressed steady-state value. Note that the time for this relaxation back to its steady-state value is determined by the intensity of the optical bias. The total Ar^+ laser intensity at the crystal was set to about 2 $mWcm^{-2}$ and the white light intensity to approximately three times this value. On chopping the signal beam, these intensity settings produced a peak to steady-state diffraction efficiency ratio of about 4:1 and a peak width of 20 ms.

6.3.4 Experimental Results

To demonstrate the principle of the novelty filter a USAF test slide was used as the input device and movement was produced manually. To allow quantitative assessment of the system the video camera was

replaced by a photodetector with laser power meter. The object was moved in a step-like manner and its change in position was registered by reflecting a beam from it onto a series of photodetectors. The diffracted intensity and object position were then logged simultaneously using a multi-channel A/D card on a PC and are presented in the upper and lower portions respectively of Figure 6.14. The diffraction efficiency is seen to increase significantly on movement of the object before settling back down to the well regulated steady-state value. Thresholding can be easily set at a value between the peak and steady-state level. Thus time differentiation is achieved and a novelty filter may be implemented.

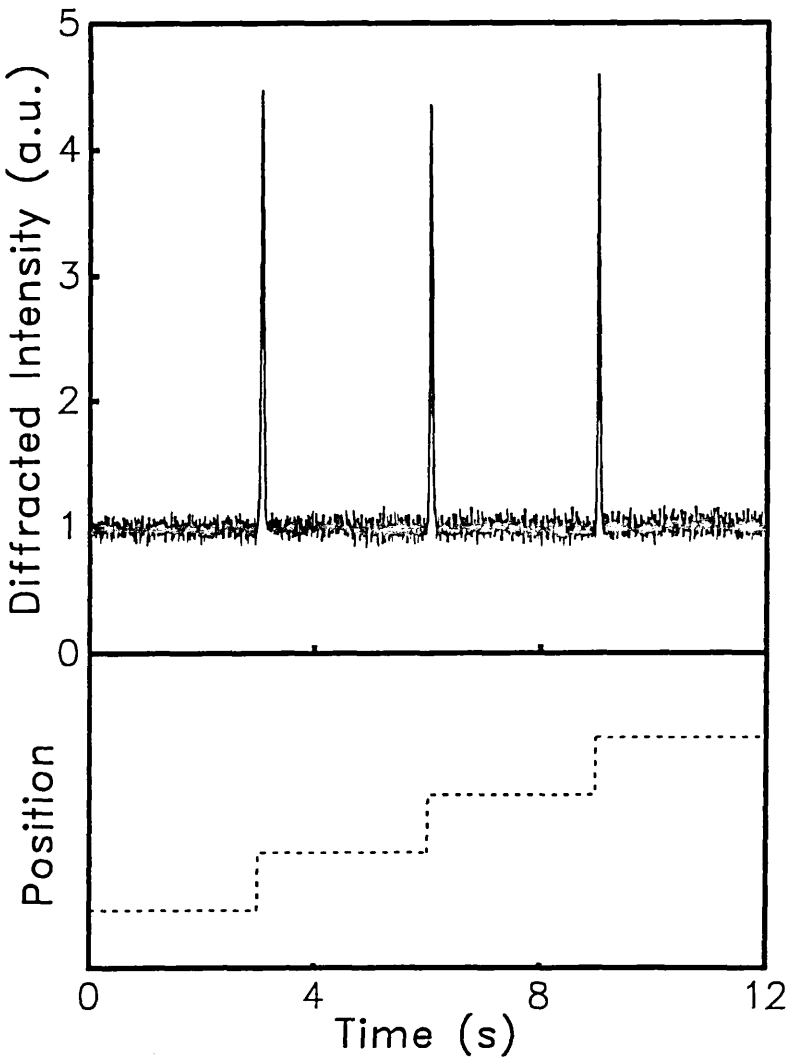

Figure 6.14 Output diffracted intensity detected by a single element photodetector at the position of the output plane. The position of the object was registered by reflecting a beam from it onto a secondary series of photodetectors.

Figure 6.15 shows the behaviour of the device when the video camera is returned to the system. In Fig. 6.15 a) the object is shown under normal static, optimum modulation conditions with the image having been binarised with the frame-grabber device. When the object is moved under these conditions the re-formation of the grating follows an exponential growth curve with a purely real time constant as in Figure 5.2 a). Fig. 6.15 b) shows the static conditions after the optical bias has been introduced. For the purposes of this demonstration the threshold value has been set deliberately low allowing some of the input image to be visible even when static; complete elimination of the background intensity under stationary conditions is easily obtained. Fig. 6.15 c) shows the output whilst the test slide is in motion; most of the input plane is again visible in reasonable detail. Once the slide stops moving the output returns to the state seen in Fig 6.15 b). Clearly, under these conditions, the output plane is significantly enhanced only when the object is in motion.

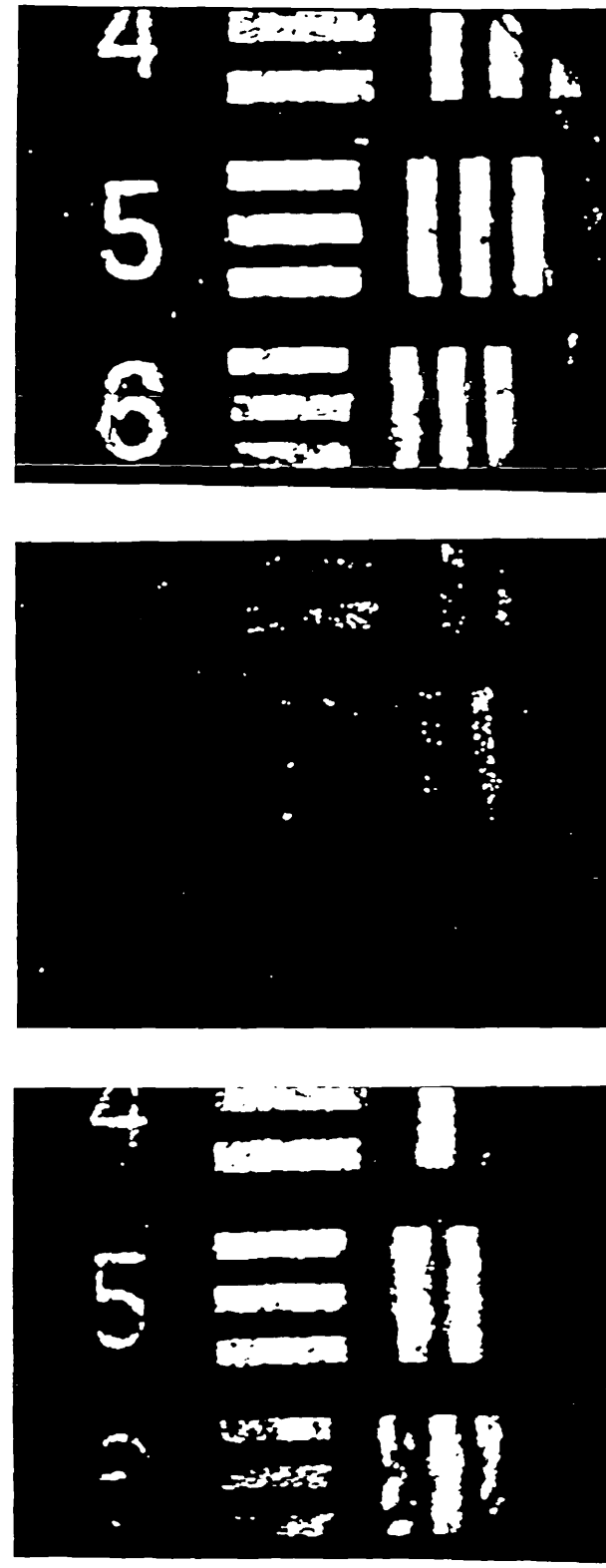

Figure 6.15 Output plane with video camera in position. a) normal static binarised image with optimum modulation; b) static object when white light is introduced; c) object in motion under the same conditions as in b).

6.4 A Motion-Sensitive Optical Intensity Correlator

In this section details are presented of an optical processor which carries out the dual operation of character recognition and temporal differentiation. This is achieved by integrating into the intensity correlator system described in section 6.2, the transient enhancement techniques implemented in the preceding section. As before, dynamic Fresnel holographic filters are written in photorefractive $Bi_{12}SiO_{20}$ at 514 nm and read out using spatially incoherent illumination at 633 nm. The transient enhancement of the readout beam is achieved by the use of optical bias under the necessary conditions. Temporal discrimination is again further improved by digital thresholding. Thus, a threshold is set such that not only will a specific object be distinguished by the device, but it will only be apparent at the output stage when it is moving. The overall system operates at T.V. frame rates.

6.4.1 Experimental Arrangement

Due to the simplicity of the transient enhancement described in section 6.3, it can easily be incorporated into the system used to carry out the optical intensity correlation operation. Therefore, the experimental system used for this application is the same as that for the intensity correlator, shown in Figure 6.8, with the exception of the addition of a white light source. The white light is fed to the crystal via a fibre-optic bundle with an I.R. filter and is incident at an arbitrary angle. The total Ar^+ laser intensity at the crystal is set to about 4 $mWcm^{-2}$ and the white light intensity to approximately equal this value. On chopping the signal beam, these settings produced a peak-to-steady-state diffraction efficiency ratio of around 1.5:1 and a peak width of 20 ms (Figure 6.16).

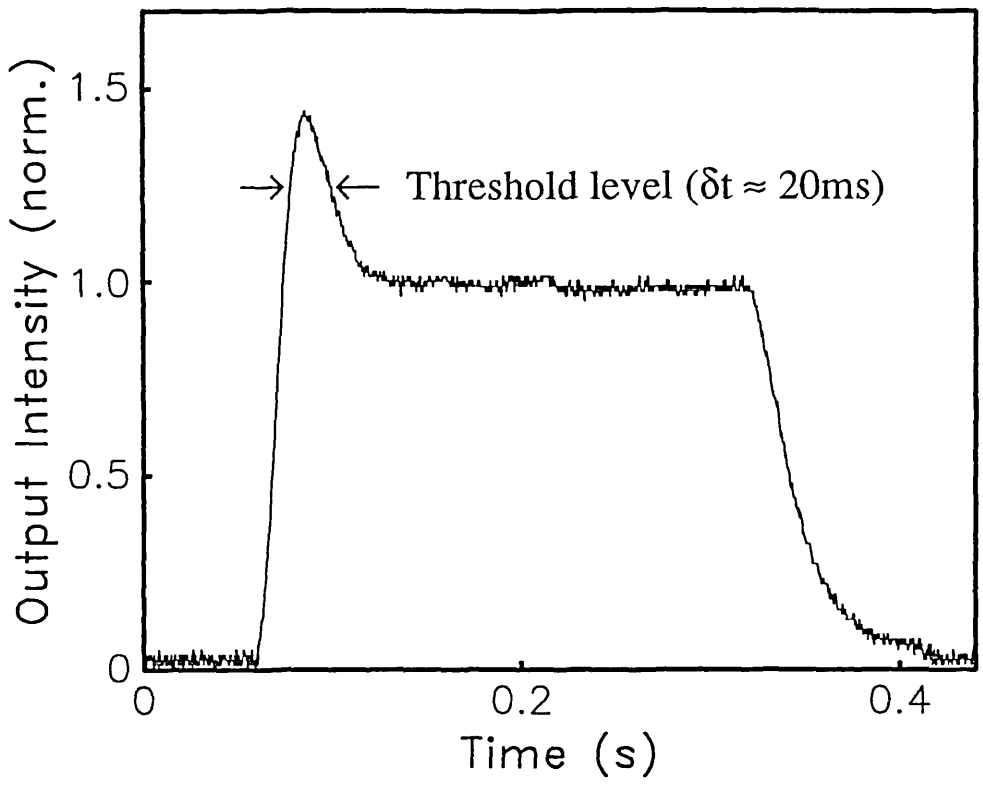

Figure 6.16 Variation of the diffracted intensity at the output plane, as measured using a single element photo-detector. To obtain this plot the beam illuminating input 1 was chopped at the mutual focal plane of a two-lens system.

6.4.2 Results

Experimental demonstration of the intensity correlator with temporal differentiation was carried out using the same objects as shown in Figure 6.9 a) and b).

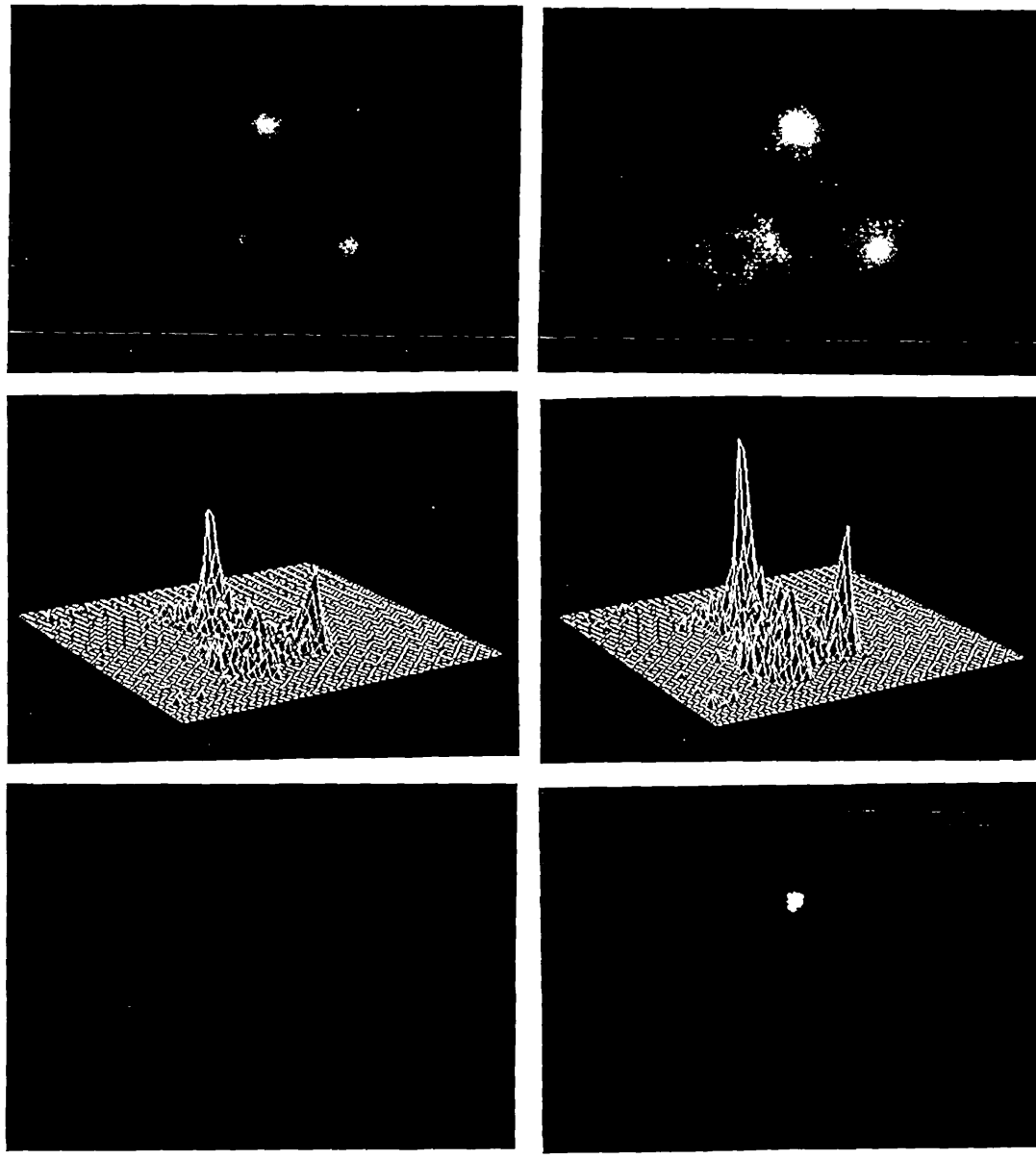

Figure 6.17 Demonstration of the dual temporal and character discrimination of the device, using the same input objects as shown in Figure 6.9. Left column; input 1 static. Right column; input 1 moving. From top to bottom; a) variation of the output intensity plane, demonstrating the transient enhancement b) axonometric plot of the output intensity to illustrate that relative intensities are maintained, and so the correlator can still distinguish between the characters, and c) the output after digital thresholding has been implemented. Note that, under these conditions, the auto-correlation of the 'O' with the 'O' is only registered at the output stage when in motion.

The introduction of the white light, of course, causes a uniform decrease in the output intensity pattern. Thus, when the input to the system (input 1) is stationary, the diffraction efficiency is at a stabilised, low-intensity steady-state value. When the input moves however, a new grating will be formed, which initially has the transient enhancement, as observed in Figure 6.17 a).

As each of the constituents of the output plane is the cross-correlation of input 2 with input 1, each of the cross-correlations is enhanced by the same factor; i.e. the same relative intensities are maintained throughout the output plane. Therefore the correlator maintains the ability to discriminate between the input objects. This point is illustrated in Figure 6.17 b) by 3-dimensional plots of the above intensity patterns.

The transient enhancement is converted into a binary state by the thresholding operation of the frame-grabber (see Figure 6.17 c). Note that complete suppression of the output is obtained in the steady state, and that only the correlation spot corresponding to the auto-correlation of the 'O' with the 'O' is visible when the input is moving. Thus the letter 'O' is recognised by the system, but is only registered at the output stage when moving. Once the object stops moving the diffracted intensity will again return to its lower steady-state value, and so the output is suppressed by the digital thresholding. The time for this relaxation back to the steady-state value is determined by the intensity of the optical bias (section 5.3.4).

Chapter Seven
Conclusions and Further Work

It has been demonstrated in this thesis that photorefractive BSO can be used as a dynamic holographic medium to implement image processing operations such as novelty filtering and optical correlation.

The novelty filter that was demonstrated exhibited good temporal discrimination, through the use of digital thresholding and careful optimisation of the optical system. The optical configuration of the novelty filter achieved a good transient-to-steady-state ratio without having to resort to readout of the higher order harmonic gratings, as was necessary with other configurations [7.1]. This alleviates the associated problems of phase-matching, limited resolution (an order of magnitude lower) and lower diffraction efficiency of the higher order grating. Also, the use of digital thresholding, whilst forfeiting the possibility of selective velocity filtering, produces complete suppression of the object below a certain speed threshold.

Optical correlation was implemented initially using a coherent optical system in the joint-transform configuration. Although this correlator produced good results its construction was hindered, as with other coherent correlators, with the small positional tolerance of these coherent systems. Also, an attempt to utilise a low-cost liquid crystal television (LCTV) as a crude spatial light modulator was unsuccessful. It is believed that the reasons for this were the optical phase inhomogeneities, due to the transparent electrodes and the liquid crystal molecular distribution, and the poor contrast of the LCTV.

Most of these practical problems were overcome in the intensity correlator because it uses spatially incoherent light to read out the holographic filter. Certainly, the positional tolerance was significantly improved, and this was demonstrated with experimental results. Also, the phase inhomogeneities of the LCTV cannot be relayed to the output stage of the intensity correlator by the spatially incoherent light.

The main disadvantage of the intensity correlator is its poor discrimination ability, as compared with its coherent counterpart. It is well known that the discrimination ability of an optical correlator is dependent only on the high spatial frequency content of the input objects. Therefore it is expected that edge enhancement, or the suppression of the low spatial frequency content, will enhance the discrimination ability of the intensity correlator. Edge enhancement can be achieved for both of the input objects of the intensity correlator; the signal on the LCTV by computer pre-processing, and the input signal in the write-beam by using the non-linear recording technique presented in section 4.7. To date, attempts to improve the discrimination of the correlator using these techniques have been unsuccessful. One of the main problems of this was the limited resolution of the LCTV. This has recently been overcome by the use of an imaging system to allow the use of a larger portion of the LCTV screen and thus achieve better resolution. Thus, an intensity correlator with improved discrimination, achieved by edge enhancement, will be the subject of future work.

An improvement to the optical processor presented in chapter 6 which achieved temporal discrimination and optical correlation simultaneously, would be to increase the level of output intensity. The problem with this device is that the output intensity of the intensity correlator is initially very low, due to a limited fraction of the beam power being able to Bragg-match to the volume grating, as the light is very divergent following propagation through the rotating diffuser. Therefore, the addition of white light has to be limited, otherwise the output image will not be registered on the output video camera. As the ratio of optical bias to write-beam intensity will therefore be quite low, the transient-to-steady-state ratio will also be low; i.e. the transient enhancement achieved is not as satisfactory as it was for the case of the novelty filter.

There are several steps which can be taken to improve this situation.

1) The use of a higher power HeNe laser to read the filter.
2) The application of a higher electric field.
3) The use of a PR crystal with a larger electro-optic coefficient.

Clearly the use of a higher power HeNe laser is the simplest solution. Unfortunately, such a laser was not easily obtainable during the course of this thesis, but it is hoped that at some time in the future this experiment will be completed.

The application of higher electric fields (> 6 kV) is not particularly desirable as the crystal would have to be inserted into a liquid gate containing an insulating medium to avoid damage to the crystal by surface currents. An attempt to artificially increase the local electric field by the use of 'structured' illumination such as that used in reference [7.2] was unsuccessful. In this technique a mask was positioned in the white light beam so that the illumination in the centre of the crystal was about a factor of three less than that towards the electrodes. Thus, a significant portion of the applied field should be dropped over the lower conductivity portion (i.e. the central portion) of the crystal. Although photoconductive enhancement was obtained in the output image as expected, there did not remain a sufficient intensity of white light in the central portion (where the actual correlation took place) to produce significant transient enhancement.

It is not known whether the transient enhancement achieved in BSO would be applicable to other PR materials. It is intended therefore, on a more general level, to conduct a study into the transient properties of other crystals, such as strontium barium niobate. Since these crystals possess larger electro-optic coefficients, the attendant drop in the diffraction efficiency caused by the addition of optical bias, would not be such a problem as with BSO, and therefore greater transient enhancements could be obtained without loss of the output image. This may lead to the implementation of transient devices with both a reasonable level of output and controllable transient properties.

It is clear from chapter 5 that there remains much work to be carried out to elucidate the results obtained with optical bias, and to develop a theory which accommodates both this work and that previously reported on TET. The suitability of a two-species carrier and/or charge hopping models to account for these results, is currently being assessed.

It is believed that in the search for a theoretical explanation of the effect of optical bias, the results contained in Appendix B will be highly significant. The behaviour of the transient photocurrent in relation to the diffraction efficiency is most interesting, and it is believed that this does not conform to the band transport model. The variation of the photocurrent decay on formation of the grating as a function of fringe spacing should yield much information. It is intended to conduct this experiment, once a thorough understanding of the rate equations is obtained, in order that an experimental procedure can be formulated.

Appendix A

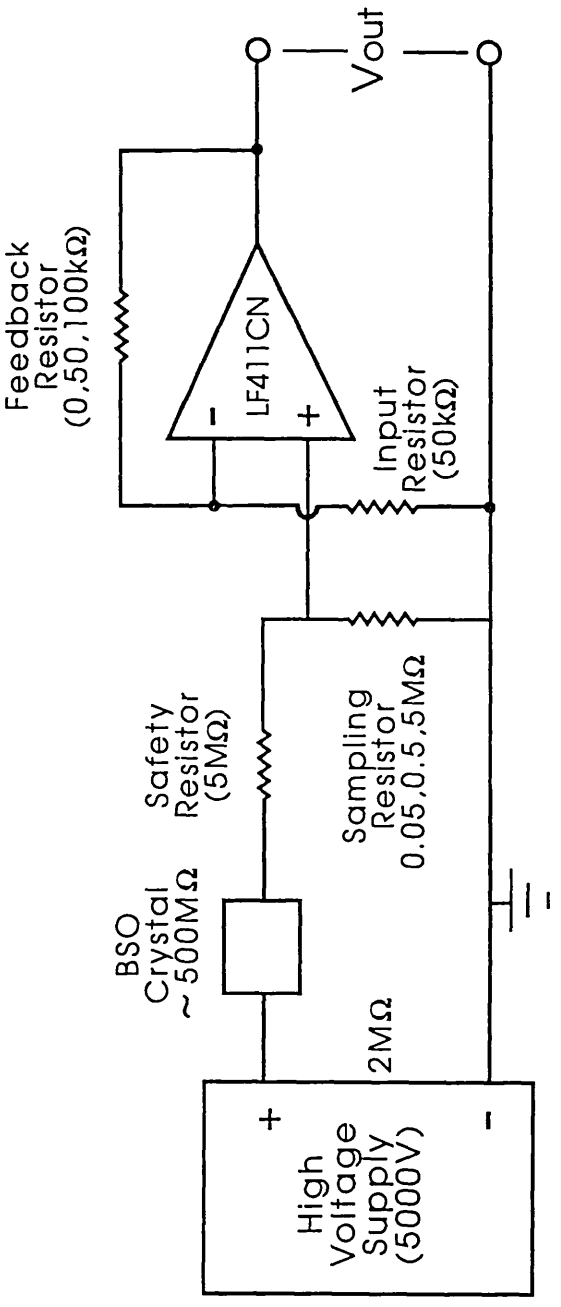

Schematic diagram of the electronic circuit used as a current-to-voltage converter to measure the transient photocurrent.

Appendix B

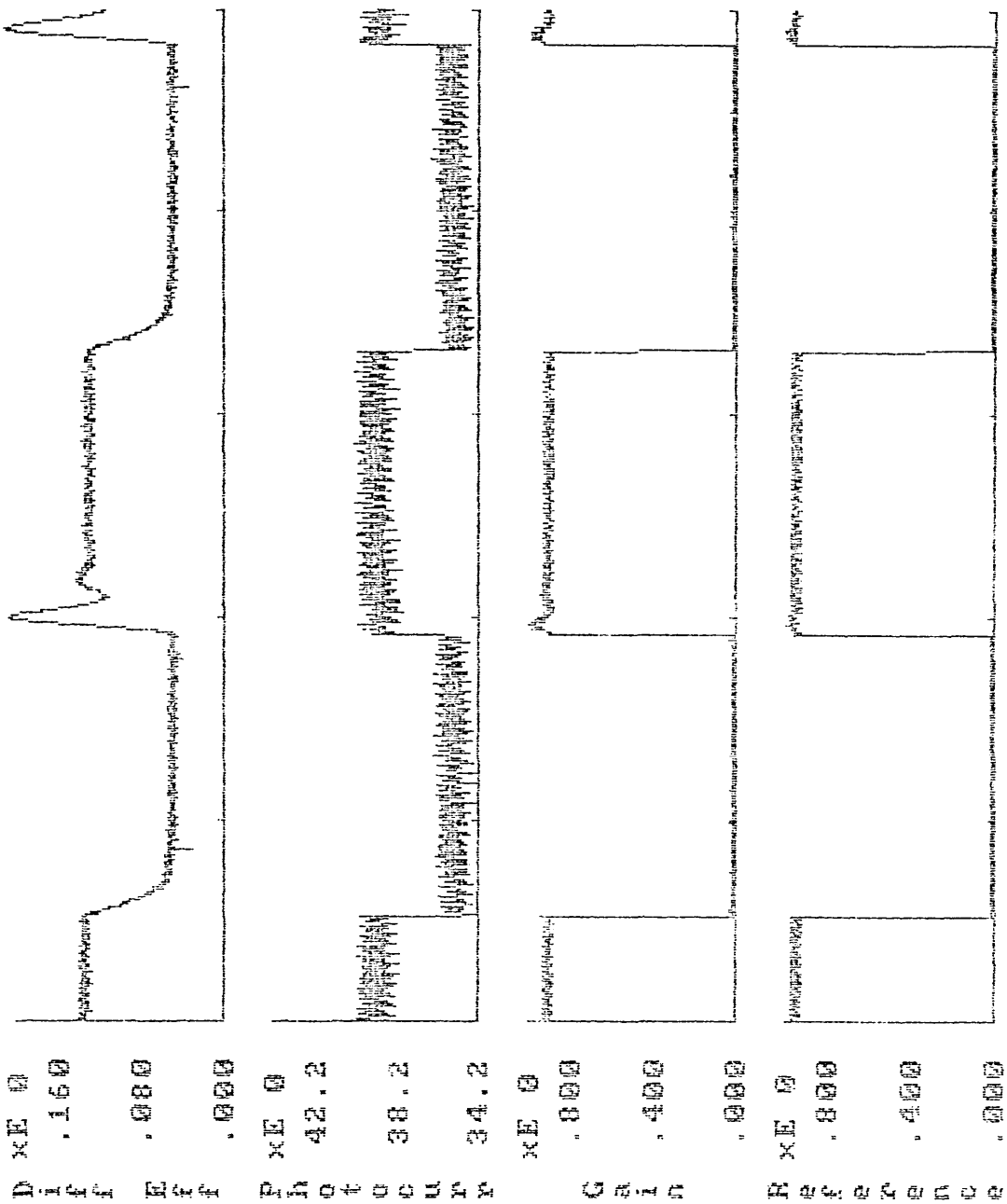

Experimental plot of transient diffraction efficiency, photocurrent, energy transfer and the reference signal. The conditions for this plot were m = 0.2, Λ = 20 μm, E_o = 6 kV/cm and write-beam polarisation parallel.

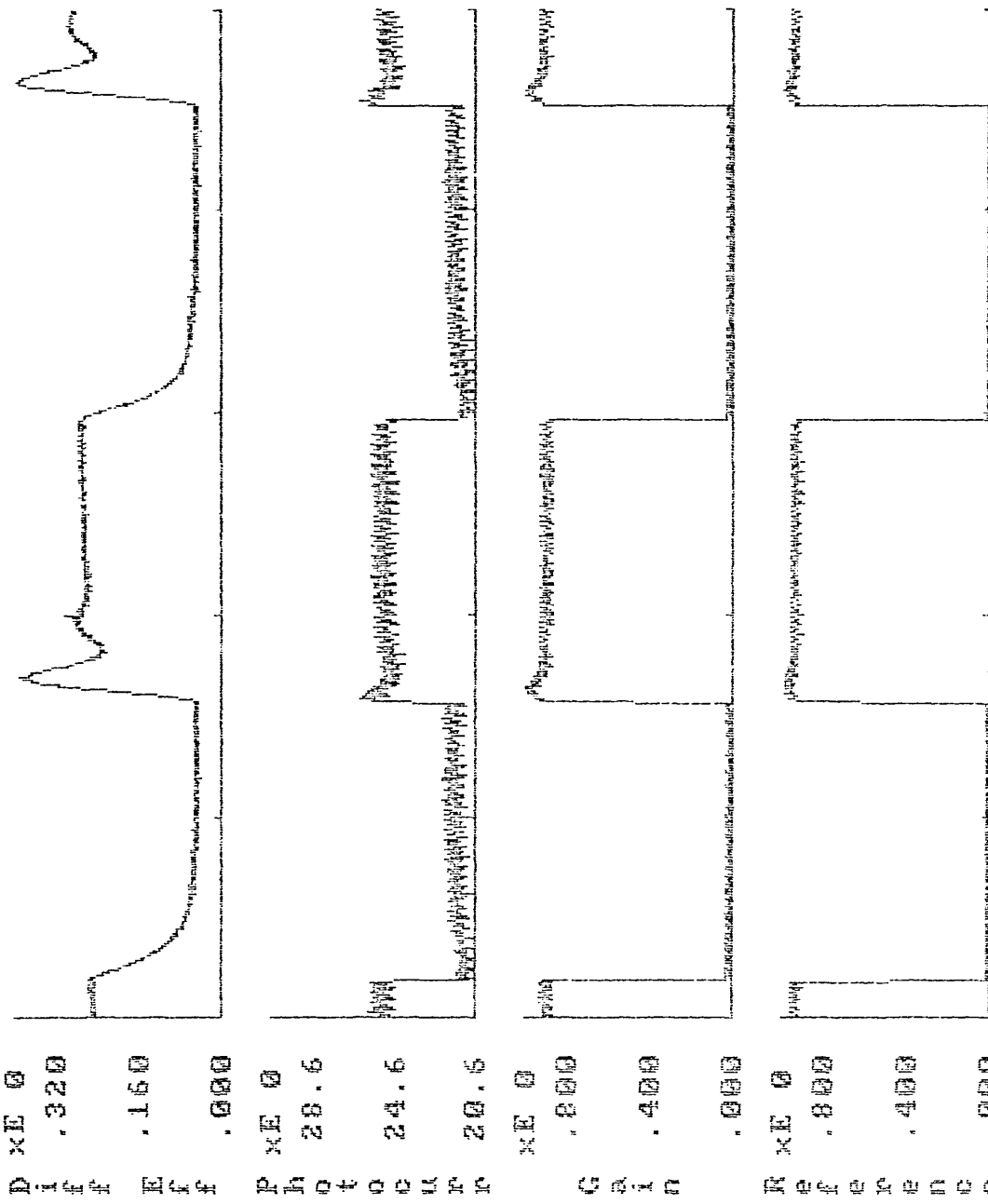

Experimental plot of transient diffraction efficiency, photocurrent, energy transfer and the reference signal. The conditions for this plot were m = 0.4, Λ = 20 μm, E_o = 6 kV/cm and write-beam polarisation parallel.

Appendix B

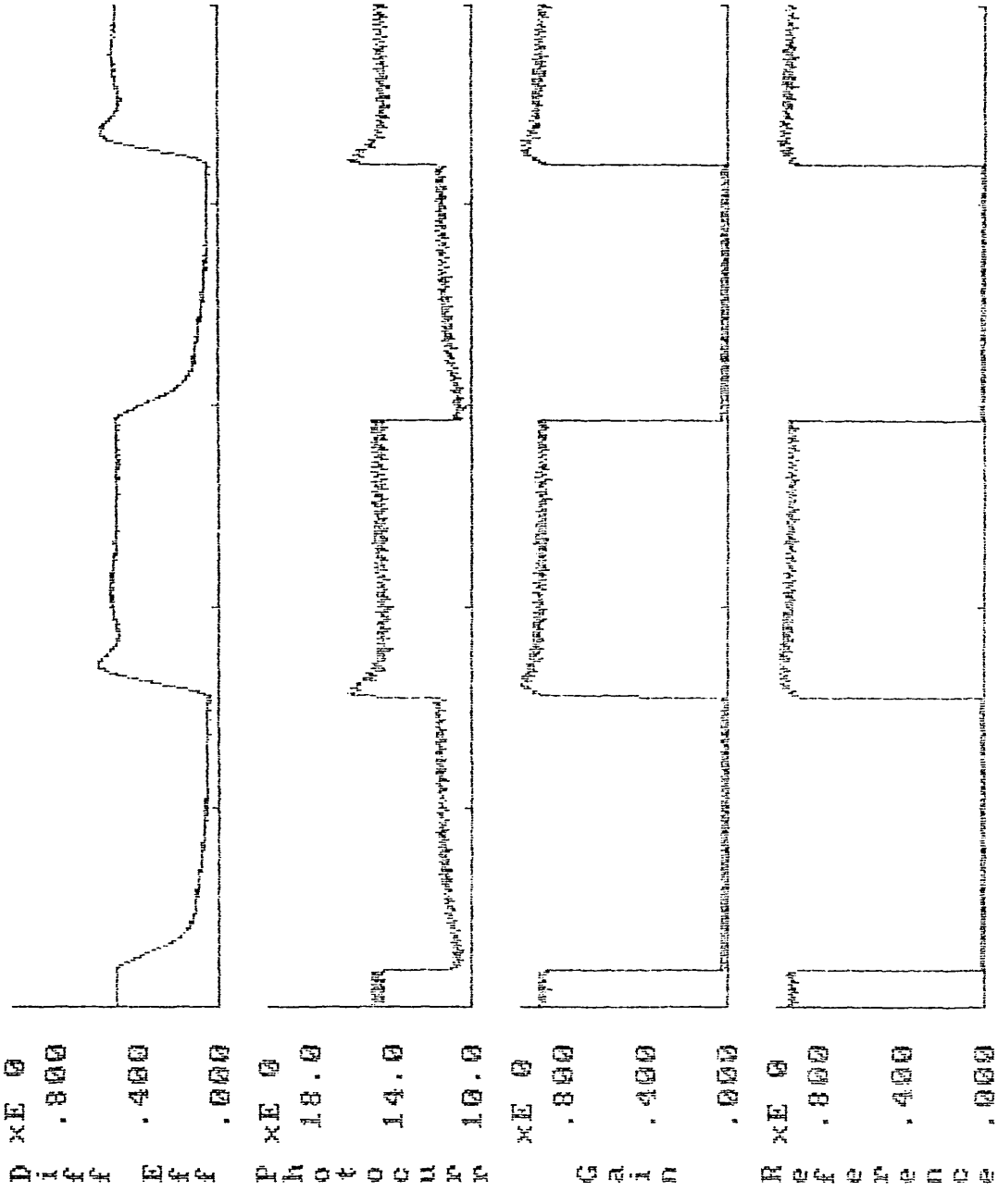

Experimental plot of transient diffraction efficiency, photocurrent, energy transfer and the reference signal. The conditions for this plot were m = 0.6, Λ = 20 μm, E_o = 6 kV/cm and write-beam polarisation parallel.

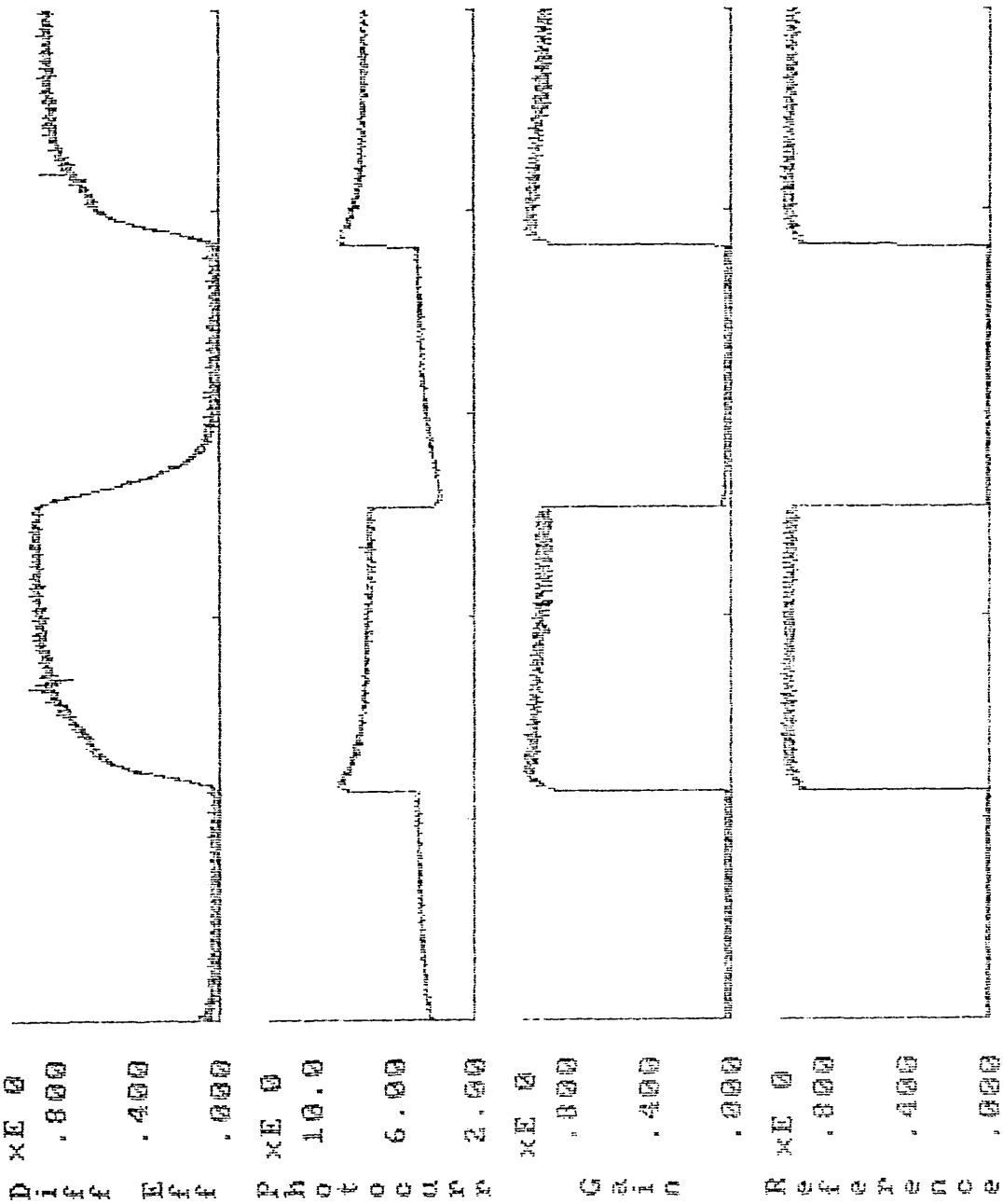

Experimental plot of transient diffraction efficiency, photocurrent, energy transfer and the reference signal. The conditions for this plot were m = 1.0, Λ = 20 μm, E_o = 6 kV/cm and write-beam polarisation parallel.

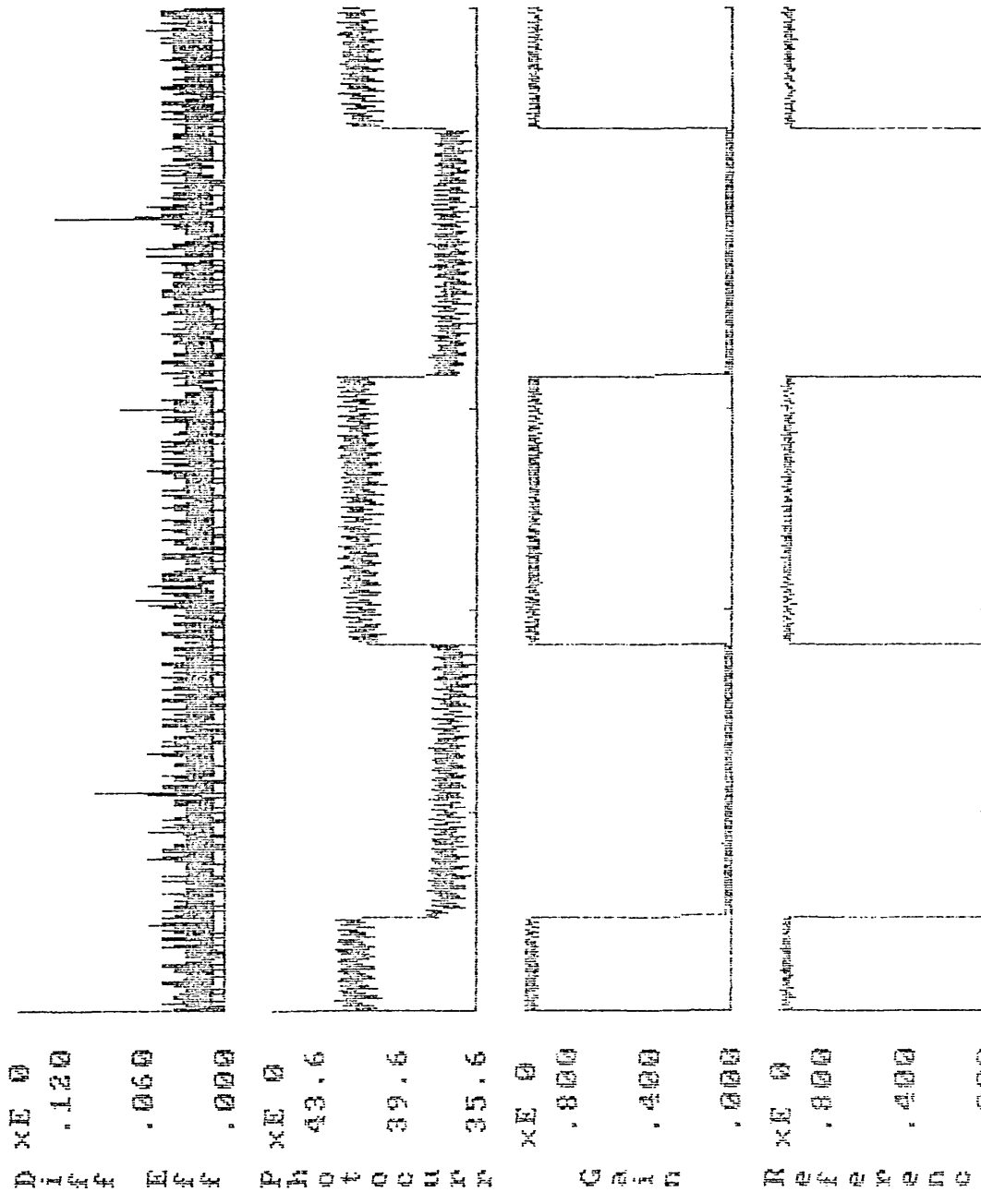

Experimental plot of transient diffraction efficiency, photocurrent, energy transfer and the reference signal. The conditions for this plot were m = 0.2, Λ = 20 μm, E_0 = 6 kV/cm and write-beam polarisation perpendicular.

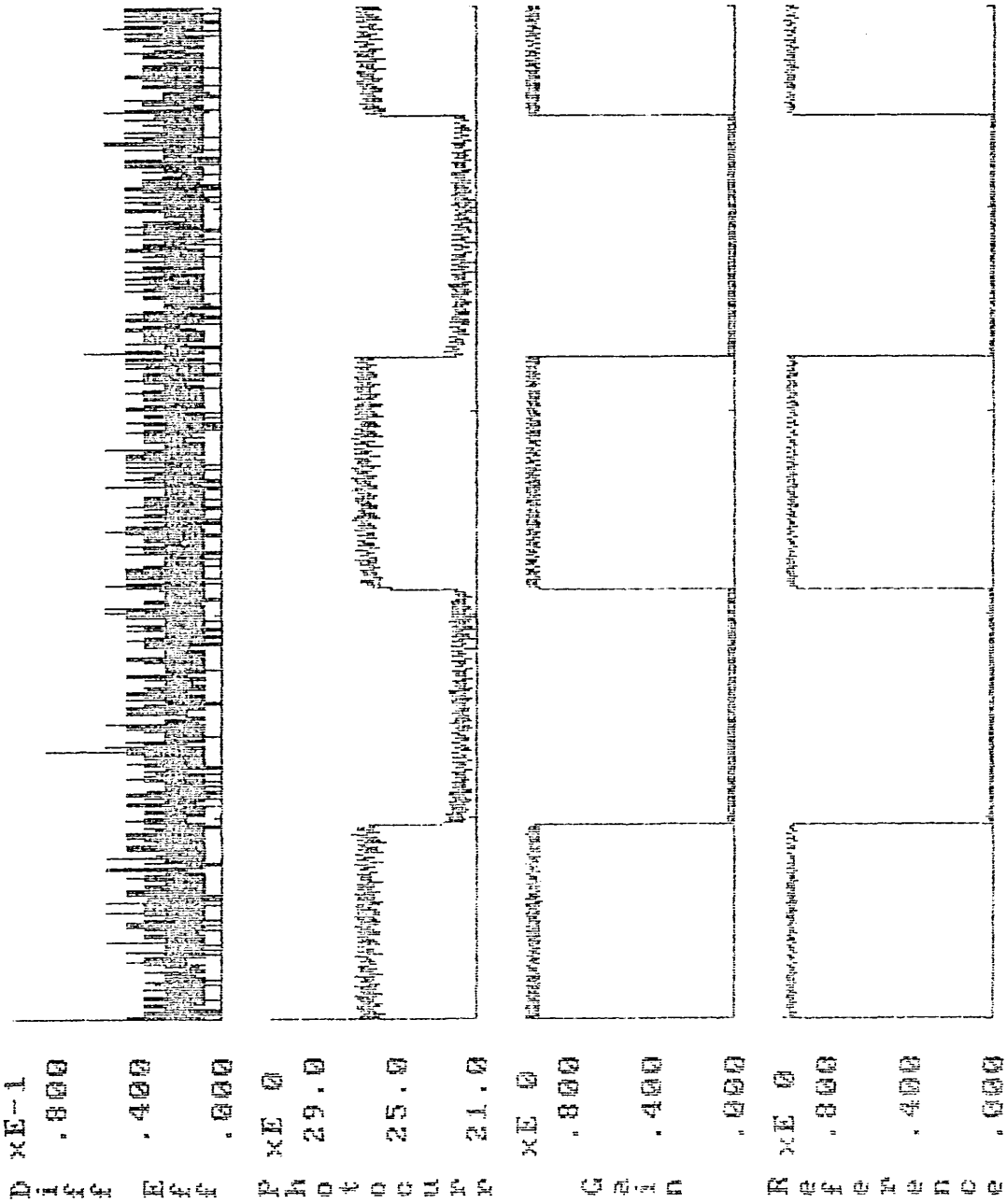

Experimental plot of transient diffraction efficiency, photocurrent, energy transfer and the reference signal. The conditions for this plot were m = 0.4, Λ = 20 μm, E_o = 6 kV/cm and write-beam polarisation perpendicular.

Appendix B

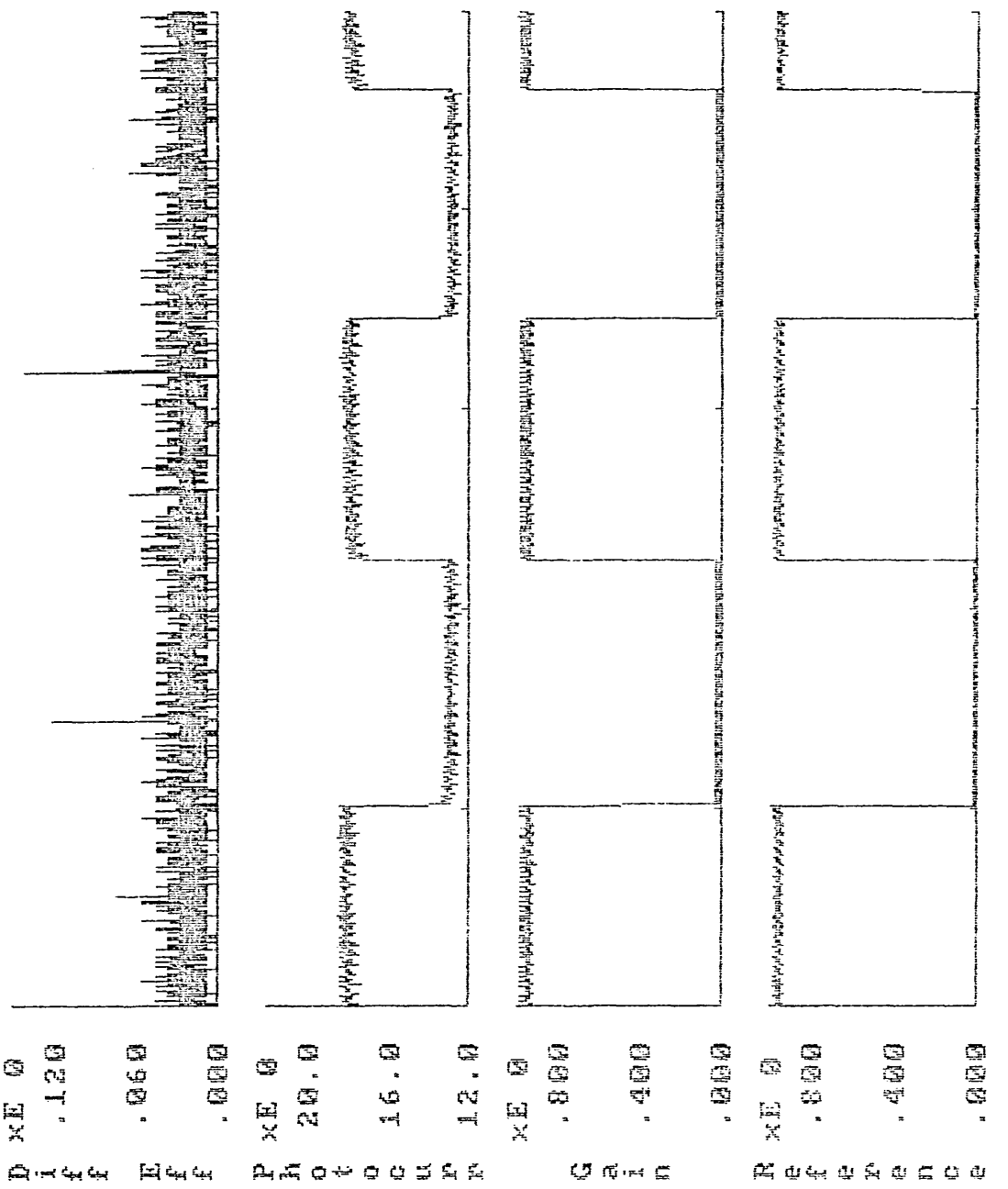

Experimental plot of transient diffraction efficiency, photocurrent, energy transfer and the reference signal. The conditions for this plot were m = 0.6, Λ = 20 μm, E_o = 6 kV/cm and write-beam polarisation perpendicular.

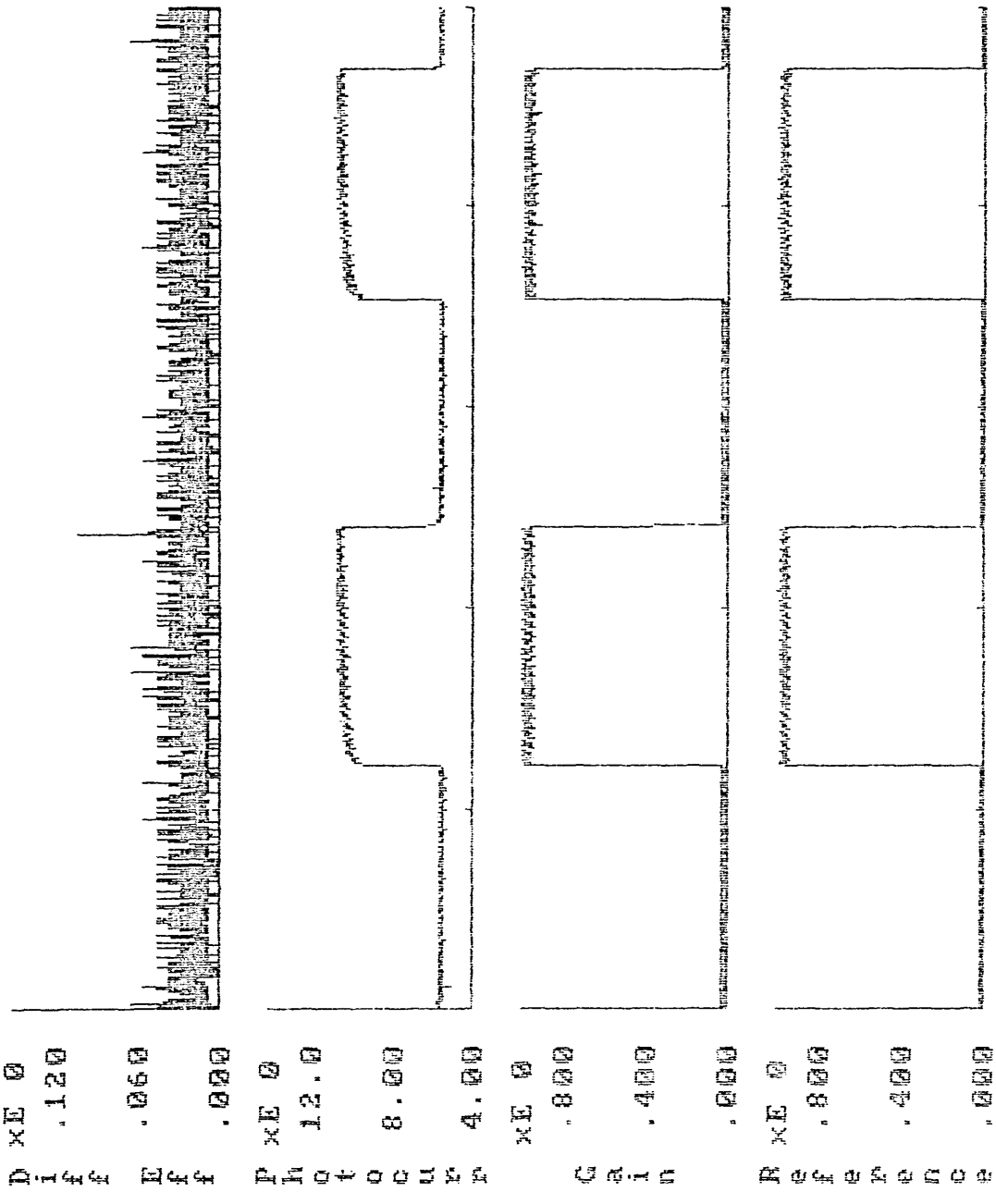

Experimental plot of transient diffraction efficiency, photocurrent, energy transfer and the reference signal. The conditions for this plot were m = 1.0, Λ = 20 μm, E_o = 6 kV/cm and write-beam polarisation perpendicular.

Appendix C

Publications

The following publications and conference presentations were based on the work presented in this thesis.

C. Soutar, C.M. Cartwright, W.A. Gillespie and Z.Q. Wang, "Tracking Novelty Filter using Transient Enhancement of Gratings in Photorefractive BSO," *Opt. Comm.* **86,** 255 (1991)

C. Soutar, Z.Q. Wang, C.M. Cartwright and W.A. Gillespie, "Real-Time Optical Intensity Correlator using Photorefractive BSO and a Liquid Crystal Television," *J. of Mod. Opt.* (accepted, October 1991)

C. Soutar, W.A. Gillespie and C.M. Cartwright, "The Effect of Optical Bias on Grating Formation Dynamics in Photorefractive BSO," *Opt. Comm.* (accepted, February 1992)

C. Soutar, Z.Q. Wang, W.A. Gillespie and C.M. Cartwright, "A Novelty-Filtered Optical Intensity Correlator using Photorefractive BSO," *J. Opt. Soc. Am. B.* (submitted, October 1991)

Conference Presentations

C. Soutar, "Applications of Photorefractive BSO in Phase Conjugate Interferometry," Rank Prize Funds Symposium on Non-Linear Optical Phase Conjugation, Broadway, England, Sept 1989.

C. Soutar, Z.Q. Wang, C.M. Cartwright and W.A. Gillespie, "Real-Time Optical Intensity Correlator using Photorefractive BSO and a Liquid Crystal Television," OSA Topical Meeting on Photorefractive Materials Effects and Devices, Beverly, Massachusetts, July, 1991.

C. Soutar, C.M. Cartwright, W.A. Gillespie and Z.Q. Wang, "Tracking Novelty Filter using Transient Enhancement of Gratings in Photorefractive BSO," EQEC91/QE10 Heriot-Watt Univ., Edinburgh, U.K., August, 1991.

References

2.1 A. Yariv, "Four wave nonlinear optical mixing as real time holography," *Opt. Comm.* **25,** 23 (1978)

2.2 N.V. Kukhtarev, V.B. Markov, S.G. Odulov and V.L. Vinetskii, "Holographic storage in electrooptic crystals," *Ferroelectrics* **22,** 949 (1979)

2.3 J. Feinberg, D. Heiman, A.R. Tanguay and R.W. Hellwarth, "Photorefractive effects and light-induced charge migration in barium titanate," *J. Appl. Phys.* **51,** 1297 (1980)

2.4 T.J. Hall, R. Jaura, L.M. Conners and P.D. Foote, "The Photorefractive Effect - A Review," *Prog. Quant. Electr.* **10,** 77 (1985)

2.5 H.M. Rosenberg; The Solid State (Clarendon Press, Oxford, 1978)

2.6 F.P. Strohkendl, J.M.C. Jonathon, and R.W. Hellwarth, "Hole-electron competition in photorefractive gratings," *Opt. Lett.* **11,** 312 (1986)

2.7 S.I. Stepanov and M.P. Petrov, "Nonstationary holographic recording for efficient amplification and phase conjugation," *Topics in Appl. Phys.* **61,** 263 (1988)

2.8 M.P. Petrov, S.I. Stepanov and A.V. Khomenko; Photosensitive Electro-Optic Media in Holography and Optical Information Processing (Nauka, Leningrad 1983)

2.9 S.G. Lipson and P. Nisenson, "Imaging characteristics of the Itek PROM," *Appl. Opt.* **13,** 2052 (1974)

2.10 E.G. Spencer, P.V. Lenzo and A.A. Ballman, "Dielectric materials for electrooptic, elastooptic and ultrasonic device applications," *Proc. of the IEEE* **55,** 2074 (1967)

2.11 E.L. Venturini, E.G. Spencer and A.A. Ballman, "Elasto-optic properties of $Bi_{12}GeO_{20}$, $Bi_{12}SiO_{20}$, and $Sr_xBa_{1-x}Nb_2O_6$," *J. of Appl. Phys.* **40,** 1622 (1969)

2.12 T.S. Narasimhamurty; Photoelastic and Electro-Optic Properties of Crystals (Plenum Press, New York 1981)

2.13 P. Günter, "Holography, coherent light amplification and optical phase conjugation with photorefractive materials," *Phys. Reports* **93,** 199 (1982)

2.14 P. Günter, "Transient energy transfer between writing beams during hologram formation in $Bi_{12}GeO_{20}$," *Opt. Comm.* **41,** 83 (1982)

2.15 P. Günter, "Introduction to photorefractive materials," *Springer Proc. Phys.* **18,** 206, (1987)

3.1 H. Kogelnik, "Coupled wave theory for thick hologram gratings," *Bell Syst. Tech. J.* **48,** 2909 (1969)

3.2 R.J. Collier, C.B. Burckhardt and L.H. Lin; Optical Holography (Academic Press, Inc., 1971)

3.3 M. Peltier and F. Micheron, "Volume hologram recording and charge transfer process in $Bi_{12}SiO_{20}$ and $Bi_{12}GeO_{20}$," *J. of Appl. Phys.* **48,** 3683 (1977)

3.4 J.P. Herriau, D. Rojas, J.P. Huignard, J.M. Bassat and J.C. Launay, "Highly efficient diffraction in photorefractive BSO-BGO crystals at large applied fields," *Ferroelectrics* **75,** 271 (1987)

3.5 P.D. Foote, "Optically induced anisotropic light diffraction in photorefractive crystals," PhD thesis King's College, London (1987)

4.1 R.E. Aldrich, S.L. Hou and M.L. Harvill, "Electrical and optical properties of $Bi_{12}SiO_{20}$," *J. Appl. Phys.* **42,** 493 (1971)

4.2 S.L. Hou, R.B. Lauer and R.E. Aldrich, "Transport processes of photoinduced carriers in $Bi_{12}SiO_{20}$," *J. Appl. Phys.* **44,** 2652 (1973)

4.3 R. Obershmid, "Conductivity instabilities and polarisation effects of $Bi_{12}(Ge,Si)O_{20}$ single crystal samples," *phys. stat. sol. (a)* **89,** 263 (1985)

4.4 R. Grousson, M. Henry and S. Mallick, "Transport properties of photoelectrons in $Bi_{12}SiO_{20}$," *J. Appl. Phys.* **56,** 224 (1984)

4.5 P.V. Lenzo, E.G. Spencer and A.A. Ballman, "Optical activity and electrooptic effect in Bismuth Germanium Oxide $Bi_{12}GeO_{20}$," *Appl. Opt.* **5,** 1688 (1966)

4.6 J.F. Nye; Physical Properties of Crystals (Oxford University Press 1957)

4.7 P.D. Foote and T.J. Hall, "Influence of optical activity on two beam coupling constants in photorefractive $Bi_{12}SiO_{20}$," *Opt. Comm.* **57,** 201 (1986)

4.8 P.V. Lenzo, E.G. Spencer and A.A. Ballman, "Photoactivity in Bismuth Germanium Oxide," *Phys. Rev. Lett.* **19,** 641 (1967)

4.9 N.A. Vainos and R.W. Eason, "Real time edge enhancement by active spatial filtering via five wave mixing in photorefractive BSO," *Opt. Comm.* **59,** 167 (1986)

5.1 J.P. Huignard and F. Micheron, "High-sensitivity read-write volume holographic storage in $Bi_{12}SiO_{20}$ and $Bi_{12}GeO_{20}$ crystals," *Appl. Phys. Lett.* **29,** 591 (1976)

5.2 J.P. Partanen, J.M.C. Johnathon, and R.W. Hellwarth, "Direct determination of electron mobility in photorefractive $Bi_{12}SiO_{20}$ by a holographic time-of-flight technique," *Appl. Phys. Lett.* **57,** 2404 (1990)

5.3 M. Miteva and L. Nikolova, "Oscillating behaviour of diffracted light on uniform illumination of holograms in photo-refractive $Bi_{12}TiO_{20}$ crystals," *Opt. Comm.* **67,** 192, (1988)

5.4 L.M. Bernardo, J.C. Lopes and O.D. Soares, "Hole-electron competition with fast and slow gratings in $Bi_{12}SiO_{20}$ crystals," Appl. Opt. 29, 12 (1990)

5.5 A.E. Attard and T.X. Brown, "Experimental observations of trapping levels in BSO," *Appl. Opt.* **25,** 3253 (1986)

5.6 B. Kh. Kostyuk, A.Yu. Kudzin and G.Kh. Sokolyanskii, "Phototransport in $Bi_{12}SiO_{20}$ and $Bi_{12}GeO_{20}$ single crystals," *Sov. Phys. Solid State* **22,** 1429 (1981)

5.7 M.A. Krainak and F.M. Davidson, "Two-wave mixing gain in $Bi_{12}SiO_{20}$ with applied alternating electric fields: self-diffraction and optical activity effects," *J. Opt. Soc. Am. B* **6,** 634 (1989)

6.1 L. Pichon and J.P. Huignard, "Dynamic joint-Fourier-transform correlator by Bragg diffraction in photorefractive $Bi_{12}SiO_{20}$ crystals," *Opt. Comm.* **36,** 277 (1981)

6.2 L. Connors, P. Foote, T.J. Hall, R. Jaura, L.C. Laycock, M.W. McCall and C.R. Petts, "Fidelity of real-time correlation by four-wave mixing," *Proc. of SPIE* **492,** 361 (1984)

6.3 J.O. White and A. Yariv, "Real-time image processing via four-wave mixing in a photorefractive medium," *Appl. Phys. Lett.* **37,** 5 (1980)

6.4 J.E. Rao, "Detection of differences in real distributions," *J. Opt. Soc. Am.* **56,** 1490 (1966)

6.5 A.B. Vander Lugt, "Signal detection by complex spatial filtering," *IEEE Trans. Inform. Theory* **IT-10,** 2 (1964)

6.6 S.H. Lee, "Basic principles of optical information processing," *Topics in Appl. Phys.* **48,** 1 (1981)

6.7 J.W. Goodman; Introduction to Fourier Optics (McGraw-Hill 1968)

6.8 N. Collings, Optical Pattern Recognition (Addison-Wesley 1988)

6.9 Z.Q. Wang, W.A. Gillespie, C.M. Cartwright and C. Soutar, "Real-time computer-aided multiplexed optical intensity correlator using Fresnel holographic filters and a liquid crystal television," (to be published in *Opt. Comm.*, 1992)

6.10 A. VanderLugt, "Optimum sampling of Fresnel transforms," *Appl. Opt.* **29,** 3352 (1990)

6.11 R.S. Cudney, R.M. Pierce and J. Feinberg, "The transient detection microscope," *Nature* **332,** 424 (1988).

6.12 M. Cronin-Golomb, A.M. Biernacki, C. Lin and H. Kong, "Photorefractive time differentiation of coherent optical images," *Opt. Lett.* **12,** 1029 (1987).

6.13 D.Z. Anderson, D.M. Lininger and J. Feinberg, "Optical tracking novelty filter," *Opt. Lett.* **12,** 128 (1987).

6.14 N.S. Kwong, Y. Tamita and A. Yariv, "Optical tracking filter using transient energy coupling," *J. Opt. Soc. Am.* **5,** 1788 (1988).

6.15 J.A. Khoury, G. Hussain and R.W. Eason, "Optical tracking and motion detection using photorefractive $Bi_{12}SiO_{20}$," *Opt. Comm.* **71,** 138 (1989)

7.1. F. Vachss and L. Hesselink, "Synthesis of a holographic image velocity filter using the nonlinear photorefractive effect," *Appl. Opt.* **27,** 2887 (1988)

7.2 R.W. Eason and N.A. Vainos, "Photoconductive enhancement of degenerate four-wave mixing reflectivity in BSO," *J. of Mod. Opt.* **35,** 491 (1988)